RICE UNIVERSITY

Nanomechanical and Electro-mechanical Characterization of Materials for Flexible Electrodes Applications

by

Cheng Peng

A THESIS SUBMITTED
IN PARTIAL FULFILLMENT OF THE
REQUIREMENTS FOR THE DEGREE

Doctor of Philosophy

APPROVED, THESIS COMMITTEE

Jun Lou, Chair
Associate Professor of Mechanical
Engineering and Materials Science

Andrew J. Dick
Assistant Professor of Mechanical
Engineering and Materials Science

Qianfan Xu
Assistant Professor of Electrical and
Computer Engineering

HOUSTON, TEXAS
December 2012

ABSTRACT

Nanomechanical and Electro-mechanical Characterization of Materials for Flexible Electrodes Applications

by

Cheng Peng

Flexible electronics attract research and commercial interests in last 2 decades for its flexibility, low cost, light weight and etc. To develop and improve the electro-mechanical properties of flexible electrodes is the most critical and important step. In this work, we have performed nanomechanical and electro-mechanical characterization of materials for flexible electrode applications, including metallic nanowires (NWs), indium tin oxide (ITO)-based and carbon nanotube (CNT)-based electrodes.

First, we designed and developed four different testing platforms for nanomechanical and electro-mechanical characterization purpose. For the nano/sub-micro size samples, the micro mechanical devices can be used for uni-axial and bi-axial loading tests. For the macro size samples, the micro tester will be used for *in situ* monotonic tensile test, while the fatigue tester can be used for *in situ* cyclic tensile or bending testing purpose. Secondly, we have investigated mechanical behaviors of single crystalline Ni nanowires and single crystalline Cu nanowires under uni-axial tensile loading inside a scanning electron microscope (SEM) chamber. We demonstrated both size and strain-rate dependence on yield stress of single-crystalline Ni NWs with varying diameters (from 100 nm to 300 nm), and the

molecular dynamics (MD) simulation helped to confirm and understand the experimental phenomena. Also, two different fracture modes, namely ductile and brittle-like fractures, were found in the same batch of Cu nanowire samples. Finally, we studied the electro-mechanical behaviors of flexible electrodes in macro scale. We reported a coherent study integrating in situ electro-mechanical experiments and mechanics modeling to decipher the failure mechanics of ITO-based and CNT-based electrodes under tension.

It is believed that our combined experimental and simulation results provide some further insights into the important yet complicated deformation mechanisms for nanoscale metals and fracture mechanism for flexible electrodes applications.

Acknowledgments

First and foremost, I would like to sincerely thank my advisor Professor Jun Lou, who has served as an extraordinary mentor to me. It has truly been an honor working under his brilliant guidance over the past four years. I am deeply indebted to all my colleagues at the Lou lab. I would like to thank my parents, Mrs. Heping Zhu and Mr. Aiping Peng and my wife Yan Yan for their constant support and encouragement over the years. I am extremely grateful to my collaborator Dr. Teng Li, Zheng Jia in University of Maryland, Dr. Ting Zhu and Yuan Zhong in Georgia Institute of Technology. Moreover, I expressed my gratuitous to Dr. Yang Lu in Hongkong City University and Dr. Yongjie Zhan in Northwest University, Dr. Jae-Hyun Kim in Korean Institute of Machinery and Materials for providing invaluable samples and for useful discussions, the NFC staff in UMN, and all my friends at Rice MEMS. Finally, I must also thank my committee members, Professors Qianfan Xu and Andrew Dick for their constructive feedback and stimulating questions.

Contents

List of Figures

List of Tables

List of Equations

$$\frac{\Delta R}{R_0} = \left((1+\varepsilon) \cdot \frac{1}{(1-\upsilon \ln(1+\varepsilon))^2} \right) - 1$$ **Equation 4. 8**

Nomenclature

1D	One dimensional
2D	Two dimensional
NW	Nanowire
CNT	Carbon Nanotube
Cu	Copper
ITO	Indium Tin Oxide
MWCNT	Multi Wall Carbon Nanotube
Ni	Nickel
OLED	Organic Light Emitting Diode
PDMS	Polydimethylsiloxane
PET	Polyethylene Terephthalate
PEN	Polyethylene Naphthalate
PI	Polyimide
PMMA	Poly Methyl Methacrylate
SEM	Scanning Electron Microscope
Si	Silicon
SWCNT	Single Wall Carbon Nanotube
TCO	Transparent Conductive Oxide

Chapter 1

1. Introduction

Flexible electronics have attracted significant interests from the electronic industries due to their large deformability, light weight, large surface areas, and low cost. Several promising applications include, but not limited to paper-like displays, solar cell, organic light emitting diodes (OLEDs) and skin-like sensor have started to emerge in the past decades. During the development of flexile electronics, improving the quality and durability of flexible electrodes becomes one of the most critical technical challenges. In this chapter, we will start with the history and concept of flexible electronics, then several most promising materials which were considered to be the candidates for flexible transparent electrodes will be carefully reviewed before presenting the thesis organization at the end.

1.1. Flexible electronics and electrodes

Flexible electronic is a technology featured by having functional electronic circuits/devices assembled on flexible plastic substrates, and it has a long history of more than 40 years. Generally speaking, anything that is sufficiently thin would become flexible. In 1960s, the first generation of flexible electronics was the solar cell arrays, which were made by thinning single crystal silicon wafer cells to ~100 μm and then assembled on a plastic substrate to provide flexibility[1, 2]. After that, with the development of roll-to-roll fabrication techniques and thin film coating in high vacuum system, the flexible TFT was fabricated and prototype flexible organic light-emitting diode (OLED) was presented[3, 4].

In the past decades, the research area of flexible electronics moved very fast. Novel materials were coated onto different organic substrate, and some prototypes and concept devices were fabricated in the labs and companies. While flexible electronics based on thin-film semiconductors are close to commercialization, stretchable electronic materials and devices are still in their infancy. Figure 1.1 gives four typical examples of flexible electronics, including touch screen[5], bendable display[6], electronic skin [7] and solar cell[8]. These are just a few examples for today's fast expanding range of flexible electronics. Inevitably, developing the suitable materials and manufacturing methods that produce stretchable, bendable and twistable devices would revolutionize consumer electronics, solar cell, biomedical devices and many other emerging applications.

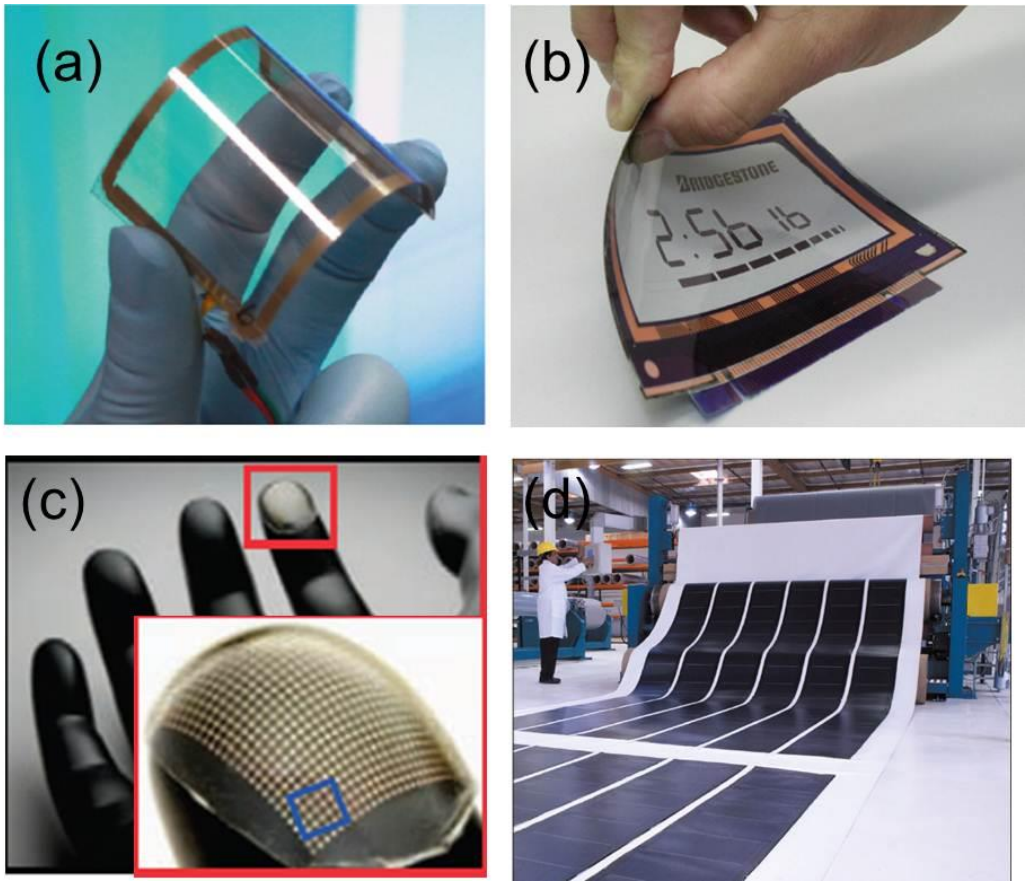

Figure 1.1 Four types of flexible electronics: (a) flexible graprene-based touch screen [5]; (b) bendable display[6] ; (c) electronic skin [7] and (d) flexible solar cell [8].

A generic large-area structure of flexible electronics is composed of a substrate and integrated circuits, offering not only electronic function but also mechanical flexibility. To make the structure flexible, all components must comply with bending, twisting and stretching to some degree without losing their function. The desirable attributes of flexible electronics result from new choices of building block materials (e.g., organic/inorganic hybrids) and manufacturing method (e.g., roll-to-roll printing).

Among the components inside these flexible electronics, the flexible transparent electrodes are key components, and need to be further developed and improved. Compared to the traditional semiconductor silicon (Si)-based electronics, the flexible electronics will be rugged, bent, twisted and stretched, and then need to survive after large deformation. In this case, the electro-mechanical behavior is of critical importance, and thus how the electrical resistance changes during the mechanical deformation become an important parameter to evaluate the electronic performances. The curve of resistance changes versus strain is always used to quantitatively evaluate electro-mechanical response of electronics, as shown in Figure 1.2 [9]. The critical strain, defined as the strain when the resistance starts to increase dramatically, had be employed as an important parameter (~1.5% for 200 nm sample in Figure 1.2 a). Moreover, how the resistance changes during cyclic bending or tensile tests is also another way to evaluate electro-mechanical properties. The electrical resistance versus number of stretches is shown in Figure 1.2 b. For the carbon nanotube (CNT) coated Polydimethylsiloxane (PDMS) sample, it was loaded to the strain of 25% and then unloaded to 0% in each cycle, and the electrical resistance was nearly a constant number after 12500 cycles. This indicates that the sample has good electro-mechanical properties under cyclic loading conditions described above.

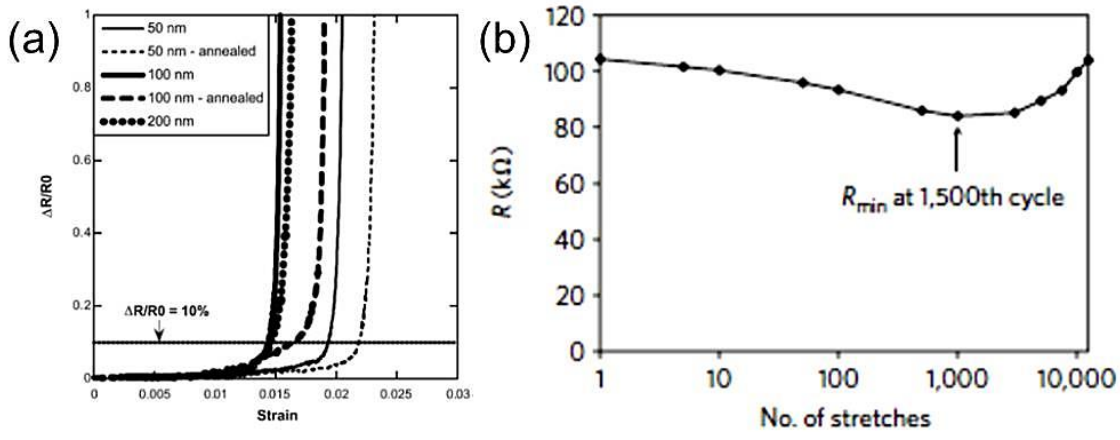

Figure 1.2 (a) Normalized resistance as the function of strain of ITO coated PET samples [9]. (b) Resistance versus number of stretches (on a log scale) of CNT coated PDMS sample [10].

The choice of materials and corresponding manufacturing methods for flexible electrodes are critical steps to ensure the success of the flexible electronics. The desirable materials must have these three characteristics: low resistivity (~10^{-4} ohm-cm), high transparency (>80%) and can be coated onto thin layer structures to endure bending, stretching and twisting during service. With the fast development of nanomaterials, many of them have become candidates for building flexible electrodes, e.g., indium tin oxide (ITO) nanoscale thin films, carbon nanotube (CNT), metallic nanowires (NWs), and mono-layer graphene etc. In the following section, we will focus on the first three kinds of materials: ITO, CNT and nanowire films.

1.2. Indium tin oxide thin film as flexible electrode

Transparent conducting oxides (TCO), e.g., indium oxide (In_2O_3), tin oxide (SnO_2) and zinc oxide (ZnO), have been widely investigated due to their good combination of electrical conductivity and optical transmittance. The applications of TCO include electrodes for most flat panel display technologies, collector electrodes in solar cells etc. Indium tin oxide (ITO) is one of the most common TCO that has been widely used for its superior combination of environmental stability, relatively low electrical resistivity ($\sim 10^{-4}$ ohm-cm) and high transparency (>90% at a film thickness of 100 nm) to visible light.

In the early days, the transparent electrodes were made by directly coating ITO powders onto the rigid glass substrates providing the combination of conductivity and transparency (Figure 1.3 a and b). With the great improvements made on sputtering deposition techniques, ITO thin films were deposited onto polymeric substrate materials (e.g. polyethylene terephthalate (PET) in Figure 1.3 c, polyethylene naphthalate (PEN), polyimide (PI), and poly methyl methacrylate (PMMA)), and then widely used as transparent conductors and interconnects in flexible displays and solar cell. Thin ITO film was coated onto the polymeric substrate and can survive after certain degrees of bending. In this stage, the good combination of transparency and conductivity enables ITO to be a good candidate material for flexible transparent electrodes as a starting point.

However, two drawbacks of ITO-based electrodes severely limit their potentials as dominating flexible electrodes: one limitation is the scarce indium

source on earth that results in high price of ITO, and another fatal disadvantage lies on its mechanical brittleness that is susceptible to the cracking with loss of function under large deformation. While compliant polymer substrates can sustain large strain, ITO thin films are brittle and often fracture at small strain. The cracking of ITO conductors and interconnects leads to loss of electrical conductance, posing crucial challenge to the reliability of flexible devices. During the uniaxial loading, the channel cracks perpendicular to the loading direction is the main reason for the failure of electrodes (Figure 1.3 d). The critical strain for the initiation of channel is only ~ 1%. Moreover, delamination from the substrate is another major issue because of the initial stress during the fabrication process.

The limitations of ITO and other TCO have motivated people work hard to find out new materials to substitute ITO-based electrode, including conductive polymer, carbon nanotube (CNT), metal grids, metallic nanowire and mono-layer graphene. In the following sections, we will mainly focus on the introduction of CNT and metallic nanowires.

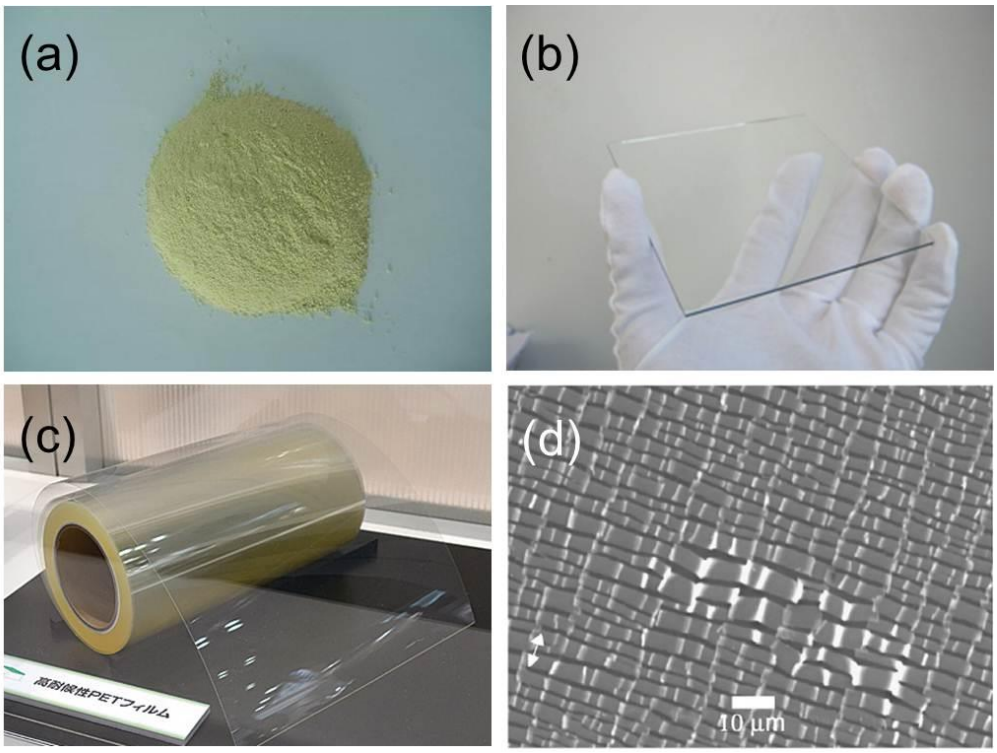

Figure 1.3 (a) ITO powder. (b) ITO coated on glass substrate. (c) ITO coated on PET substrate[11]. (d) ITO cracking and delamination of an ITO-coated PET sample tensile tested above 6% strain. Arrows indicate applied force direction [12].

1.3. Carbon nanotube film as flexible electrode

Carbon nanotube (CNT) film is considered as the most promising materials to substitute ITO-based electrode. First, excellent electrical properties of CNT can be relatively easily tuned by chemical methods after nearly 20 years of research efforts; Second, the random network structure of the CNT film (Figure 1.4 c) statistically averages the electrical resistance and reduces the quality difference from device to device during the manufacturing process; Third, low resistance and high transparency features can be comparable to ITO-based electrode. Compare to

100 ohm/sq sheet resistance and 85% transmission of ITO coated PET samples, the sheet resistance can be 600 ohm/sq for 50 nm thick CNT film and the transmission (including the PET substrate, CNT and polymers) can be 85% at 550 nm[13].

Room-temperature fabrication of NT films ensures compatibility with a variety of surfaces that are used for printed electronics on flexible substrates. Solubilization and deposition are the main parts of the technology: while solubilization is trying to separate the NT in solution, deposition is trying to transfer the tubes uniformly from solution to a given substrate. Among the deposition, spraying, slot coating, spin coating and filtration/stamping are the mainly methods.

More importantly, numerous experimental results demonstrated that the CNT-based electrodes retained good performance after large deformation. It was found that even after heavy mechanical crumpling[14], or monotonic tensile loading to 700% strain[15], the films still remain conductive. There was also only 5 times increase in electrical resistance under the strain of 150%[10]. Additionally, cyclic bending experiment on CNT films reported almost no electrical resistance change after 10,000 cycles of bending around a 5 mm radius cylinder[16], only 20% electrical resistance changes after 12500 cycles of bending at 25% strain, and nearly hysteresis-free behavior was found in up to 100 tensile fatigue cycles[17]. These previous reports highlight the excellent mechanical durability of CNT based electrodes, but the understanding of structural and corresponding functional evolutions in CNT films under loading is still quite limited: the surfaces of CNT films were examined by optical microscope after cyclic loading-unloading

experiments[13], and the surface morphology evolution of CNT films was recorded by atomic force microscope (AFM) during stretching with insufficient details on the deformation and failure processes provided[10]. More *in situ* electro-mechanical experiments are clearly in need before a complete understanding the fundamental deformation and failure mechanisms in such CNT films could be reached for reliable operation of flexible devices under large deformation.

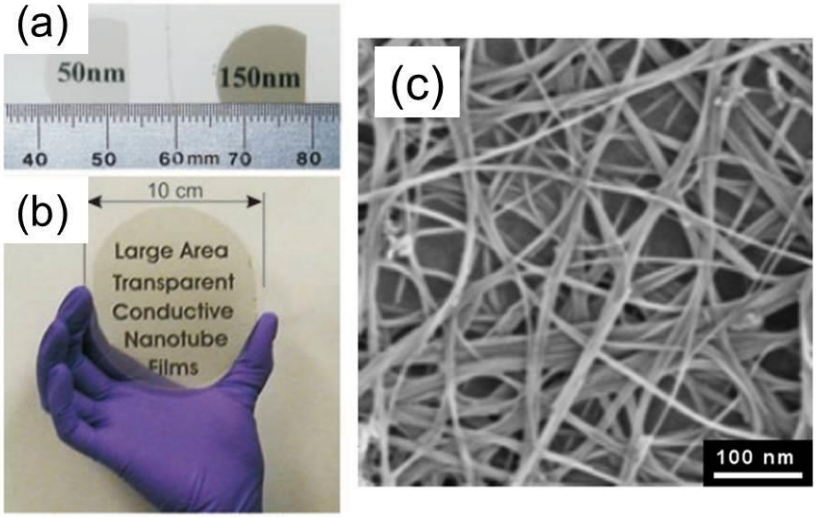

Figure 1.4 (a) Transparent single wall carbon nanotube (SWNT) films of the indicated thickness on quartz substrates. (b) A large, 80-nm-thick SWCNT film on a sapphire substrate 10 cm in diameter large area [18]; and (c) Scanning electron micropscope (SEM) image of a CNT network [13].

Solution-coated films of carbon nanotubes (CNTs) are one flexible alternative to ITO, but to date they still have their own shortcomings: a relatively low transmittance and sheet resistance due to their absorbance of light and the poor electrical contact between nanotubes. Owing to the mixture of carbon nanotube properties, with 1/3 metallic and 2/3 semiconducting, the sheet resistances of CNT

electrodes are dominated by the large CNT junction resistances. A typical sheet resistance for CNT networks on plastic is 200-1000 ohms/sq with an optical transmittance of 80-90%.[19] For voltage driven devices, such as capacitive touch screens, electro wetting displays, and liquid crystal displays, the relatively high sheet resistance of CNT networks is not problematic. However, the relatively higher sheet resistance would prevent the practical application of transparent CNT electrodes in current based devices such as organic light emitting diodes and solar cells. These problems aim to be solved by improvement of fabrication techniques.

1.4. Mechanical properties of metallic nanowire

One-dimensional metallic nanowires (NWs), as important building blocks for electromechanical systems, circuit interconnects, and nano devices, have recently drawn considerable attention. As the dimensions of materials become smaller, the surface to volume ratio increases, and then the role played by free surface becomes more important than that in bulk materials. Moreover, the defects size and amount can be largely reduced in the small scale materials. In such a small scale, some superior and interesting phenomena might happen in the nearly defect-free metallic nanowires, e.g., ultra-high strength, high electrical and thermal conductivity.

It is crucial and important to understand the mechanical properties of metallic nanowires before their fully utilization. The density functional theory and molecular dynamics calculations suggested that the ideal surface strength of different metals (Au, Al, Pt, Cu, Ni) is around half of its ideal bulk strength.[20, 21] Experimental

studies on nanowires also have been extensively studied in past decade. Several novel methods ways have been developed to test nanowires mechanical properties, e.g., nanoindentation tests[22], MEMS based tensile testing[23], atomic force microscope (AFM) assisted bending[24], micro/nano pillar compression[25, 26] and tension tests[27], and TEM-AFM holder method[28]. These results are good demonstrations of ultra-high strength in metallic nanowires and provide important parameter for the real applications.

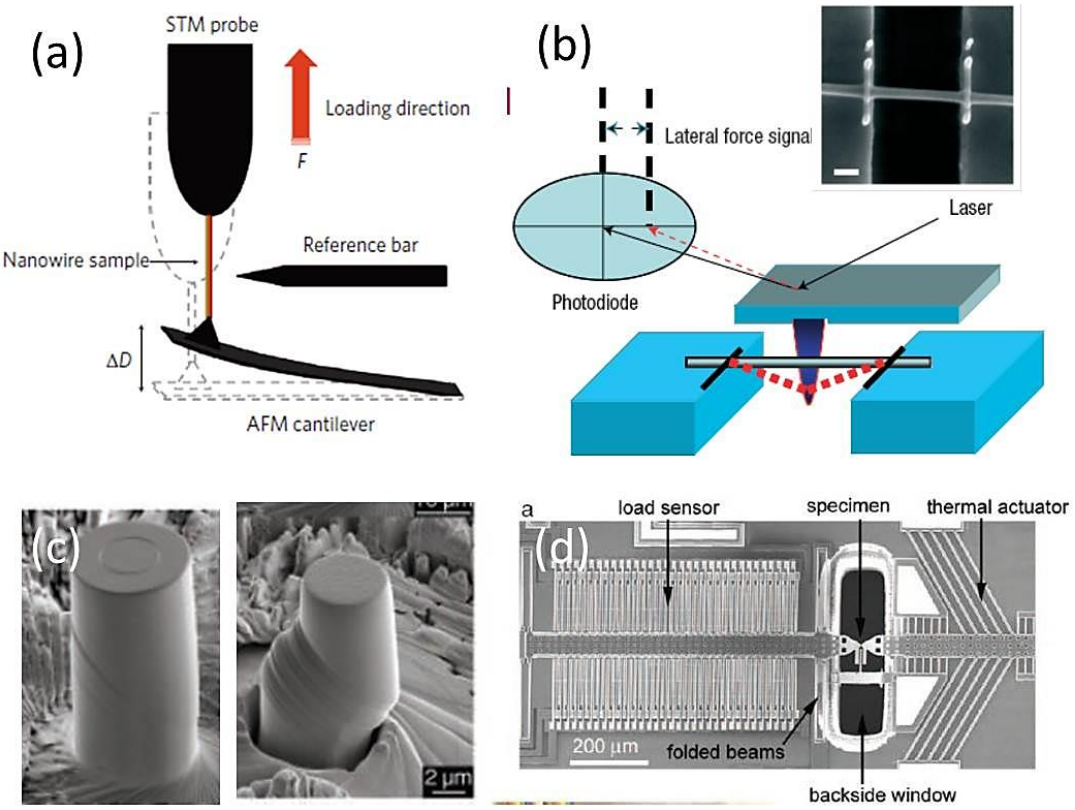

Figure 1.5 Mechanical testing methods for nanomaterials: (a) Schematic of TEM-AFM holder, showing how the AFM cantilever acts as a force sensor (by measuring the deflection of the cantilever, ΔD) and the STM probe acts as an actuator while the attached nanowire sample is under tensile loading[28]. (b) The AFM bending test for nanowire mechanical measurements [24]. (c) Ni micro pillar compression experiments [29]. (d) Tensile tests performed by a micro-electro-mechanical system inside TEM chamber[23].

Table 1. 1 **Experimental results of strength in metallic nanowires**

Sample	Size in diameter	Strength (GPa)	Testing Method	Reference
Au	10 nm	0.93	TEM-AFM holder	Lu et al. [30]
Au	40-250 nm	5.6	AFM-assist Bending	Boland et al. [24]
Au	350 nm	0.8	Nano Pillar Compression	Greer et al. [26]
Au	300 nm	1.0	Nano Pillar Compression	Volkert et al. [31]
Cu	75 nm	7.0	Nano Pillar Compression	Volkert et al. [32]
Co	300 nm	1.5	MEMS	Michler et al. [33]
Ag	16 nm	7.3	AFM-assist Bending	Boland et al. [34]
Al	--	2.0	Nanoindentation	Minor et al. [35]
Pt	--	4.4	Nanoindentation	Mason et al. [36]

1.5. Metallic nanowire thin film as flexible electrode

As mentioned above, transparent electrodes, indispensable in displays and solar cells, are currently dominated by ITO films. Because of its brittleness and high price of indium, people are trying hard to find out some alternatives to substitute ITO. Sheet resistance and optical transmittance are two key parameters that determine the applications of transparent electrodes. During different novel materials, CNT is one of the promising one for the ITO replacement. However, a sheet resistance of 100-1000 ohm/sq at 80% optical transmittance is still too high for display and solar cell application. To further reduce the resistance, people came back to metal materials. Recently, metal nanostructures such as copper nano-grids

have been developed, with sheet resistance of 10-20 ohm/sq at 80% transparency [37, 38]. However, the costly lithography steps and difficulty in scaled up production limit its wide applications.

One-dimensional metallic nanowires (NWs), as important building blocks for electromechanical systems, circuit interconnects, and nano devices, have recently drawn considerable attention. Random networks thin film of metallic nanowires (NWs) is also a promising replacement of ITO due to its high conductivity and optical transmittance. Compared to the nano-grid metals, the synthesis cost is relatively low. Similar like random networks of CNT, the metallic NWs can also be scalable synthesis and then be filtered into solution to make transparent conducting films. In other words, high conductivity, good plasticity and relatively low price enable them to be the component of flexible electrodes.

Different metallic nanowires, e.g. silver and copper, have been selected as the candidates of metallic nanowires thin films, as showed in Figure 1.5. Cui proved that the solution-coated films of long silver nanowires (Ag NWs length ~10 um) have a transmittance (80%) and sheet resistance (20 ohm/sq) close to ITO, even silver is also scarce and expensive[19]. Other than expensive silver, copper (resistivity $\rho = 1.59*10^{-9}$ ohm-m) is nearly as conductive as silver ($1.67*10^{-9}$ ohm-m), but it is 100 times less expensive and 1000 times more abundant. Wiley et al have recently reported a scalable synthesis of copper nanowires (Cu NWs) and filtered them from solution to make transparent conducting films. The well-dispersed and high ratio (length>20 um and diameter<60 nm) nanowires enable the conducting films with a

low sheet resistance of 30 ohm/sq at a high transmisttace of 85%[39]. Moreover, the electro-spinning Cu nanofiber network is another type of transparent electrodes, which achieved 50 ohm/sq at transmittance of 90% and could be successfully used as electrode inside the solar cell [40].

The properties of nanowires electrodes are strongly affected by the quality of nanowires and the junction resistance. Right now, metallic nanowires can be fabricated by several methods, including template method[41], thermo hydrau method[42], photochemistry method[43] and seed mediated methods[44]. These methods will certainly produce nanowires with different levels of quality, and the subsequent procedures including dissolving and dispersing can also induced the damage to the nanowires. Moreover, the length and the diameter will affect the quality of the electrodes. Long and thin nanowires are always better than the short and thick nanowires[39]. How to fabricate massive long and thin nanowires is also a problem needed to be solved. People are working hard on the improvement of metallic nanowires thin film, and it is believed that these problems will be solved later on.

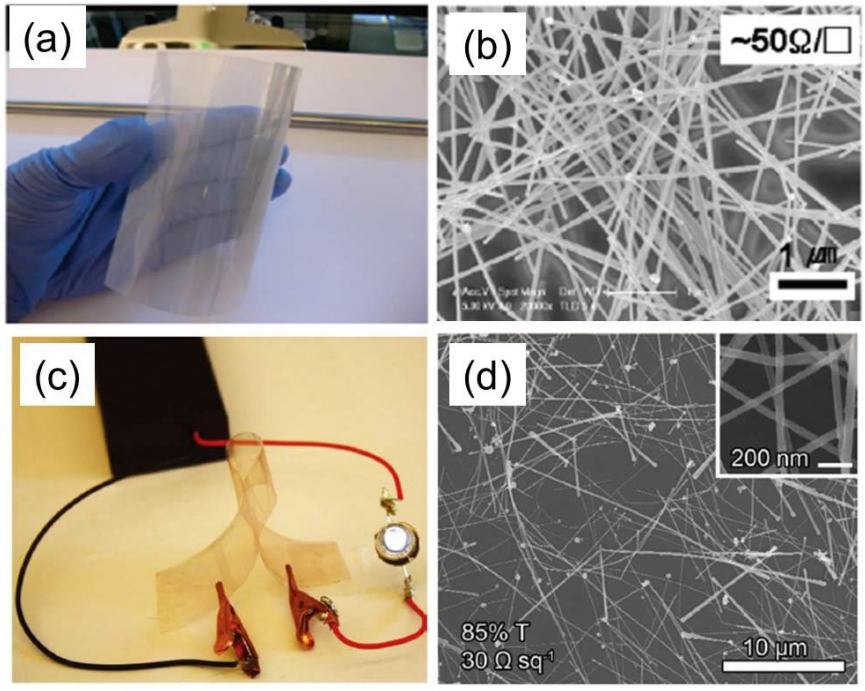

Figure 1.6 (a)Finished Ag NWs film coating on PET substrate. The Ag NW coating looks uniform over the entire substrate shown in the figure. (b) A SEM image of Ag NW coating shown in (a). The sheet resistance is 50 ohm/sq [19]. (c) A bend Cu NW film (25 ohm/sq and 83% transparent) completing an electrical circuit with a battery pack and a LED. (b A SEM image of Cu NW coating shown in (c). The sheet resistance is 30 ohm/sq [39].

1.6. Comparison of different flexible electrodes

Other than ITO, CNT and metals, there are still many advanced materials considered to be the candidates for transparent electrodes. Graphene electrodes are an emerging candidate as showed in Figure 1.1 a, with the performance of 300 ohms/sq and 80% transmittance [45, 46] and getting better of 125 ohm/sq at 97% transmittance [5]. A graphene electrode could have significantly lower cost due to the abundant material source and new methods for making these thin films.

However, significant improvement is needed before the sheet resistance can reach the low values of ITO for current driven devices, especially OLED and solar cell. Moreover, hybrid structures of metallic grid and graphene were fabricated as transparent and flexible conducting films[47]. The sheet resistance of the fabricated electrodes was as low as 8 ohm/sq with the transmittance of 80% and 30 ohm/sq with the transmittance of 90%.

Following table gives the performance comparison of different transparent electrodes.

Table 1. 2 Comparson of different transparent electrodes

Materials	Transparency	Sheet Resistance (ohm/sq)	Bending Cycles with damage	Critical Strain	Reference
ITO on glass	90%	15		~1%	VLSI standards
ITO on PET	85%	100 with 200 nm ITO		1.75%	[12]
CNT on PET	85%	600 with 50 nm CNT		25%	[13]
Ag NWs on PET	80%	20			[19]
Cu NWs on PET	85%	30	1000 cycles at 2.5 mm radius		[39]
Cu nanofiber on PDMS	90%	50	1 cycle at 6mm radius	10%	[40]
Ag grid on PDMS	85%	0.5			[37]
Au grid electrodes	84%	24			[38]
Graphene on PET	97%	125		>6%	[5]
Hybrid structure of Cu grid and graphene on PET	90%	8	500 cycles at 5 mm radius		[47]

1.7. Organization of thesis

In this thesis, we will take three kinds of candidate materials for flexible electrodes as our studying objects: metallic NWs, ITO thin film, and CNT thin film.

In the chapter 2, four types of testing platform for different materials will be introduced.

Chapter 3 will put focus onto the mechanical behavior of metallic NWs. Firstly, the size dependent mechanical behavior, including fracture modes in copper (Cu) NWs and strength in nickel (Ni) NWs will be included. After that, the strain rate dependent strength and yield stress in Ni NWs will be illustrated.

Chapter 4 will put focus on the electro-mechanical characterization of two types of flexible electrodes: ITO-based and CNT-based thin film on the polymeric substrates. The cracking fracture mechanism will be studied in both single layer and multilayer ITO-based electrodes, and then the crack evolution of CNT thin film during both monotonic and cyclic uni-axial loading will be showed.

Finally in the Chapter 5, the conclusive remarks will be summarized, and the author will provide with some suggestions for future work.

Chapter 2

2. *In situ* electro-mechanical characterization methods for flexible electrodes and their components

Electro-mechanical behavior is critical for flexible electronics, because large deformation is going to directly applied to these electronics. Unfortunately, there is no standard testing method and equipment for the electro-mechanical characterization purpose. In this chapter, we designed four types of testing platforms for the electro-mechanical characterization. For 1-d metallic nanowires, the *in situ* uni-axial micro mechanical device has been fully developed and utilized for this purpose. For 2-d nanomaterials, a bi-axial *in situ* micro mechanical device has been designed and optimized in structures. For the macro-scale ITO-based and CNT-based electrode samples, the *in situ* electro-mechanical testing platforms,

including tensile and bending testers, have been designed, manufactured and utilized.

2.1. *In situ* uni-axial micro mechanical device for 1-D nanomaterials

For 1-d nanomaterials, the typical sample size is ~100 nm in diameter and ~10 um in length. For mechanical testing, the required load and displacement resolutions are in the order of uN and nm. To load the sample into failure, the maximum force and displacement are in the order of mN and um. Moreover, the observation requirement is to see the morphology during the deformation. To meet all the requirements, we first designed this uni-axial tensile platform and developed following techniques for mechanical characterization purpose.

In situ uni-axial tensile tests of fabricated 1-D nanomaterials were performed using a recently developed micromechanical device inside a FEI Quanta 400 SEM. Device fabrications, using the standard photolithographic techniques, have been described in details in these previous paper.[48] The working principle of this device is a simple "push–pull" mechanism which is shown in Figure 2.1 a. Briefly, the Agilent inSEM nanoindenter was employed as the device actuator, as well as the force and displacement sensor. With compression forces applied by the indenter head to the top shuttle , the two middle sample stages would move in opposite directions, due to the design of symmetric inclined beams. Therefore, the sample clamped onto the sample stages would be stretched uni-axially in the x -direction.

The load and displacement resolution can be as high as 69.4 nN and 0.87 nm, respectively, and the maximum loading force could reach 10 mN. Therefore, the capacity of the experimental set-up is sensitive enough to accurately measure the mechanical properties of metallic NWs and powerful enough to fracture the NWs. Monotonic loading or cyclic loading-unloading test can be performed, until the sample breaks. The load applied to and displacement of the top shuttle can be obtained from the high resolution quantitative nanoindenter. Once the geometry of 1-d nanomaterial was measured, the stress-strain curve could be derived from recorded load-displacement data from the nanoindenter and a response substraction method.

One of the challenges is to precisely manipulate, align, and clamp samples onto the device.[48] In all the samples testing in this work, only the samples with good alignment, like shown in the inset of Figure 2.1 a, were in used and tested. Due to the relative low stiffness of epoxy clamping portion, the displacement of deformed epoxy was taken into account. To ensure the accuracy of displacement measurement, a digital image correlation method was also utilized [49] and all the results in this thesis (Chapter 3) have been corrected by this technique.

Other than the uni-axial tensile testing, the electrical response is also aim to be measured during the loading. By the coating conductive metals on selected area of the semi-conductive Si device, the current flow can be controlled intentionally, and then the four-point probe electrical measurement will be realized. By applying the DC voltage on between the two top electrodes, the current flow will be in the

direction as showed in the Figure 2.2, and then the current can be measured between the two bottom electrodes. Furthermore, the electro-mechanical measurement can be realized by combining the mechanical testing mentioned above. Right now, the fabrication techniques are still need to be improved and optimized before the real application of this type of device.

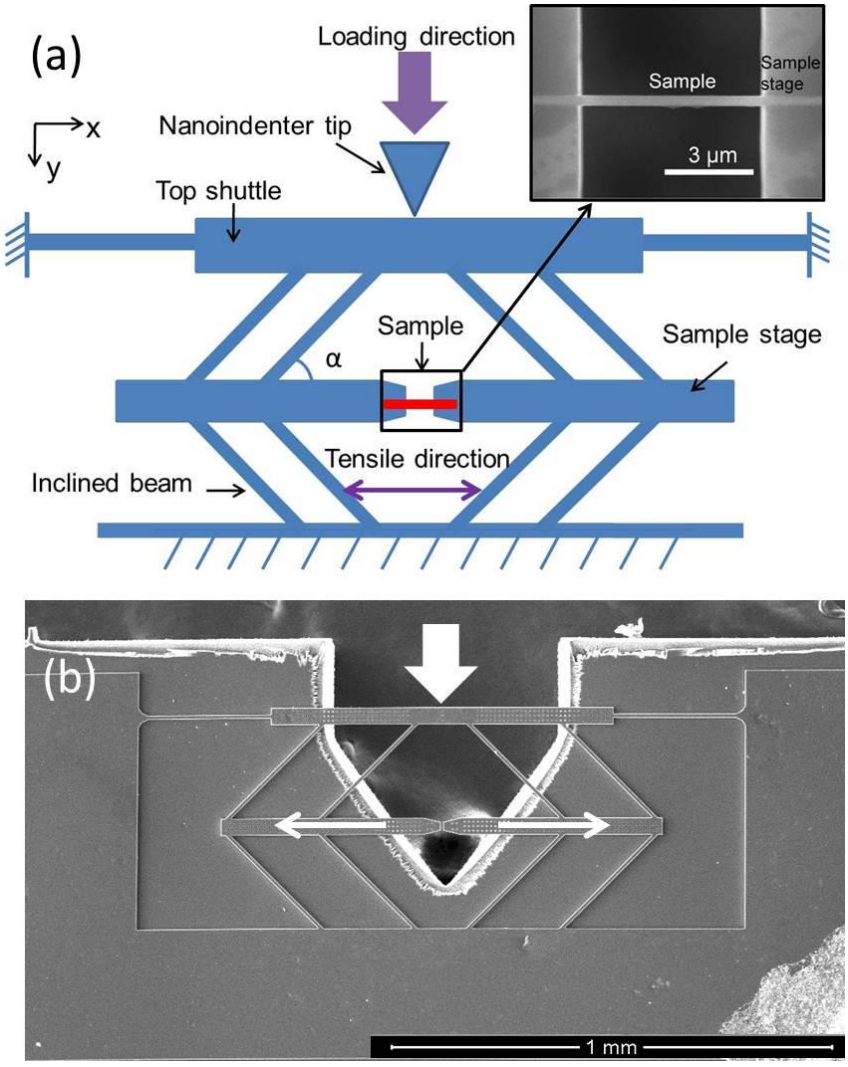

Figure 2.1 (a) Schematic illustrations of the micromechanical device. The arrows indicate the "push–pull" working principle. Inset: a real Cu NW with good clamping alignment. (b) SEM image of micro mechanical device, and the arrows indicate the movement of the device during the compression loading.

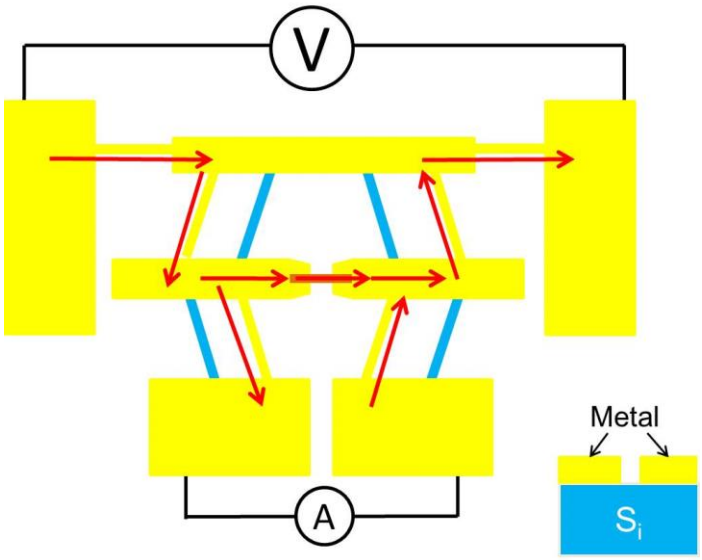

Figure 2.2 Four-point probes electrical measurement during loading process. The red arrows indicate the current flow.

2.2. *In situ* bi-axial micro mechanical device for 2-D nanomaterials

2-D nanomaterials, such as free standing graphene, molybdenum disulfide (MoS_2) and boron nitride (BN) thin films, attract so much interest for their conductivity or insulation. How their electrical properties perform during loading is an important research topic, before we can fully utilize them as components inside flexible electronics. Rather than uni-axial loading, bi-axial loading is also critical for this type of 2-D nanomaterials. To develop a reliable and easy-to-use device for the testing is an urgent work. Two challenging things lay in front of us: one is how to

apply the bi-axial loading to the sample; another one is how to firmly clamp the thin film onto the device.

Inspired by a microsystems platform to study biomechanical response of single living cells to in-plane biaxial stretching (Figure 2.3), the “X-shape” structure will be induced into our device design to conquer the first challenge. As showed in Figure 2.3, the layout of the biaxial cell stretcher MEMS contains the quadrant platform and relative linkages on the top, and the single, large comb drive on the bottom part. When the force is applied in the downward direction, the live cell sample will be stretched in bi-axial ways[50]. The similar idea was also showed in the recent work in [51] . In our design, by combining the push-pull loading mechanism and X-shape structure, the bi-axial force can be applied to the 2-D sample, as showed in Figure 2.4. The working principle is very similar to the 1-D micro mechanical device: when the loading force was applied on the top shuttle, the four sectors in the middle of the device will be separated. If the sample is well fixed in the middle, the sample will be under bi-axially loading. At this stage, the first problem of how to apply bi-axial loading to the sample has been solved.

To solve the second problem, the 2-D thin film will be directly mounted onto the device. With the relative large contact area and strong Van der Waals attraction from the substrate and surface tension during drying process, the thin film is believed to be fixed firmly onto the device substrate. [52, 53]

The geometry optimization has been done by finite element analysis (FEA) before the fabrication process. Because of the device’s planar beam-based geometry,

a 2-D FEA model was first constructed using ANSYS Beam 32 elements. Material nonlinearities were ignored, since the device layer was made of single-crystal silicon, which is linear elastic at the temperatures at which the experiments were conducted. However, since large deformations might occur as the indenter load increases, geometry nonlinearities were considered in the analyses. For all the analyses, the Young's modulus and Poisson's ratio of single-crystal silicon (<100> orientation) were set equal to 160 GPa (obtained via nanoindentation of the device layer after fabrication) and 0.278, respectively. By tune the spacing between the sectors and the length of beams, the displacement ratio between x and y directions can be tuned to be almost equal (~0.97).

The second step for FEA is to see if the uniform stress can be applied to the testing sample. Because the device layer is rather thin (6 um) compared to the beams length (>300 um), the plain stress assumption is used and the element of plain stress (Plane 42) is employed in Ansys FEA software. The contour of stress state (Figure 2.6) shows the stress state is relative uniform among the sample mounting in the middle of four sectors.

Finally, the device was fabricated in the Nanofabrication Center, University of Minnesota. The general photolithography process is used, the same as the ones using in fabrication of 1-D micro mechanical device. The SiO_2 layer is only 3 um, in order to reduce the adhesive stress and enable the device is sensitive enough in the testing mono-layer 2-D nanomaterials. The Si device layer is 6 um, in order to reduce the stiffness of the whole device. In the final products after fabrication, the

four sectors in the middle of the device are in the same plain, making sure that the 2-d thin film will be under the plain stress state (Figure 2-5).

To evaluate the quality of the device, the stiffness of empty device, defined by the load versus displacement on the top shuttle, has been measured by nanoindentor. The value of stiffness is close to the simulation result (3800 N/m VS 3650 N/m), and this result confirm the validation of FEA simulation.

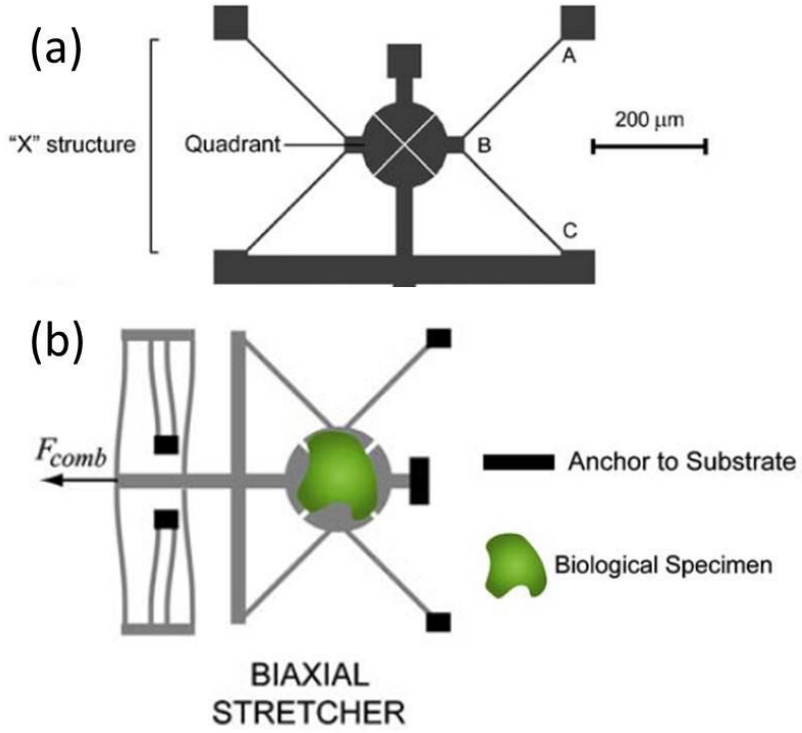

Figure 2.3 Schematic illustrations of the 2-D micromechanical device. (a) Layout of the biaxial cell stretcher MEMS, showing the quadrant platform and relative linkages on the top, and the single, large comb drive on the bottom part.[50] (b) Schematic depiction of MEMS for cell mechanics [51].

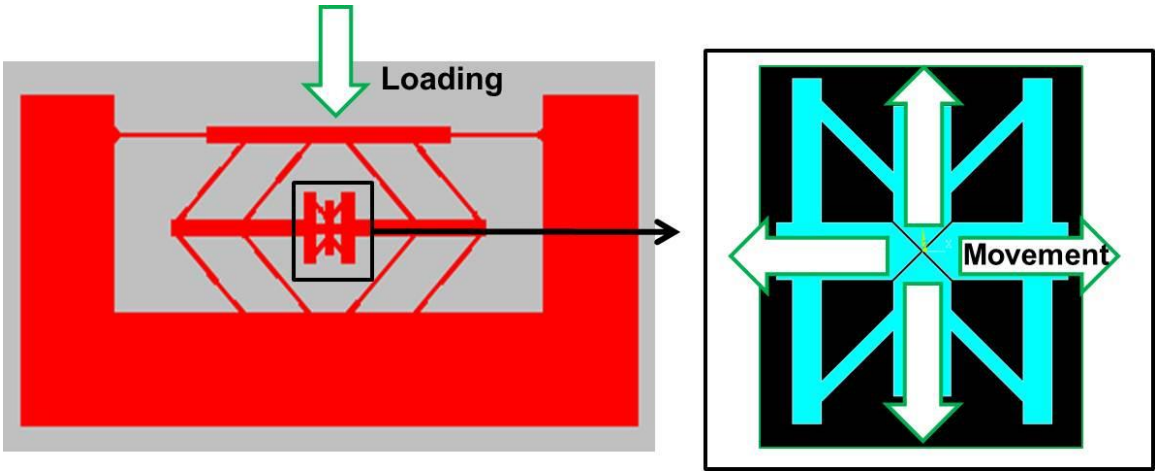

Figure 2.4 Micro mechanical device designed for bi-axial testing, and the arrows indicate the loading direction.

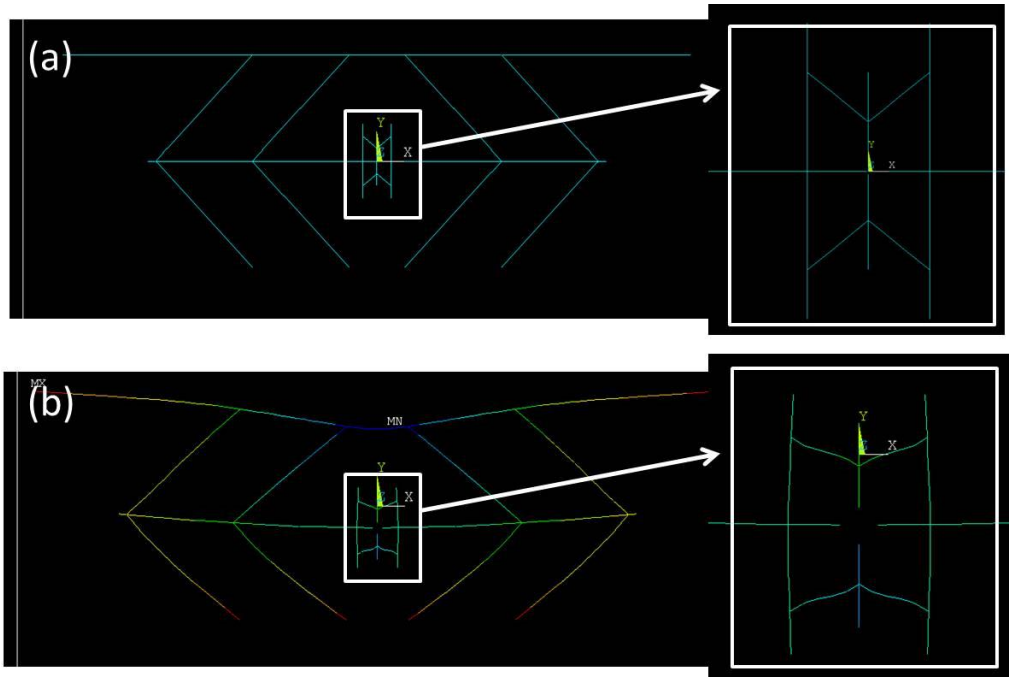

Figure 2.5 Finite element analysis of 2-D mechanical device, (a) before and (b) after deformation.

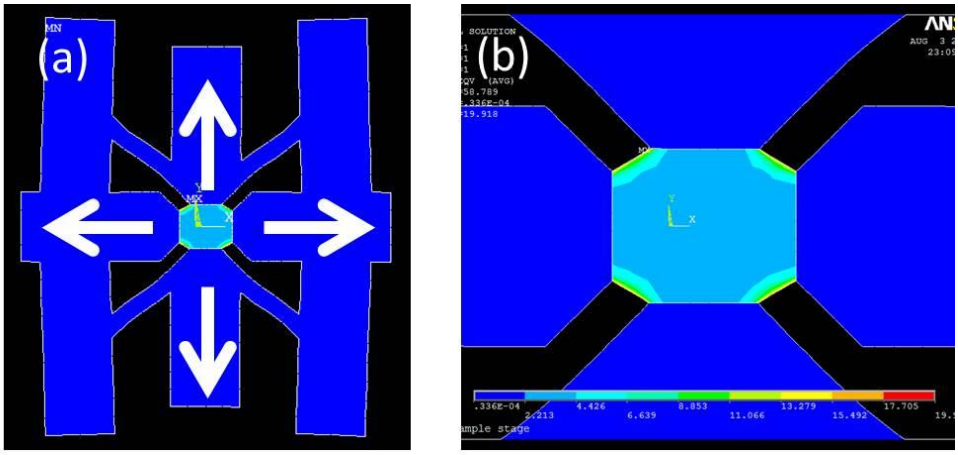

Figure 2.6 Finite element analysis of 2-D mechanical device. (a) The uniform stress is found in the middle of the clampped sample, except in the corner. (b) Details of stress contour in (a).

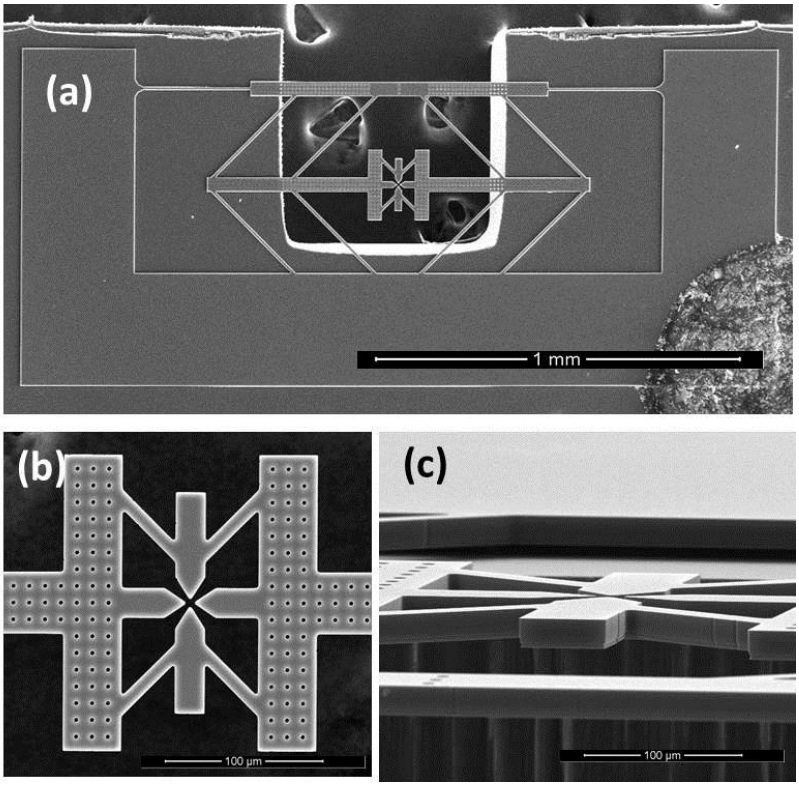

Figure 2.7 The SEM images of real 2-D device. (a) top view; (b) in the middle of the device (c) side view of the device showing the four sectors are rather flat.

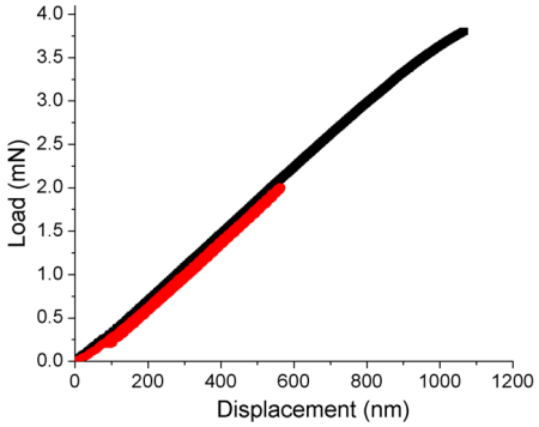

Figure 2.8 Two calibration curves of empty device under different loading ranges.

Table 2. 1 Comparison of experimental and simulation results.

Device	Stiffness (N/m)
Simulation	3800
Real Device	3650

2.3. *In situ* electro-mechanical testing platforms for flexible electrodes

For the macro-scale electrode sample, the sample size is much bigger and easier to be clamped. In this case, two electro-mechanical testing platforms, including tensile and bending testers, are introduced. Each testing platform includes three parts: micro tester, SEM, electro measurement.

The first testing platform is the tensile platform, it included microtester, SEM and electrical measurement.[54] The microtester, showed in Figure 2.9 a, was manufactured in Deben UK, Ltd. The maximum force and displacement capacities of the micro-tester are 200 N and 10 mm, with resolution of 0.01 N and 0.001 mm, respectively. The in situ tensile tests were performed using a microtester (Deben UK, Ltd.) inside the SEM chamber (FEI Quanta 400 high resolution field emission scanning electron microscope, FEI company, Hillsboro, OR). The whole equipment set-up is illustrated in Figure 2.9 c. The uni-axial tensile tests were conducted under displacement control, and the strain rate was controlled to be around 10^{-4}/s. The increase of applied tensile strain was paused at certain preset strain values to allow for high resolution SEM imaging at different locations along the sample length. The electrical resistance of the samples was measured by two point probe method using a Keithley 2000 multimeter during the tensile test.

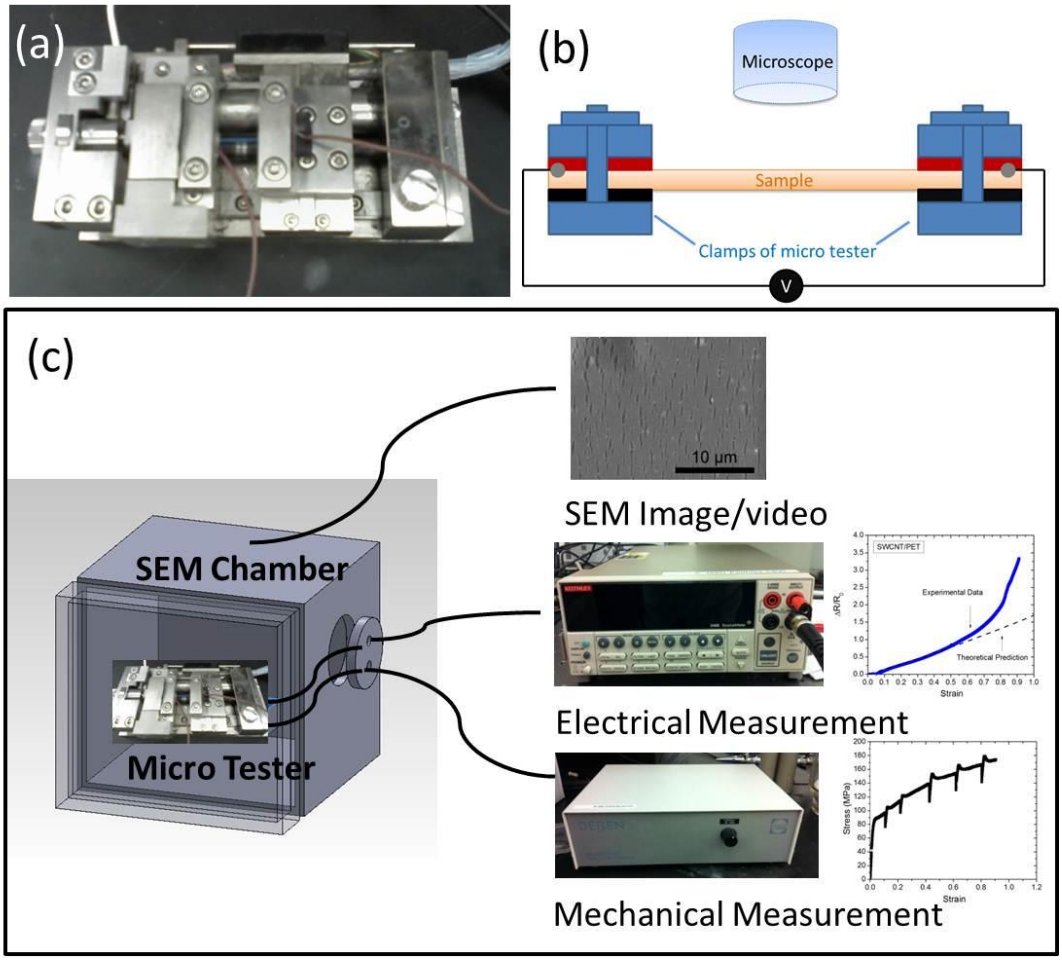

Figure 2.9 The microtester and electro-mechanical testing. (a) Micro tester with sample clamped in the middle. (b) Schmatics of *in situ* tensile test with two-point probe electricla maasuremnt. (c) Illustrattion of electro-mechanical set-up.

In the real application, cyclic fatigue testing is more important for flexible electronics. In this case, the *in situ* fatigue testing machine, including tensile and bending, was designed and manufactured. As showed in Figure 2.10, the piezo atutor is induced as the actuator, which can generate up to 30 um displacement and the frequency can be 5 Hz. By changing the clamping portion in the tester, either

tensile or 3-point bending loading can be applied to the sample. More important, they can also be set-up into the SEM for the *in situ* observation purpose.

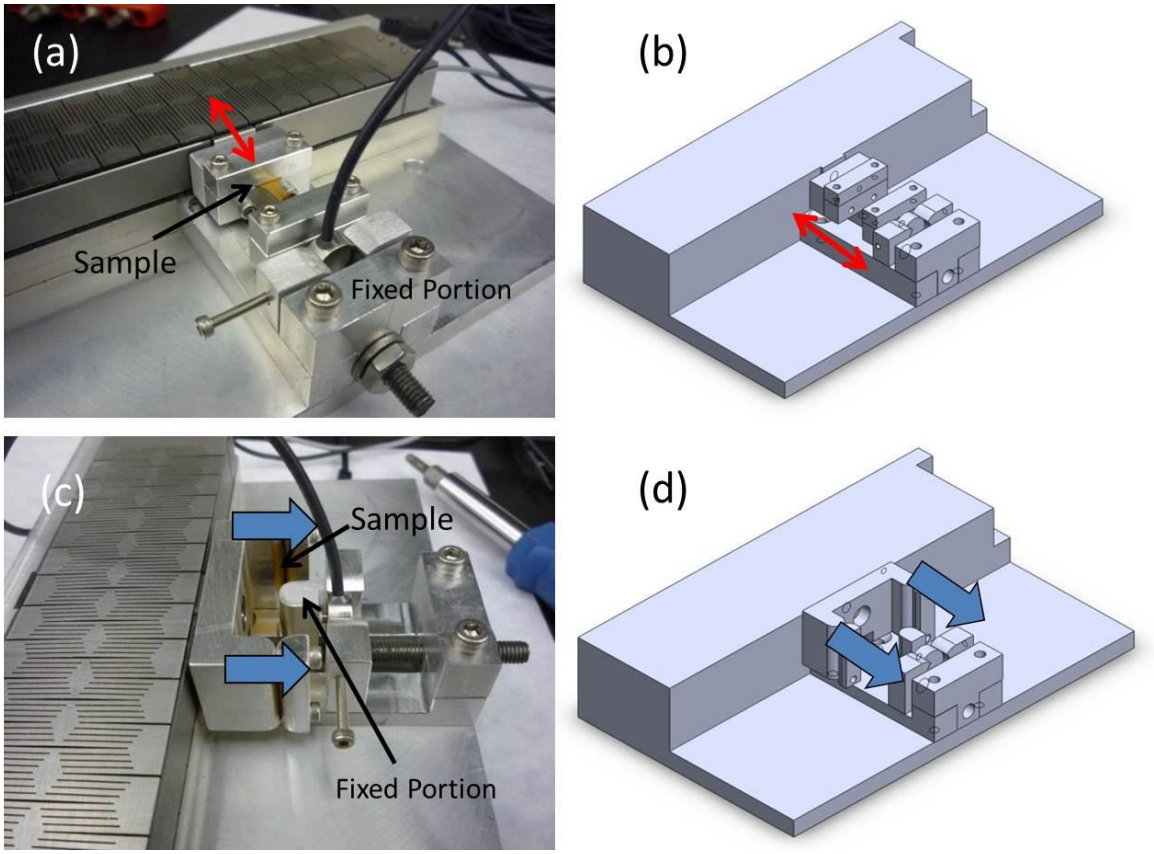

Figure 2.10 Cyclic fatigue tester for both tensile and bending testings: (a) Real product (b) CAD design of tensile tester; (c) real product and (d) CAD design of bending tester. All the arrows indicate the loading direction.

2.4. Summary

In short, this chapter introduced four different testing platform for electro-mechanical characterization of flexible electronics. For the sample in

nano/submicro size, the micro mechanical devices can be used for uni-axial and bi-axial loading tests. For the sample in macro size, the micro tester will be used for *in situ* monotonic tensile test, while the fatigue tester can be used for *in situ* cyclic tensile or bending testing purpose. Overall, we have developed systematic *in situ* electro-mechanical characterization methods for flexible electrodes and their nano components, and now all the samples in this dissertation can be tested using the tester described in this chapter.

Chapter 3

3. Size and rate dependent mechanical behavior in metallic nanowires

Metallic nanowires are the important building blocks inside the flexible electrodes, and full understanding of their deformation mechanism is essential and critical for their applications. As the dimensions of materials become smaller, the role played by free surfaces in their deformation and fracture becomes increasingly important due to the increasing surface to volume ratio. Very interesting phenomena, including size and rate dependent mechanical properties, can happen in small scale. In this chapter, the size-dependent strength in Ni NWs and size-dependent fracture mode in Cu NWs were illustrated first, and then the rate dependent strength has been investigated later on. Finally, atomic simulation was performed to provide mechanistic insights into the rate-controlling deformation mechanism in small scale.

3.1. Overview on size and rate dependent mechanical behavior in nanomaterials

One dimensional metallic nanowires (NWs) as important building blocks for flexible electrodes, nano-electromechanical systems (NEMS), and nano devices, have drawn considerable attentions recently.[55-58] Durability and reliability of these materials call for fundamental understanding of mechanical behaviors at the relevant small length scales.[59, 60] Compared to their macro scale counterparts, free surfaces play an important role in the deformation mechanism in nanoscale samples. Due to the high surface to volume ratio, the free surface could serve as both sources and drains for dislocations and also suppress dislocation storages within the volume. Meanwhile, surface oxides and defects are also more dominant in affecting corresponding mechanical behaviors. Therefore, some interesting and unusual mechanical phenomena could occur at the nanometer length scale, e.g., the strength of nanocrystals could be much higher than their bulk counterparts and fracture behaviors could be very different.

Size dependence in Young's modulus, strength and yield strength thus has been well recognized and predicted by theoretical and computational methods. With the help of molecular dynamics (MD) simulations, researchers were able to calculate the yield stress in different face-centered cubic (FCC) nanomaterials, e.g., Au, Ag and Cu. The calculated yield stress of these materials could be in the order of a few GPa, and the strength values have strong correlations with sample dimensions and surface structures.[61-65] However, the high strain rates inherent to the MD

simulations (10^7-10^9 /s) always lead to questions on the fidelity of such MD simulation in reflecting the deformation mechanisms in real experiments where the strain rate is typically around 10^{-3}-10^{-1} /s. Experimental results of semiconductor nanowires also have illustrated the size effects on Young's modulus and fracture strength. [66-68]

There have been extensive experimental investigations of size-dependence strength mechanical behaviors of metals at small length scales. In the 1950s, tension testing of metallic whiskers (nearly dislocation-free crystals) with micron-scale diameters showed dramatic strengthening as a function of whisker diameters.[69-71] With the advancement of experimental techniques, Fleck et al. revisited this important phenomenon in a series of experiments on yielding of copper micro-wires in both tension and torsion, inspiring many subsequent studies on size-dependent mechanical properties.[72] Stolken and Evans[73] and Lou et al.[74] reported higher strengths for thinner Ni foils subjected to monotonic and cyclic bending conditions and attributed this size effect to the plasticity strain gradient theories. Similarly, results from many nanoindentation experiments showed a very strong inverse relationship between the hardness and the indentation depth or size of the indentation.[22, 75-80] Pillar (with diameters ranging from micron to sub-micron regimes) compression experiments that circumvent the strain gradients inherent to conventional indentation and bending experiments were applied to nickel alloys,[25] pure nickel,[29, 81, 82] and gold[26, 31] samples, and results showed strong geometry dependence in the flow stress: for Au NPs, it is 0.8 GPa with 350 nm in diameter[26] and 1.0 GPa with 300 nm in diameter[31] ; and for Ni NPs, it is

1.0 GPa with 10 μm in diameter[29] and 3.4 GPa with 165 nm in diameter[82]. Recently, several innovative micro-electromechanical-systems (MEMS) set-ups have been built and offer more options for *in situ* uni-axial tensile testing performed inside various electron microscopes.[23, 48] The relatively uniform stress state in uni-axial tension makes the obtained experimental results easier to be interpreted and tensile fracture behaviors can also be systematically studied. Copper whiskers,[32] cobalt nanowires,[33] and gold nanowires[83] have been tested and clear size effect in strength was observed.

In addition to size-dependent high strengths, fracture behaviors of nanomaterials and associated fracture modes are also of great interests. While high strength could be achieved in a wide range of nanomaterials, their fracture behaviors especially the important ductile to brittle transitions were not thoroughly investigated thus warrant more systematic studies to understand the fundamental fracture mechanisms at the nanoscale. By simulating the dynamical failure of a three-dimensional notched crystal using molecular dynamics method, Abraham and Gao found the anomalous ductile and brittle fracture behaviors in face center cubic (FCC) crystals could be explained by a hyper-elastic model.[84] Kang and Cai simulated fracture behaviors of Si and Ge NWs, and found the observed ductile versus brittle fractures were well correlated to a simple parameter based on the ratio between the ideal tensile strength and the ideal shear strength.[85] Although temperature is traditionally considered to be an important factor in determining the ductile-brittle transition in metals, it was recently suggested by both simulations and experiments that size could also become another important factor concerning

fracture modes. It was found that fracture behaviors of silicon NWs depends on both temperature and NW diameter and below a critical diameter of 4 nm ductile fracture would occur regardless of the temperature.[86] The experimental results of micro-compression of hollow indium nanopillars also showed that the sample could become brittle once the indium sidewall thickness became less than 15 nm.[87]

While size dependent mechanical properties have been extensively investigated for face centered cubic (FCC) metallic materials by both experimental and theoretical approaches [26, 29, 31, 61, 88, 89], the strain-rate effects on mechanical properties of nanowires are still under-explored experimentally[90]. To fully understand the relationship between strength and strain rate, the rate-controlling deformation mechanism must be understood, and the kinetic rate theory could be used [91]. Two quantitative measures can be introduced to characterize the rate-controlling deformation mechanism: the athermal strength and activation parameters. While the athermal strength measures the elastic limit of material without the aid of thermal fluctuations, the activation parameters measures the probabilistic nature of transformation by thermal fluctuations when the applied load is below the athermal limit. The activation parameters include activation energy and activation volume. These two parameters can be determined both experimentally and theoretically. In experiments, the activation volume is typically determined by measuring the strain rate sensitivity. Lu et al. showed that nano-twinned copper has the high value of rate sensitivity ~0.02 and small activation volume down to $20b^3$ [92], and the same magnitude in activation volume has also been measured in nanocrystalline nickel sample by Ma et al.[93]. Meanwhile,

relatively small activation volume in copper nanopillars has been obtained under the uniaxial compression tests [27]. In computational models, the stress-dependent activation energy and activation volume can be calculated in a robust and efficient manner by using the reaction pathway exploration approach such as the nudged elastic band method. Zhu et al. calculated the activation energy and found that a small activation volume ($<10b^3$) leading to increased strain-rate sensitivities of flow stress in copper nanowires[59].

In this chapter, both size-dependent strength and fracture will be investigated in Ni NWs and Cu NWs. A simple silicon based micro mechanical device, as mentioned in Chapter 2, is employed to perform systematic uni-axial tensile test for these NWs with varying diameters and crystalline orientations inside a SEM chamber equipped with a quantitative nanoindenter. Engineering stress-strain curves were derived from nanoindenter load-displacement curves facilitated by a simple response subtraction method. Real time observations of the deformation and fracture processes and subsequent fracture surface analysis were then performed. Finally, atomic simulation was performed to provide mechanistic insights and better understanding into the rate-controlling deformation mechanism in small scale.

3.2. Size dependent mechanical properties in nickel nanowire

3.2.1. Sample preparation and experimental procedures

Ni NWs with different diameters were fabricated by electro-chemical deposition using nanoporous anodic aluminum oxide (AAO) templates.[94, 95] By carefully controlling the anodization condition and process,[96] AAO templates consits of ordered channels with uniform pore size ranging from tens of nanometers to hundreds of nanometers (in this work only the templates with 100-300 nm pore sizes were used) were made. The channel depths (AAO thickness) were usually about 40-50 μm, which will be the upper limit of the nanowire lengths. Electro-chemical deposition of Ni NWs into the AAO templates was accomplished using a two-electrode system (Figure 3.1a) with a graphite counter electrode at room temperature under a DC power supply (Extech™, voltage~0.8-1.5 V, current~0.01 A). Before deposition, a layer of silver (1-2 μm) was sputtered on one side of the AAO membrane, which served as the working electrode. Then the AAO membrane was mounted on a copper plate using insulating electrical tape with the conductive, metal-coated side facing the copper. The insulating tape covered the remaining copper plate and prevented unwanted deposition. The electrolyte used was a commercial $Ni(H_2NSO_3)_2$ based nickel electroplating solution (Technic™).

All the Ni NW samples tested in this paper can further be divided into two groups (~100 nm diameter Ni NWs and ~200-300 nm diameter Ni NWs), based on

the pore diameter of AAO templates used in electrodeposition and thus the final NW diameters. Transmission electron microscope (TEM) was first used to examine the microstructure and crystalline orientation of the fabricated NWs before actual mechanical testing. Freestanding Ni NWs on a TEM grid were obtained by wet etching of the AAO template in NaOH solution as shown in Figure 3.1b. The TEM select area diffraction (SAD) analysis (Figure 3.1c and d) of individual NW at different sample locations indicates that 100 nm diameter Ni NWs are single crystals with [111] orientation along axial direction while the 200-300 nm diameter Ni NWs are single crystals with [112] orientation along axial direction.[96]

A droplet of Ni NW solution was first dispersed in isoproponal by ultrasonication for 5-10 minutes. A small drop of this dispersed solution was then deposited on top of a Si wafer coated with a 5 nm thick titanium layer. Individual nanowires were subsequently picked up and placed across the sample shuttles using micromanipulators housed within a probe station (The Micromanipulator Co., Carson City, NV). Tungsten tips (The Micromanipulator Co., Carson City, NV) were used to perform the manipulation of the NWs since they were found to attach to the tips fairly easily via electrostatic interaction. A portion of each sample stage was coated with a thin layer of epoxy (HARDMAN Water-Clear Epoxy) to firmly clamp the sample after epoxy hardening process.

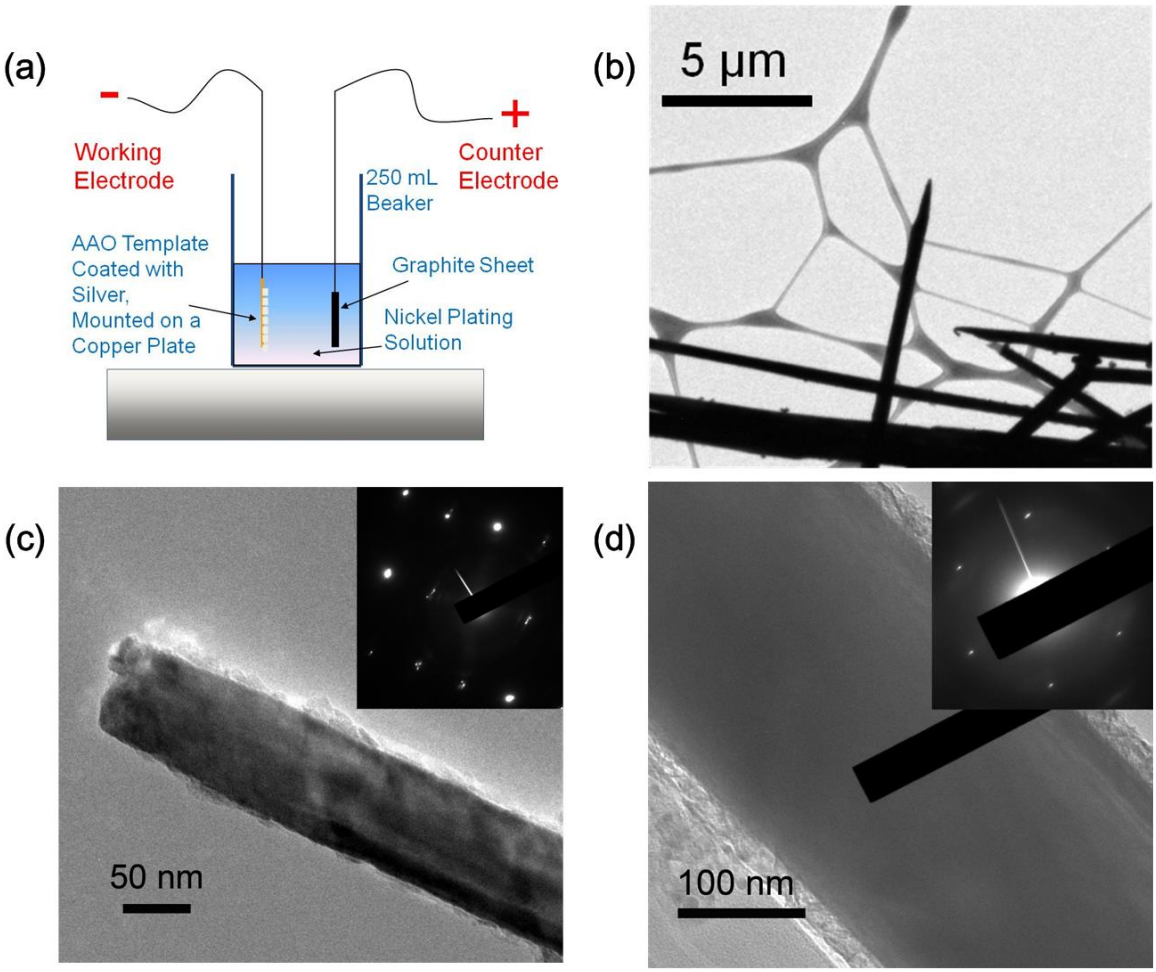

Figure 3.1Fabrication and TEM characterization of Ni NWs: (a) Schematic illustration of two-electrode system for Ni NWs electro-chemical deposition. (b) TEM image of individual free-standing Ni NWs. (c) TEM image of an as-fabricated Ni NW with a diameter ~100 nm. Inset is the corresponding SAD pattern, showing that it is a single crystal and its length direction is [111]. (d) TEM image of an as-fabricated Ni NW with a diameter ~250 nm. Inset is the corresponding SAD pattern, showing that it is a single crystal and its length direction is [112].

In situ tensile experiments for Ni NW properly placed on micro mechanical devices (mentioned in Chapter 2) were performed inside a scanning electron microscope (FEI Quanta 400 high resolution field emission SEM, FEI company, Hillsboro, Oregon) equipped with an InSEM® Indenter (Agilent Technologies, Oak

Ridge, Tennessee) system. The tensile tests were performed under displacement-control mode and the strain rate was fixed at $\sim 10^{-3}\ s^{-1}$. The maximum load applied to the device was ~0.5 mN, to make sure the force was high enough to break the samples. Monotonic loading or cyclic loading-unloading test can be performed, until the sample breaks. The load applied to and displacement of the top shuttle can be obtained from the high resolution quantitative nanoindenter. Once the geometry of Ni NW was measured, the stress-strain curve could be derived from recorded load-displacement data from the nanoindenter and a response substraction method.[48, 97] Due to the relative low stiffness of epoxy clamping portion, the displacement of deformed epoxy was taken into account. To ensure the accuracy of displacement measurement, a digital image correlation method was also utilized,[49] and all the results in this work have been corrected by this technique.

3.2.2. Results: high strength and size dependent strength

Uniaxial tensile tests for ten Ni NWs with different diameters (100-300 nm) and two different crystalline orientations ([111] for 100 nm diameter NWs and [112] for 200-300 nm diameter NWs) have been performed successfully. Four representative engineering stress-strain curves are shown in Figure 3.2a, and the strength values of all tested samples are listed in the Table 3.1. For all ten samples, the values of breaking strength are typcially high, in the range of 1-3 GPa. These values are much higher (>5 times) than the ultimate tensile strength (UTS) of Ni in bulk which is ~140-195 MPa.[98] However, the strength values are still far away from reaching the theoretical strength of the Ni material (Figure 3.2). It is also quite

obvious from the enigneering stress-strain curves of the four samples shown in Figure 3.2a and strength values shown in Table 3.1, that a clear size effect in breaking strength can generally be found with higher average strength for ~100 nm diameter Ni NWs compared to their larger diameter counterparts: for ~200-300 nm diameter group, the average breaking strength is 1.36±0.24 GPa; and for ~100 nm diameter group, the average breaking strength is 2.43±0.15 GPa.

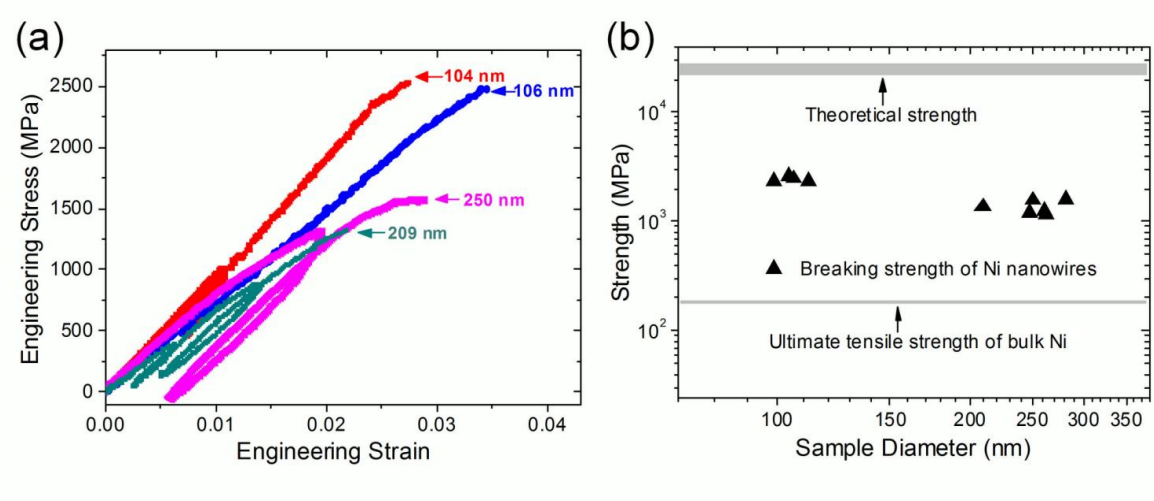

Figure 3.2 Representative engineering stress-strain curves and plot of strength vs. NW diameter: (a) Four representative engineering stress-strain curve of Ni NWs of varying sizes. (b) Strength plotted as a function of Ni NW diameters on log-log scale. The values are much higher than ultimate tensile strength of bulk material, but they are still far away from the theoretical strength of <111> or <112> oriented single crysal.

Table 3.1 Breaking strength and 0.2% offset yield stress of ten Ni NWs in this work.

Sample number	Length (μm)	Diameter (nm)	Breaking strength (GPa)	0.2% Offset yield stress (GPa)
1	3.62	282	1.60	1.32
2	3.41	263	1.16	0.95
3	3.39	261	1.26	1.13
4	3.10	250	1.57	1.22
5	2.93	248	1.21	1.02
6	3.23	209	1.37	1.20
7	3.41	112	2.33	1.99
8	3.30	106	2.46	2.11
9	3.13	104	2.57	2.29
10	2.43	99	2.35	2.03

In addition to the stress-strain curves, the evolution of sample morphology and surface structures was also recorded by SEM video during the deformation process in real time (Figure 3.3). As shown in Figure 3.3a, the particular Ni NW sample was loaded then unloaded twice before the final fracture. The initial slag of the NW sample (Figure 3.3b) was straightened after the load being applied. Very little changes in sample morphology and surface structures (slip bands etc.) were observed throughout the experiment, before a sudden fracture event occurred at relatively low strain level (~2% in this case). With the magnification of SEM imaging at ~55,000 x, there were no obvious changes in sample diameters and no sign of necking during the deformation process indicating lack of apparent ductility. However, upon further examination at even higher magnifications, fracture surfaces of the broken Ni NW were very rough and formed certain angle to the loading direction (also NW axis, Figure 3.3d and inset). This fracture surface morphology

presumably caused by localized shear process suggests limited plasticity involvement in the final stage of fracture.

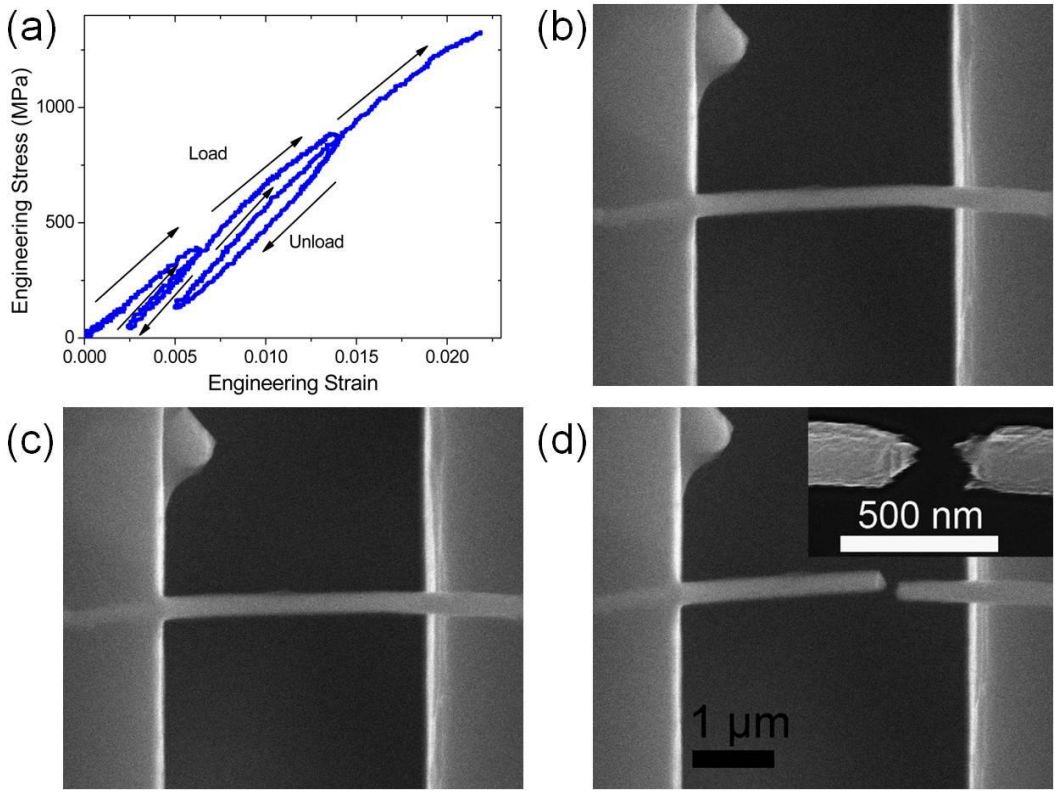

Figure 3.3 *In situ* observation of a Ni NW during tensile deformation: (a) Engineering stress-strain curve of a Ni NW with diameter of 209 nm, and the particular Ni NW sample was loaded then unloaded twice before the final fracture; (b) Initial slag of the Ni NW sample before loading; (c) The sample was straigthened after the loading of 1200 MPa being applied; and very little changes in sample morphology and surface strctures were observed. (d) Brittle-like fracture mode. Insert is the rough fracture surface of the broken sample, and limited necking and no obvious slip band can be found on the sample surface.

3.2.3. Discussion: Size dependent yield stress and CRSS

It is well known that plasticity of bulk Ni is mediated by dislocation based mechanisms thus extensive slip bands formation are typical surface features during deformation at the macro-scale. Earlier micron and sub-micron Ni pillar compression experiments also showed clear sign of slip bands formation during and after compression tests, demonstrating substantial dislocation mediated plasticity.[25, 29, 81] This is in sharp contrast to Ni NWs tested under uni-axial tension showing limited ductility and an apparent brittle-like fracture as discussed earlier (Figure 3.3). Careful examination of Figure 3.2a also reveals that most of the stress-strain curves shown are nearly linear with the slope of the curves kept almost as a constant (only a little bit of change of slope before failure), and no obvious yielding can be detected before final fracture shortly after reaching UTS in all of the samples tested (including the ones not shown in Figure 3.2a). These results are consistent to earlier real time SEM observations of the deformation and fracture processes.

Similar stress-strain curves and brittle fracture modes were found in recent tension tests of copper nanowhiskers.[32] It is clear that large-scale plasticity is not sustainable in such whiskers with good crystal quality and very few pre-existing dislocations and other critical defects. However, for Ni NWs investigated here, the underlying mechanisms are believed to be different since template assisted electro-deposition of metal NWs will inevitably introduce pre-existing dislocations,[99] and such samples are known to be prone to small amount of fabrication defects like voids and surface imperfections. It is quite plausible that crack nucleation from

critical defects would initially dominate the initiation of dislocation motion in Ni NWs under high stresses, leading to a more brittle-like deformation and fracture process as observed. Only under much higher stresses towards the end of the experiments can limited dislocation activities start to become active, rendering the highly localized final shear fracture morphologies.

Additionally, size dependence in strength or yield stress were widely reported in small scale single crystalline metal samples with different crystalline orientations, including size dependent yield stress observed in Ni alloys,[25] pure Ni,[29, 81] and Au pillar[26, 31] compression experiments. So it is not entirely surprising that our Ni NWs with 100-300 nm in diameters also showed size dependent high strength (1-3 GPa), which is still far away from the theoretical value. This deviation may be largely due to the fabrication defects in our samples as discussed earlier. In order to make straight forward comparisons to literature data in terms of size dependence in yield stress for single crystalline metals, a simple Hall-Petch like relationship ($\sigma_y \propto D^{-\alpha}$) was introduced to elucidate the scaling law where the parameter of grain size was replaced by diameter of NWs or nanopillars.[31] Since no apparent yielding was observed in our samples, 0.2% offset yield stress was used as shown in Figure 3.4a. The fitting parameter is determined to be 0.69, very close to the value of 0.69 for [111] Ni pillar,[82] 0.64 for [269] Ni pillar,[81] and 0.61 for Au single crystal.[31]

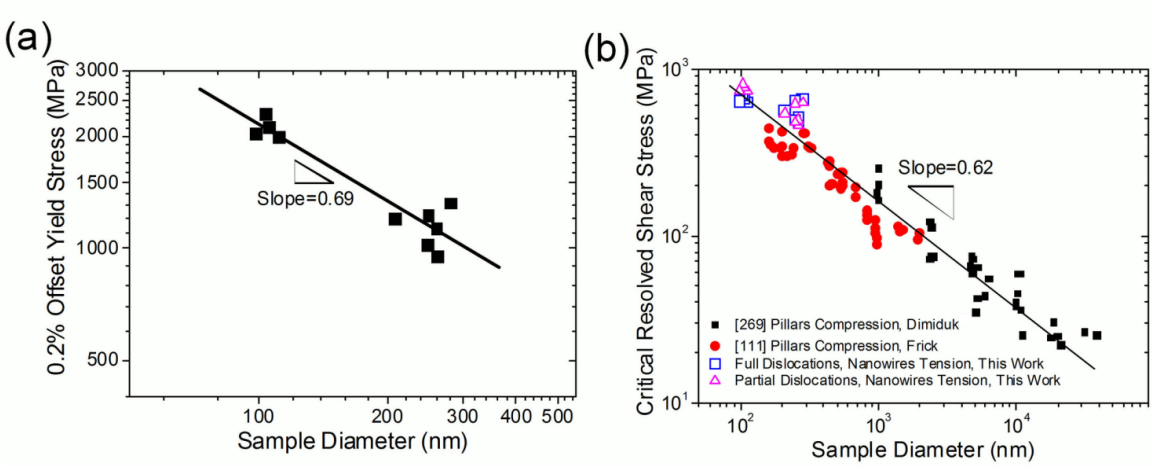

Figure 3.4 Plots of 0.2% offset yield stress vs. NW diameter and critical resolved shear stress (CRSS) vs. NW diameter on log-log scales: (a) 0.2% offset yield stress as a function of Ni NW diameters. The linear line is the fitting result using the power law $\sigma \propto D^{-\alpha}$, where α=0.69. (b) CRSS as a function of Ni NW diameter, and comparisons with previously reported values of Ni pillars.[81, 82] Fitting by the same power law in (a), the parameter α is 0.62.

Because of the different crystalline orientations of single crystalline Ni NWs ([111] for 100 nm diameter NWs and [112] for 200-300 nm diameter NWs) investigated in our study, the critical resolved shear stress(CRSS) were calculated in order to eliminate the effects of crystalline orientation and to make meaningful comparisons to other previously studied single crystals with different orientations. We have considered the cases for both {111}<110> type full dislocations and {111}<112> type partial dislocations in our calculations. As listed in Table 3.2, clear size effect in average CRSS can be seen to increase as sample diameters decrease for both full and partial dislocation cases. Figure 3.4b plots the CRSS from this study in comparison with other reported data for Ni pillars with different orientations (take the stress value corresponding to 3% strain for the [111] Ni pillars[82] and the 0.2%

offset stress for the [269] Ni pillars[81]), as a function of NW diameter. It can be clearly seen that the CRSS values for all of the results match reasonably well and can be simply described by a linear fitting with slope of 0.62. Most importantly, the size effect in CRSS is shown to be independent of the sample crystalline orientations.

Table 3. 2 Comparison of average CRSS for ~100 nm and ~200-300 nm diameter Ni NWs.

Group	Orientation	Average 0.2% offset yield stress (GPa)	Full dislocations {111}<110>		Partial dislocations {111}<112>	
			Schmid factor	CRSS (GPa)	Schmid factor	CRSS (GPa)
100 nm	[111]	2.11	0.272	0.573	0.314	0.661
200-300 nm	[112]	1.14	0.408	0.465	0.393	0.448

3.3. Size dependent fracture modes transition in copper nanowires

3.3.1. Sample preparation and experimental procedures

The Cu NWs were fabricated by solvothermal methods, which is commonly used in preparing nanostructures. This method has great potential because it can conveniently produce Cu NWs with excellent qualities such as large aspect ratio and single crystallinity at very low cost. The detailed fabrication process can be found in

the previous paper. [42] Crystalline structure of the as-grown Cu NWs was examined carefully using a JEOL 2100F TEM. Freestanding Cu NWs on a TEM grid were obtained by drying ethyl alcohol solution containing dispersed Cu NWs. TEM selected area diffraction (SAD) patterns obtained at multi-locations (Figure 3.5) of individual Cu NW indicated that such NWs were single crystals and the orientation was <110> along the growth direction. *In situ* uni-axial tensile tests of fabricated Cu NWs were performed using a recently developed micro mechanical device inside a FEI Quanta 400 SEM, and the details can be found in Chapter 2 and Session 3.2.1.

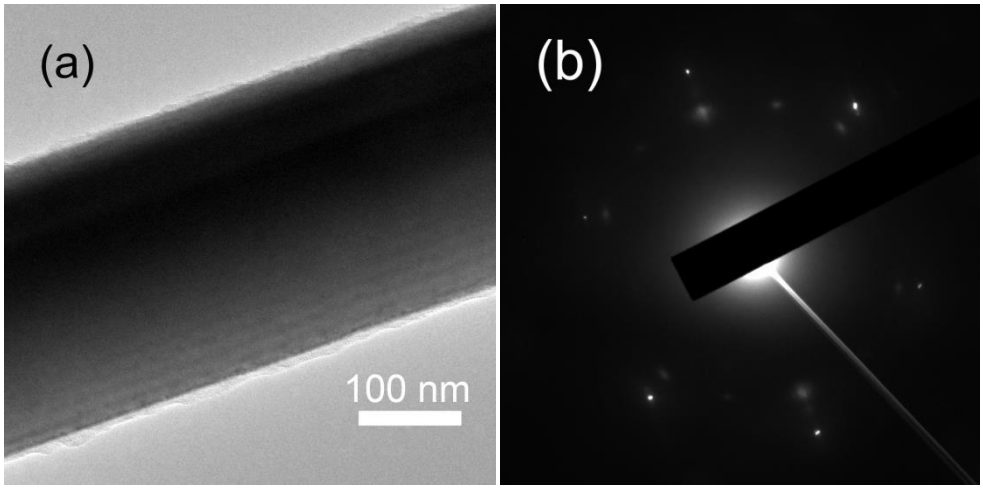

Figure 3.5 TEM characterization and experimental set-up: (a) TEM image of an as-fabricated Cu NW with a diameter of ~200 nm; (b) SAD pattern for this Cu NW, showing that it is a single crystal and its length direction is <110>.

3.3.2. Results: high strength and size dependent fracture modes

Quantitative tensile tests were successfully performed on ten Cu NW samples inside the SEM chamber, and forces and displacements of the samples were derived afterwards. The dimensions of the Cu NWs were measured before the test, in order to calculate the corresponding engineering stress-strain curves. Four representative stress-strain curves were shown in Figure 3.6a. The stress-strain behavior was found to be more or less linear until the occurrence of brittle fracture or yielding. Among these four curves, two of them (for NWs with 221 and 252 nm in diameter) failed at around 1% strain with very little plasticity, while the other two (for NWs with 291 and 614 nm in diameter) demonstrated yielding and apparent plasticity. Plastic deformation is especially pronounced for the sample with diameter of 614 nm, while the plastic strain was up to 30%. Coupled with in situ observations of the deformation processes inside SEM (Figure 3.7a-d) and higher resolution fracture surface inspections (Figure 3.7e and f) afterwards, fracture of the ten Cu NW samples successfully tested in this work can be clearly divided into two categories: five of them failed in brittle-like fracture mode while the other five were in ductile fracture mode (Table 3.3). This interesting phenomenon will be discussed in details in the next session.

The strengths of ten Cu NWs (from 131 to 655 nm in diameter) that were successfully tested were plotted as a function of sample diameters in Figure 3.6b and were also summarized in Table 3.3. The values of strength between 400 MPa-1000 MPa are quite high, which are well in excess of the yield stress of high purity

bulk single crystalline Cu. They are also higher than the yield stress of <234> oriented Cu microcrystals tested in tension. [100] However, the strengths are still far away from the ideal strength for pure <110> Cu, and they are also smaller than the values of the <110> oriented nanowhiksers ranging from 75 to 300 nm in diameter [32] and the <111> oriented nanopillars ranging from 75 to 165 nm in diameter (Figure 3.6b).[27]

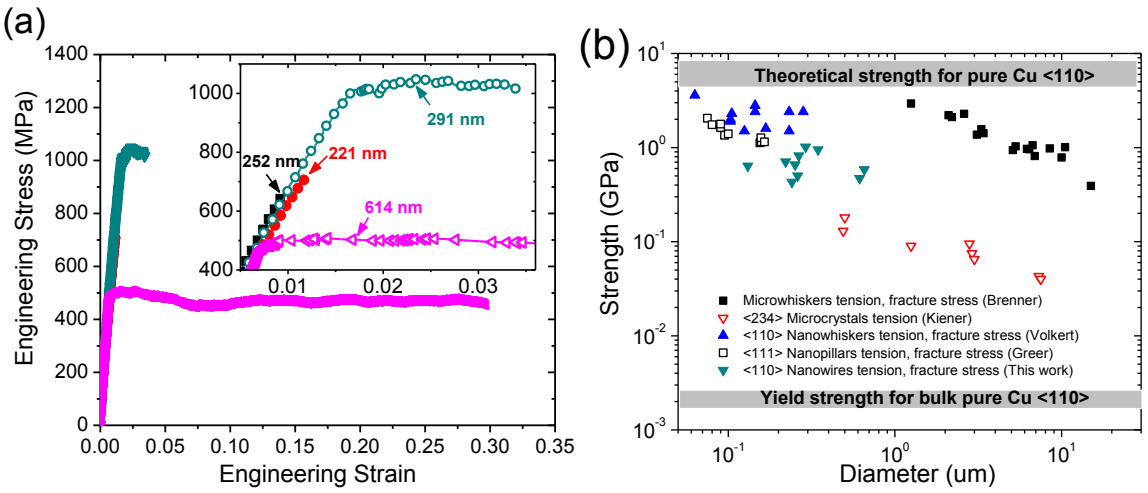

Figure 3.6 Representative engineering stress-strain curves and plot of strength vs. NW diameter: (a) four typical engineering stress-strain curves for Cu NWs of varying sizes; (b) strength plotted as a function of Cu NW diameters, and comparisons with previously reported values of strength of pure Cu single crystalline small scale samples under tensile deformation.

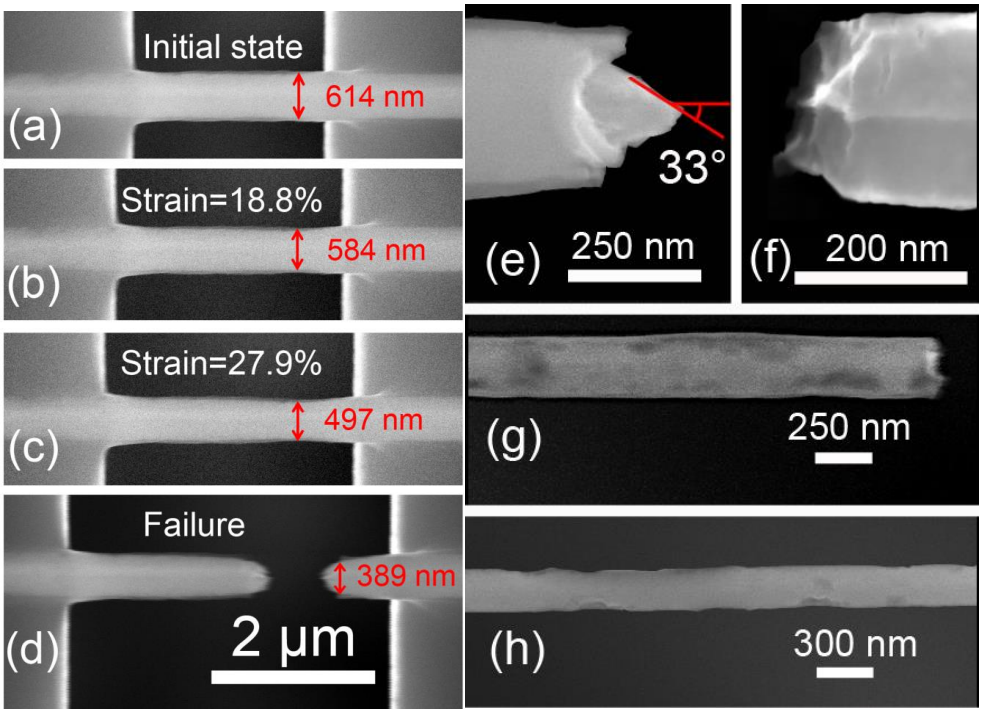

Figure 3.7 Ductile and brittle-like fracture modes: (a)-(d) *in situ* observation of a Cu NW during tensile deformation, decreasing of the NW diameter with increasing of the applied strain was clearly demonstrated; (e) ductile fracture surface, and the angle between the slip plane and loading direction is ~33⁰; (f) brittle-like facture surface, the surface is very rough and perpendicular to the loading direction; (g) oxidation of Cu NW surfaces failed in brittle-like fracture mode; (h) voids on Cu NW surfaces failed in brittle-like fracture mode.

3.3.3. Discussions: high strength and size dependent fracture modes

As mentioned above, the values of strength in ten Cu NWs are quite high, between 400 MPa and 1000 MPa. This result of high strength is consistent with previous results of FCC materials in such a micro/sub-micro scale, e.g., Au [26, 31], Ni [29, 82], and Cu [27, 32]. More interestingly, we notice the missing of the widely-reported size dependence of strength, which scales in a power-law fashion with sample diameters [27, 31], in ten Cu NW samples studied here (Figure 3.6b). This is

especially true for NW samples failed in brittle-like fashion (Table 3.3), implying the importance of these samples' initial conditions on their mechanical behaviors. For samples with stress-strain curves that demonstrated considerable plasticity, prolonged homogeneous plastic deformations were apparent from the steady flow region observed (Figure 3.6a). This is quite different from the <111> oriented nanopillars tested in tension where very limited homogeneous plasticity was followed by a large strain burst. [27] Therefore, considerable interactions among dislocations stored or multiplied in these samples dominated the deformation and subsequent fracture processes. For samples with stress-strain curves that demonstrated little plasticity, the recorded breaking strengths were considerably lower than the values obtained for nearly defect free <110> oriented Cu nanowhiskers.[32] This again indicated that the studied Cu NWs possessed non-negligible amount of inherent defects due to fabrication or sample manipulation.

For the five samples fractured in ductile mode, extended homogeneous plastic deformation right after the yielding point was evident with the NW diameter continuously decreasing as the increasing of applied strain (Figure 3.7a-c). This was followed by obvious localized necking before the sample broke near the necked region (Figure 3.7d). The fracture took place along planes with certain orientation relative to the tensile axis, and the angle is measured to be ~33 degrees as shown in Figure 3.7e. In all the five ductile samples, the particular angles were about 33-37 degrees. For full dislocations in <110> Cu stretched along <110> direction, the preferred slip systems with the maximum Schmid factor of 0.408 are (11 -1)[101] and (11-1)[011]. Therefore, the angle between the loading axis and slip plane of 35

degrees could be calculated. The experimental results of 33-37 degrees for 5 Cu NW samples fractured in ductile mode is thus well consistent with this theoretical prediction based on dislocation theories. It is therefore reasonable to believe that the apparent ductile fracture might be due to highly active dislocation interactions in these samples followed by typical shear fracture in metals. This evidence along with previous analysis on stress-strain curves of such samples clearly demonstrated that the plasticity and subsequent fracture were likely controlled by dislocation activities inside the sample volume.

In the other five samples, the facture surfaces were relatively flat although appeared rough at higher magnifications (Figure 3.7f), and they were generally perpendicular to the nanowire length/loading axis. *In situ* observations showed no sign of homogenous plastic deformation and subsequent necking process, the sample broke suddenly instead. The corresponding stress-strain curves demonstrated typical elastic-then-break behaviors of brittle materials (Figure 3.6a). All these evidences suggested that those samples fractured in a brittle-like mode with very limited dislocation activities. This fracture behavior in absence of clear signs of plasticity is quite similar to the results of Cu nanowhiskers [32] as well as the Cu microwhiskers, [70] although the magnitude of achieved strength was quite different as discussed earlier. Large-scale plasticity was thought to be not sustainable due to an absence of stored dislocation in these arguably defect-free whisker samples, and the strength of the whiskers was suggested to be controlled by the strength of the flaws for nucleating new dislocations. [32] The lower strength in our case might be attributed to two facts: surface oxidation layers and voids on

the surface. In Figure 3.7g, part of the surface is in dark color, suggesting the occurrence of oxidation which would definitely alter the structures and properties of Cu NWs. The presence of oxidation layer is consistent with our previous analysis of similar samples.[42] In Figure 3.7h, the appearance of the sample surface is not very smooth, and some surface voids can be clearly seen. The existence of pre-existing defects like oxidation layers and voids on NW surfaces enhanced the probability of possible crack/damage initiation from critical defects as explained in the weakest link model. [32, 70] Since the amount and the distribution of pre-existing critical defects were more abundant and widely-spread in Cu NWs, they have very little chance to reach ultra high strength levels even without significant plasticity mediated by dislocations.

The phenomenon of two different fracture modes is certainly very intriguing, because all the samples were taken from the same batch of synthesized materials. More interestingly, it seems that the "ductile-brittle" transition is size-dependent, or specifically we can say that the fracture modes depend on the diameter of the samples by carefully examining sample information in Table 3.3. The diameter of all the ductile samples listed ranged from 265 to 655 nm, which is higher than the diameters for the brittle-like samples (from 131 to 261 nm). One possible explanation to this seemly coincidental result is following: the increase in strength of crystals with sub-micron dimensions that are not initially dislocation free as in our cases could be explained by a dislocation starvation model, [26] with dislocations leaving the crystal more quickly than they could multiply giving rise to a dislocation starved state. Very high stresses would then be needed to nucleate new

dislocations either from surface or bulk leading to high strength observed. For samples with larger diameters, the dislocation multiplication process would be more efficient such that there is high probability of normal dislocation interactions mediated plasticity occurring (Figure 3.7a-e). [101] Clearly, this dislocation-starvation induced strengthening effect would be more dramatic in samples with smaller diameters such that higher stresses could always be reached in such samples. With the presence of critical defects such as oxidation layers and voids (Figure 3.7g-h), it seems quite possible that cracks could more readily initiate from such defects before reaching the stress level that could nucleate new dislocations and lead to more stochastic brittle-like fractures depending on distributions of critical defects. This hypothesis could be further corroborated by some earlier experimental results. In <234> Cu microcrystals (from 0.5 μm to 8 μm in diameter), all the samples showed large plastic deformation prior to facture (from 18% to 40%). [100] However, the tensile fracture behavior of <111> Cu nanopillars (from 75 nm to 165 nm in diameter) demonstrated instant necking in absence of apparent homogeneous ductility and then break right after they reached the ultimate tensile strength (UTS). [27] Fortunately, the size range of our Cu NW samples (from 131 nm to 655 nm) overlaps with the lower limit of microcrystals (0.5 μm) and the upper limit of nanopillars (165 nm), making it possible to observe this interesting "ductile-brittle" transition in fracture behaviors. Finally, it should be noted that due to different crystalline orientations and sample preparation techniques, above speculations and qualitative comparisons still need further developments and verifications through more systematic studies in the future.

Table 3. 3 List of mechanical properties of ten tested Cu NWs.

Sample Number	Diameter [nm]	Yield Stress [MPa]	Strength [MPa]	Failure Strain	Fracture Mode
1	131	--	639	1.03%	Brittle-like
2	221	--	708	1.18%	Brittle-like
3	241	--	430	0.71%	Brittle-like
4	252	--	658	0.96%	Brittle-like
5	261	--	501	0.79%	Brittle-like
6	265	744	819	5.60%	Brittle-to-ductile transition
7	291	1013	1017	3.43%	Brittle-to-ductile transition
8	346	961	950	16.2%	Ductile
9	614	488	471	20.6%	Ductile
10	655	625	585	29.7%	Ductile

3.4. Rate dependent mechanical properties in Ni NWs

3.4.1. Sample preparation and experimental procedures

All details concerning sample synthesis, mechanical testing and data analysis method can be found in previous Session 3.2. The tensile tests of Ni NWs with diameters from 80 nm to 300 nm were perform under displacement control mode, and the corresponding strain-rates were varied from 10^{-4} to 10^{-2} s^{-1}.

3.4.2. Results: rate dependent strength and strain rate sensitivity

Uniaxial tensile tests at room temperature (300 K) were performed for thirty Ni NWs with different diameters (80 to 300 nm) and two different crystalline

orientations ([111] NWs with diameter of ~100 nm and [112] NWs with diameter of ~200-300 nm). Six representative engineering stress-strain curves of Ni NWs under different strain rates are shown in Figure 3.8. All the stress-strain curves are nearly linear, with only a small change in the slope right before failure. No obvious yielding can be detected before the final fracture, which occurs shortly after achieving the ultimate tensile strength (UTS) in all of the tested samples (including those not shown in Figure 3.8. The UTS of the six samples are high, in the range of 1.2-3.4 GPa. A size effect in UTS can be found, with a higher strength level for Ni NWs of ~100 nm diameter than for counterparts with larger diameter. Specifically, the UTS is about 1.2-1.5 GPa for the diameter group of ~200 to 300 nm, and is about 2.5-3.4 GPa for the diameter group of ~100 nm. More importantly, in the same group with similar diameters, a higher strain rate always results in a larger UTS (Figure 3.8). It is clear that the smaller sample diameter and higher strain-rate give the higher UTS.

The size dependence of strength or yield stress was widely reported in small single-crystal metals and alloys, e.g. in pure Ni, Au, Cu and Ni alloy pillars tested by micro-compression.[26, 27, 29],[31] To compare the data in the literature in terms of size dependence of yield stress, a simple power law of $\sigma \propto D^{-\alpha}$, analogous to the well-known "Hall-Petch" relationship, was introduced to reveal the scaling trend, with the size of grains replaced by the diameter of NWs or nanopillars. Because no apparent yielding was observed in our samples, a 0.2% offset yield stress was used to define the yield point in this work. Figure 3.9 shows the relation between 0.2% offset yield stress and the NW diameter under the two different strain rates. The fitting parameter of the exponent α is ~ 0.7 in both cases (0.68 and 0.75), close to

the previous report for Au and Ni pillars.[31, 82] This consistency suggests that the exponent α is not significantly affected by strain rates for NWs in the size regime studied.

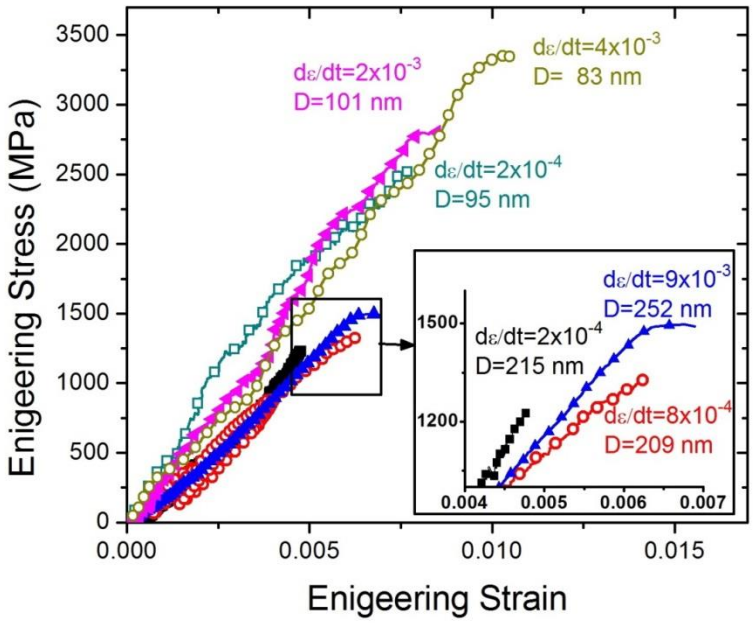

Figure 3.8 Six representive engineering stress-strain curves of Ni NWs under tension. In both groups of NWs with either ~100 nm or ~200-300 nm in diameter, the sample tested at higher strain rate has higher strength; and the average strength of 100 nm group is much higher than that of 200-300 nm group.

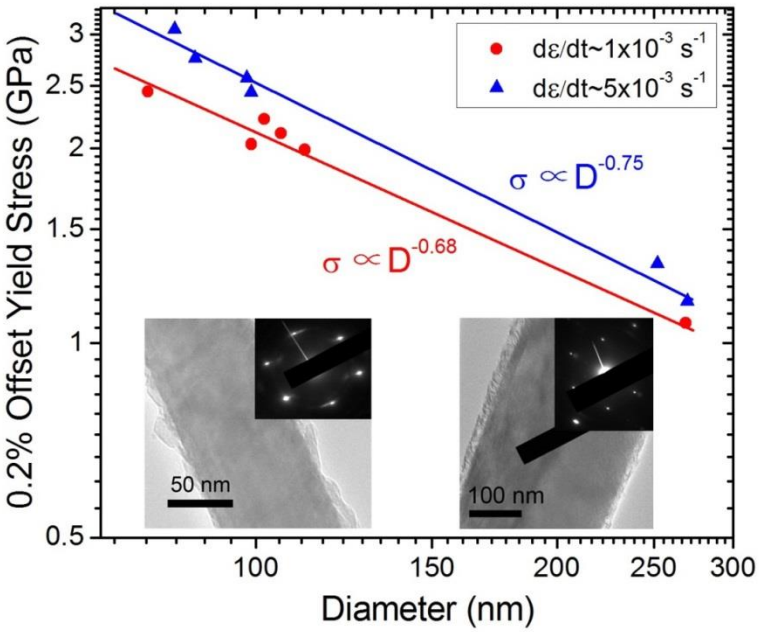

Figure 3.9 0.2% offset yield stress as the function of NW diameter, under two different strain rates. The NWs with smaller diameters have higher 0.2% offset yield stress, and the NWs with similar diameter under the higher strain rates have higher 0.2% offset yield stress. Insets are transmission electron microscope (TEM) select area diffraction (SAD) analysis: 100 nm diameter Ni NWs are single crystals with [111] orientation along the axial direction, and the 200-300 nm diameter Ni NWs are single crystals with [112] orientation along the axial direction.

To understand the strain-rate effects on yield stress, activation volume and rate sensitivity are two important parameters as discussed earlier. The rate sensitivity, *m*, is usually defined in terms of an empirical fitting formula between the yield stress σ and strain rate $\dot{\varepsilon}$,

$$\sigma = \sigma_0 \dot{\varepsilon}^m \qquad \textbf{Equation 3.}\ 1$$

where σ_0 is the reference stress constant. Physically, the activation volume measures the individual and collective nature of an underlying defect process that controls the plastic yielding, and it is proportional to the number of atoms simultaneously involved in a thermally activated process of defect nucleation or migration. By fitting the curve of strain rate as a function of yield stress, the activation volume *v** can be obtained according to

$$v^* = k_B T \frac{\partial \ln \dot{\varepsilon}}{\partial \sigma} \qquad \textbf{Equation 3. 2}$$

where k_B is the Boltzmann constant and T is the temperature.

In our experiments, we performed the uniaxial tensile tests at different strain rates, spanning three orders of magnitude, from 10^{-4} to 10^{-2} s^{-1}. Figure 3.10 show the experimentally measured 0.2% yield stress as a function of strain rate for two diameter groups of Ni NWs. By a linear fitting of the logarithm of yield stress versus strain rate based on Equation 3.1, the strain-rate sensitivity *m* is calculated for each Ni NW size group. For the group of ~200-300 nm, *m* = 0.080, while for the group of ~100 nm group, *m* = 0.098. These values are more than 15-fold greater than that of bulk coarse-grained Ni (~0.005) at room temperature (300 K), and at least 4-fold greater than that of nanocrystalline Ni (~0.02).[93] Notably, these values of strain-rate sensitivity are close to the recent result (~0.11) from Cu nanopillar compression experiments,[90] where sample sizes and experimental conditions (nanopillar diameter are 75 nm and 125 nm under the strain rate < 1×10^{-2}) are similar to our work. This finding suggests that as the sample size is reduced, not

only does the strength/yield stress increase, but also the strain-rate sensitivity markedly increases.

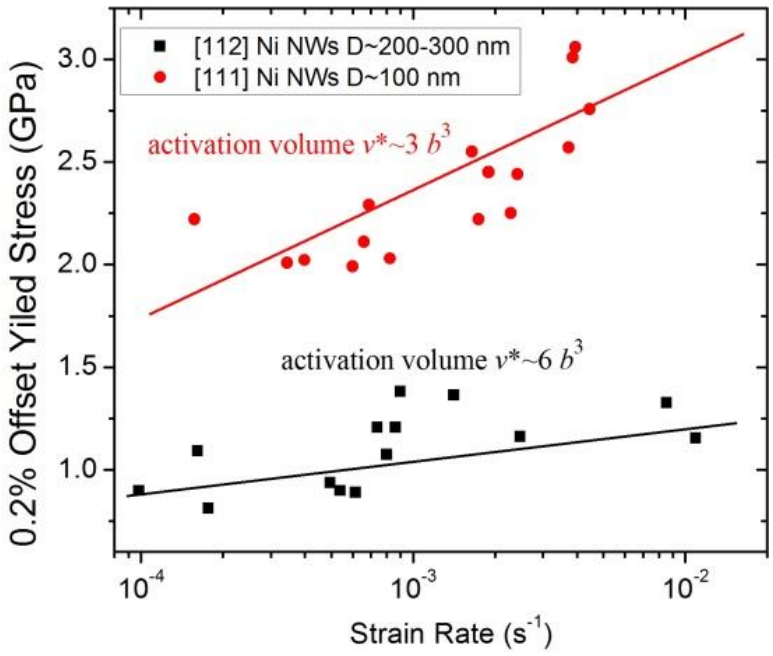

Figure 3.10 0.2% offset yield stress as the function of strain rate. The samples were grouped into two branches, 100 nm and 200-300 nm groups. For the samples of 100 nm group, the activation volume v^* is about $3b^3$, the strain rate sensitivity m=0.098; and for the samples of 200-300 nm group, the activation volume v^* is about $6b^3$, the strain rate sensitivity m=0.080. All the calculations are based on partial dislocation scenario.

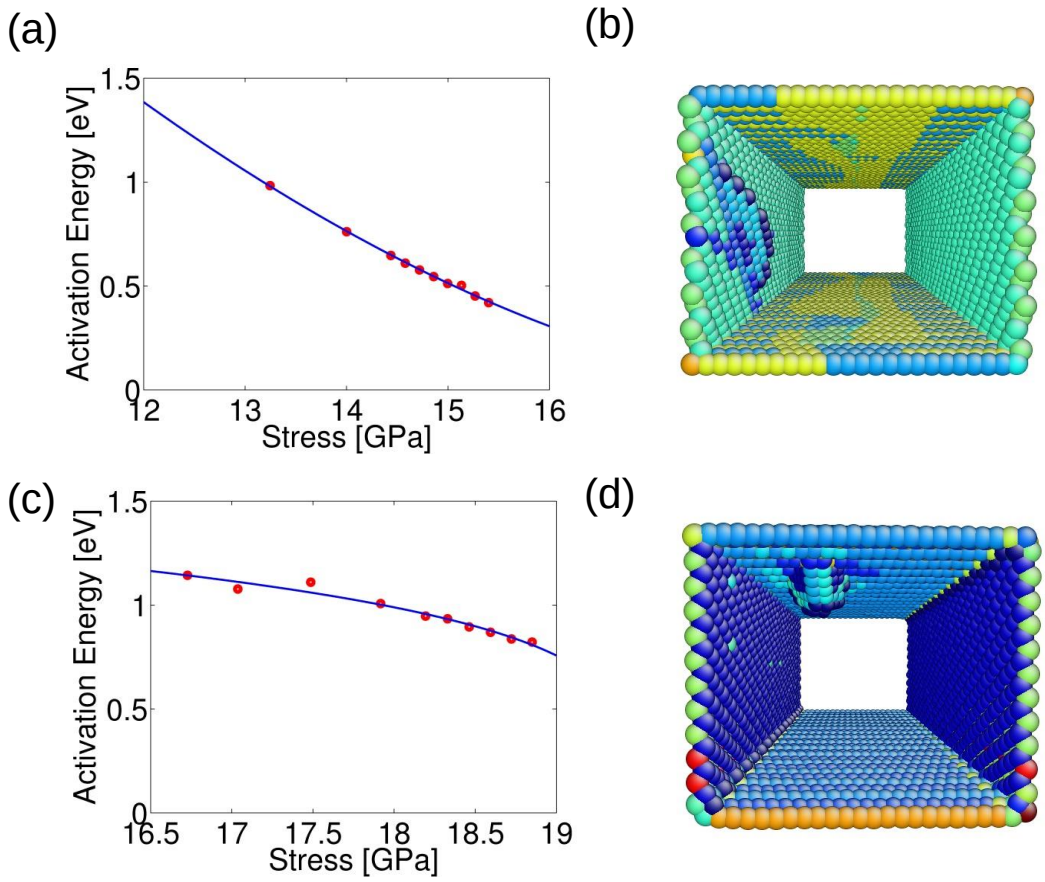

Figure 3.11 Atomistic study of surface dislocation nucleation in a Ni nanowire under uniaxial tension from free-end nudged elastic band calculations. The nanowire is about 10.5 nm long, the cross section is 4.5 nm x 4.5nm, and the system cosnists of about 27,000 atoms. (a) Stress-dependent activation energies around 0.7eV in a [112]-oriented nanowire, giving the nucleation rate relevant to laboratory experiments. Circles are calculated data points and the solid line is the fitting curve. (b) A representative saddle-point atomic configuration, showing a partial dislocation loop nucleating from the surface. Atoms are colored by the central symmetry parameter, showing both the free surface and stacking fault. (c) Same as (a) except for a [111] nanowire. (d) Same as (b) except for a [111] nanowire.

3.4.3. Discussions: Activation volume and surface nucleation

We further estimated the activation volume to be $\sim 6b^3$ for the group of ~200-300 nm and $\sim 3b^3$ for the group of ~100 nm on the basis of Equation 3.2, where b is the Burgers vector length of a {111}<112> partial dislocation in Ni. Unlike the body-centered cubic (BCC) metals such as Mo,[102] the trend of the smaller sample with the smaller activation volume is expected in FCC metals. In bulk FCC crystals, the forest dislocation interaction dominates the plastic deformation when the grain size is in the micrometer range, and the activation volume is relatively large ~100-$1000b^3$. Thus, the thermal contribution is nearly negligible to the yield strength. However, grain refinement from the micrometer to the nanometer scale can lead to a decrease in activation volume by two orders of magnitude. Ma et al. showed that the activation volume can be as small as $20b^3$ in the nanocrystalline Ni of 30 nm in grain size,[93] and the dominant deformation mechanism is changed to grain boundary-mediated dislocation activities. Moreover, Lu et al. obtained the similarly small activation volume $\sim 20b^3$ in the nanotwinned Cu samples,[92] and attributed the controlling mechanism to the twin boundary-mediated dislocation processes. In our single-crystal Ni NWs, the measured activation volume of $\sim 10b^3$ is on the same order of that in nanocrystalline and nanotwinned FCC metals. These measured small activation volumes suggest that the rate-controlling deformation mechanism is transitioning from the typical process of forest dislocation cutting in coarse-grained bulk metals to the nucleation-controlled dislocation process in nanostructured and nano-sized metals.[91] Generally, the controlling mechanism is expected to relate to

the interface dislocation process in nanocrystalline and nanotwinned metals, and to the surface one in small-sized nanowires.

To gain mechanistic insights into the measured high strain-rate sensitivity and small activation volume in Ni nanowires, we conducted the molecular dynamics (MD) simulations with an empirical interatomic potential of Ni[103] to identify the representative dislocation processes that might be strength and strain rate controlling. With these unit processes as input, we further performed the nudged elastic band (NEB) calculations to quantify the associated activation volumes for correlation with experimental measurements.[59, 60] For single-crystal Ni NWs with the cross-sectional size of ~10 nanometers, our MD simulations indicate that the individual dislocations inside NWs are not stable and tend to escape from the free surface, leading to dislocation starvation. Such dislocation-starved state arises owing to the large attractive image force of the free surface that destabilizes the dislocation inside the NWs, as well as the lack of effective mechanisms of dislocation blocking and multiplication within the small-sized NWs. To sustain the continued plastic deformation, the free surface of the nanowire acts as a source of dislocations. The representative unit process typically involves the dislocation nucleation from a free surface, gliding into the bulk, and annihilation at the opposite free surface of the NW. Among these three steps, the surface dislocation nucleation is most difficult and thus rate controlling.

Using the free-end NEB method,[59, 60] we calculate the activation energy of surface nucleation as a function of the applied tensile stress for both [112] and [111]-orientated Ni NWs, as shown in Figure 3.11 a and c. The activation volumes

are then estimated by taking the numerical derivative of activation energy with respect to stress. Notice that the activation volume is also a function of stress. Thus we define the yield stress as the tensile load giving the activation energy of 0.7eV for surface dislocation nucleation; this characteristic activation energy corresponds to $\sim 30 k_B T$ at room temperature, giving the nucleation rate relevant to the laboratory experiments according to transition state theory. On this basis, we obtain the activation volume of $2.4b^3$ and $2.1b^3$ for the [112] and [111] nanowire, respectively**.** Figure 3.11 b and d show the corresponding saddle-point state with a partial dislocation loop nucleating from the NW surface. Our studies of dislocation nucleation from other side faces indicate that the above results of calculated activation volumes are insensitive to the specific nucleation site on the surface.

To gain a physical understanding of the characteristically small activation volume associated with plastic yielding in FCC Ni NWs, we note that the atomic volume enclosed by the dislocation loop in Figure 3.11 b and d represents the activation volume of surface nucleation. In a thermally activated process, the resolved shear stress does work on this volume to lower the activation energy and thereby facilitates dislocation nucleation. Our calculated activation volumes fall in the range of 1-10b^3, consistent with the previous atomistic study of surface dislocation nucleation in FCC Cu nanowires.[59, 60] Compared to coarse-grained Ni, the reduced activation volume and correspondingly increased rate sensitivity in small-sized NWs can be attributed to the ultra-high yield stress on the order of Gigapascals. As a result, the work done by such ultra-high stress on a small activation volume of surface nucleation is sufficient to lower its activation energy to the order of 0.7eV, in

order for the nucleation rate and associated plastic strain rate matching the externally applied loading rate.

However, we note that the tensile yield stresses in our NEB calculations (i.e., the stress of surface nucleation with activation energy around 0.7eV) are around 15GPa. They are markedly larger than the experimentally measured values. To explain such a discrepancy, we propose that for the nanowires in experiments, their yielding is controlled by the bulk and surface dislocation processes collectively. The former process usually involves the cutting of forest dislocations, giving the relatively low yield stress and large activation volume. In contrast, the latter corresponds to the high yield stress and low activation volume. Our atomistic modeling only addresses the latter process, owing to the limited computational resources. In experiments, the nanowires with two different diameters (100nm versus 200-300nm) reveal the size dependence of yield stress and activation volume. We attribute such a size effect to the transition from the bulk-controlled to surface-controlled dislocation process with decreasing size of nanowires. A similar size effect has been shown previously in the study of nanotwinned copper with different twin lamellae thicknesses.[92] In addition, we note that the temperature effects on activation energy and activation volume have been recently studied in detail.[59, 60],[104, 105] However, in order to bring out the essential physical effect without additional complications, we only study in this Letter the zero-*K* activation energy and activation volume. Corrections accounting for the finite temperature effects would not reconcile the discrepancy in measured and calculated yield strengths. Hence, we rationalize both the size effect

and experiment-modeling difference in terms of the transition between the bulk and surface-controlled dislocation processes.

3.5. Summary

In summary, we have investigated mechanical behaviors of single crystalline Ni nanowires and single crystalline Cu nanowires under uniaxial tensile loading inside a SEM chamber. Engineering stress-strain curves were obtained and *in situ* observations of deformation and fracture process were realized in real time.

For Ni NWs, limited plasticity and brittle-like fracture observed were attributed to possible earlier dominance of crack initiation from critical defects over dislocation activities. More importantly, we demonstrated both size and strain-rate dependence on yield stress of single-crystalline Ni NWs with varying diameters (from 100 nm to 300 nm). The experimental results show a very high strain rate sensitivity in the order of ~0.1 and a very small activation volumes in the order of $\sim 10b^3$ for these Ni NWs, and such findings are confirmed by atomistic simulations.

For Cu NWs, considerably high strengths/yield stresses were found in all of the ten samples. Most interestingly, two different fracture modes, namely ductile and brittle-like fractures, were found in the same batch of samples. The larger diameter NW samples could have higher probability of dislocations interactions, which facilitate ductile deformations and fractures observed in these samples. While higher propensity to nucleate cracks in smaller diameter NW samples were thought to be responsible for the observed brittle-like fractures. However, the strengths of

these Cu NWs failed in brittle-like fashion are still far away from the ideal strength of <110> pure Cu due to pre-existing surface defects such as oxidation layers and voids.

It is believed that our combined experimental and simulation results provide some further insights into the important yet complicated strength-limiting, size effects, fracture mode transition and rate-controlling deformation mechanisms for nanoscale metals.

Chapter 4

4. Fracture and fatigue behavior of macro ITO-base and CNT-based electrodes

Understanding the electro-mechanical behaviors of flexible electrodes is crucial for reliable operation of flexible devices under large deformation. In this chapter, *in situ* electro-mechanical tensile tests are performed for both ITO-based and CNT-based electrodes inside the scanning electron microscope (SEM). The good combination of transparency and conductivity enable ITO to be the most common material for flexible electrodes, but its brittleness also limits its wide application. By *in situ* electro-mechanical tensile measurements and coherent mechanics modeling, we try to understand the fracture cracking mechanics and improve its performance by structural modification in ITO-based electrodes. Meanwhile, CNT is considered to be the candidate to substitute the traditional ITO material. In this work, two types of CNT-based electrodes are selected and studied. The monotonic and cyclic loading

are applied to the sample, the crack initiation and propagation, crack density evolution and the corresponding electrical resistance variation were systematically investigated. Finally, we will compare these ITO-based and CNT-based electrodes and make a conclusion on the results.

4.1. *In situ* experiments on fracture cracking behavior of ITO thin film

4.1.1. Fracture cracking of ITO on polymer substrate

Fracture cracking of thin brittle films, e.g., ITO, on flexible substrate is a new research direction in the past few years. Fracture of thin brittle films on rigid substrates (e.g., Si) has been a focused topic in the discipline of materials science and mechanics in the past two decades, largely originated from the context of microelectronics.[106-110] These studies shed important lights on but cannot fully capture the characteristics of the fracture mechanisms of thin brittle films (e.g., ITO) on polymer substrates used in flexible electronics. For example, ITO is more than two orders of magnitude stiffer than typical polymers (e.g., polyimide), while electronic materials in microelectronics have comparable stiffness. Furthermore, flexible devices are often subject to deformation (up to 10%) much larger than that traditional microelectronic devices typically undergo (< 1%). These two distinctions cause the material response of ITO thin films on polymer substrates different from that of brittle films on rigid substrates, which therefore requires new efforts to

describe its characteristics. A growing literature exists on the rupture of thin metal films on polymer substrates.[111-118] Metal film necking and metal/polymer interfacial delamination have been shown as the major fracture mechanisms. Unlike the ductile failure of thin metal films on polymer substrates as a result of diffusive necking, the fracture of brittle ITO thin films on polymer substrates results from channel cracking, which in turn often interplays with the delamination along the ITO/polymer interface. Existing studies on the brittle fracture of ITO thin films on polymer substrates under tension include the fragmentation tests in which the crack density evolution as a function of the applied strain is monitored.[9, 119] The cohesive toughness of the ITO films and the adhesive toughness of the ITO/polymer interface can be estimated based on the experimental data from fragmentation tests.[120] The variation of electrical resistance due to ITO cracking has also been studied.[12, 121, 122] Other mechanics models investigate the effect of the large film/substrate stiffness ratio on the cracking of thin brittle films on compliant substrates.[123-126]

In our study, we perform *in situ* mechanical and electrical tests of ITO thin films deposited on polyimide substrates inside SEM, in which both the evolution of the crack density in ITO thin films and the resulting variation of the electrical resistance of the ITO thin films are monitored real time as a function of applied tensile strain. Simultaneous *in situ* mechanical and electrical tests are of particular importance to correlate crack initiation and propagation with its resistance change, and to avoid the unloading-induced partial or full closure of cracks in the ITO thin film in *ex situ* tests. We further conduct mechanics modeling to simulate the tensile

failure process of ITO thin films on polymer substrates, and apply the model to the experimental data to compute the critical but hard-to-measure properties, such as the cohesive toughness and fracture strength of the ITO thin films and the adhesive toughness of the ITO/polyimide interface. By combination of these experimental and simulation results, we aim to better understand the governing failure mechanism of ITO/polymer structure (i.e., ITO channel cracking versus ITO/polymer interfacial delamination).

4.1.2. Sample preparation and experimental method

ITO thin films were deposited on polyimide substrates (Dupont Kapton 50NH, 12.7 um in thickness) by e-beam evaporation. The resulting ITO/polyimide laminates were then cut into rectangle strip samples for in situ tests, with gauge length ~13 mm and width ~3mm. Mixed ITO powder (In_2O_3 and SnO_2, weight ratio of 90%:10%, density of 7.14 g/cm^3) was used as the evaporation sources in a Sharon E-beam evaporator. The deposition rate was kept at 1~3 Å/s and chamber pressure was at ~1×10^{-5} Torr. Before loaded into the chamber, polyimide substrates were cleaned in an ultrasonic cleaner for 10 minutes with acetone and ethanol and then dried with nitrogen gas. The thickness of ITO thin films were determined by an atomic force microscope (Pico-Plus AFM, Agilent Inc.), using the contact mode. Samples with two ITO film thicknesses (200nm and 80nm) were tested in SEM. The *in situ* electro-mechanical tests were performed inside the SEM, and the details of experimental method can be seen in the Chapter 2.

4.1.3. *In situ* SEM observation of crack initiation and propagation in ITO films

From in situ SEM observation, the unloaded ITO thin films were smooth, without any appreciable cracks. As the tensile strain increased to a threshold value (e.g., 1.59% for 80 nm thick ITO films), small channel cracks started to initiate at certain locations in the ITO film and then grew along the sample width direction (perpendicular to the tensile load direction). Figure 4.1 illustrates the typical process of crack initiation and propagation as the tensile load increases. Here, the ITO film thickness is 80 nm. For example, a crack tip was found near the top edge of the blue rectangle box in Figure 4.1a at the tensile strain of 3.68% and this crack propagated downward and advanced outside of the same blue rectangle box at the tensile strain of 4.70% (Figure 4.2b). Meanwhile, a channel crack not existing in the view of Figure 4.1a propagated upward with its tip slightly above the top edge of the blue rectangle box in Figure 4.1b. Similar crack propagation is also evident when comparing the red rectangle box in Figure 4.1b and c, as the tensile strain increased from 4.70% to 5.85%.

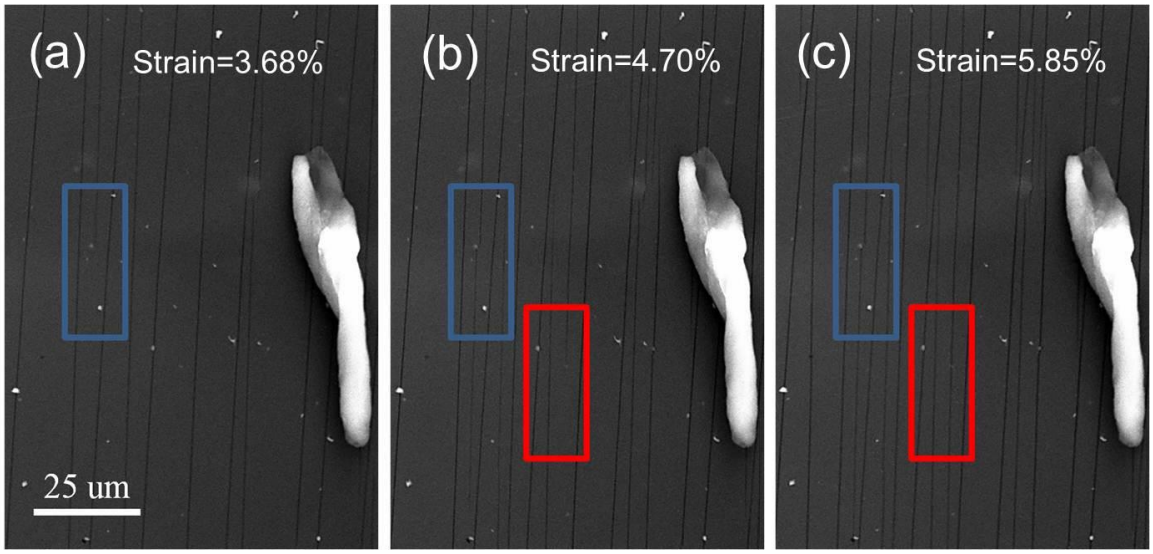

Figure 4.1 Crack initiation and propagation during *in situ* tensile test. A crack tip was found near the top edge of the blue rectangle box in (a) strain=3.68% and this crack propagated downward and advanced outside of the same blue rectangle box in (b) strain=4.70%. Similar phenomena is also shown in the red rectangle box in (b) strain=4.70% and (c) strain=5.85%. The dust in the right corner is used as the reference for *in situ* observation.

4.1.4. Crack density evolution and measurement of resulting change in sample electrical resistance

Figure 4.2 shows a series of snap shots of the polyimide supported ITO film to illustrate the increasing number of cracks in the film as the tensile load increases. Here the ITO film thickness is 80 nm. At small tensile strain (e.g., 0.55%, Figure 4.2a), the ITO film remained intact. Above a threshold tensile strain for crack initiation (1.59%, Figure 4.2b), channel cracks started to emerge in the view. As the tensile strain increased (e.g, Figure 4.2c-e], more channel cracks initiated and propagated through the sample width. It was found that the channel crack distribution in the ITO film is quite uniform along the sample length direction (also

the tensile load direction), suggesting the rather uniform elongation of the polyimide substrate. The sample was further stretched until the polyimide substrate ruptured into two halves. Figure 4.2f shows the ITO fragments near the sample rupture location. Note the obvious delamination along the ITO/polyimide interface near the edges of the ITO fragments.

To quantitatively characterize the ITO cracking under tensile strain, we define the crack density as the number of channel cracks in ITO film per unit length in the tensile load direction. In all data reported hereafter, the crack density of the samples is calculated as the average of crack density values obtained from at least three SEM images of the cracked ITO thin film in different random locations. Figure 4.3 plots the crack density in an 80 nm thick ITO film on a polyimide substrate as well as the resulting resistance variation of the ITO thin film as a function of the applied tensile strain. As shown in Figure 4.3, once the onset of crack initiation starts, the crack density first increases significantly as the tensile strain increases, and then gradually saturates at about 190 mm^{-1} as the tensile strain approaches to 5.85%. Also evident in Figure 4.3, the electrical resistance of the ITO thin film remains nearly unchanged when the applied tensile strain is relatively small.

For example, when compared with the as-fabricated ITO film, there is less than 2.5 times increase in resistance for a tensile strain less than 3%. In other words, the ITO thin film remains electrically conductive when subject to a modest elongation. As the applied tensile strain further increases, the ITO electrical resistance first rises gradually, and then shoots up dramatically as the tensile strain

approaches the value at which the crack density saturates. Such a correlation between the evolution of crack density and the change in electrical resistance in the ITO thin film under tension can be explained as follows. At the onset of crack initiation, many channel cracks start to nucleate but have not fully propagate through the whole sample width. As a result, the electrical conductance of the partially cracked ITO film remains nearly unchanged as a current can percolate through the whole ITO conductor. As the applied tensile strain increases modestly, the short channel cracks nucleated in the ITO thin film start to advance through the width of the samples, but the opening displacement of these channel cracks is relatively small, as evident by the rather thin crack lines in the SEM images (e.g., Figure 4.2b and c). When the crack opening is small, the local irregularity of the macroscopically straight channel cracks (e.g., the zigzag grain boundaries in the ITO thin film) may keep the ITO fragments in contact at certain locations in the wake of the channel cracks, and it is also likely that at certain locations the channel cracks have not fully developed to reach the ITO/polyimide interface thus the ITO thin film is not completely fragmentized. As a result, the ITO thin film remains conductive and its electrical resistance only increases modestly. As the applied strain further increases, channel cracks in the ITO thin film are fully developed, resulting in larger cracking opening (as shown by the thicker cracking lines in Figure 4.2d-f). Our further measurements of the total crack length and crack opening in the ITO thin film as a function of the applied strain further confirm the above explanation. That is, the total crack length increases drastically at small strains (corresponding to channel crack initiation) and such increases in total crack length diminish

significantly (corresponding to the fully developed channel cracks) when the applied strain is beyond about 4% (at which the ITO resistance starts to increase dramatically). Further increase of the ITO resistance is shown to be consistent with the continuously increasing crack opening.

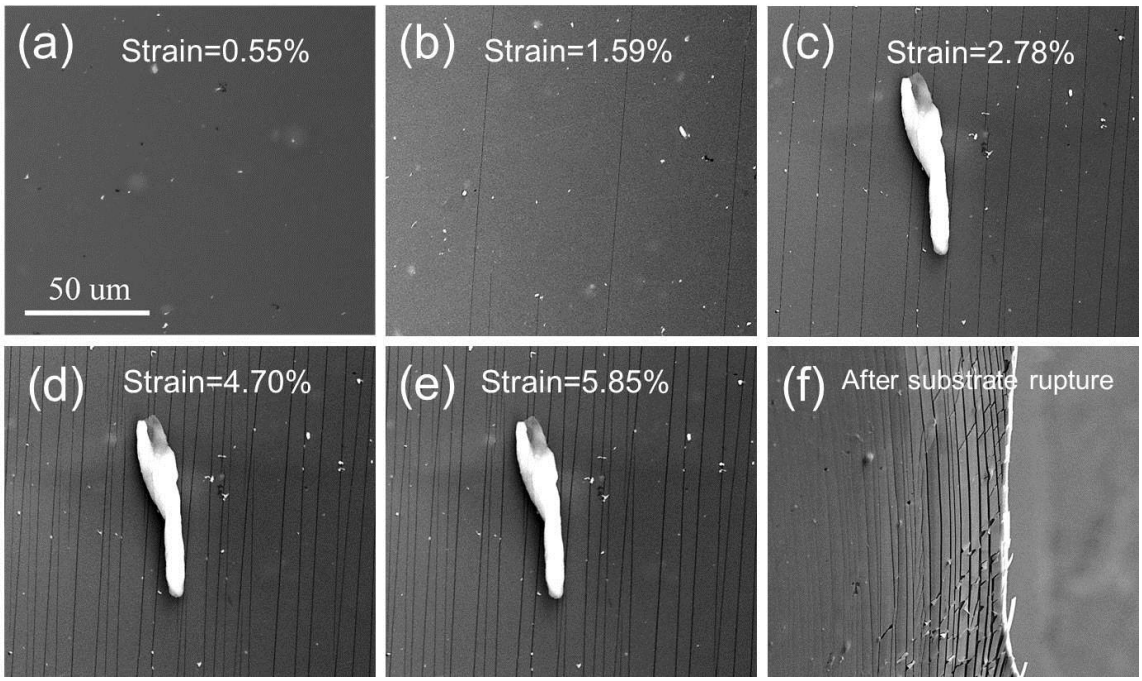

Figure 4.2 Snap shots of polyimide-supported ITO film under increasing tensile strain. Note the onset of channel crack initiation at 1.59 % tensile strain (b) and the increasing crack density as the tensile strain increases. No appreciable increase of crack density when tensile strain increases from 4.70% to 5.85% (d-e), indicating the saturation of channel cracking in the ITO film. (f). ITO fragments near the sample rupture location. Note the obvious delamination along the ITO/polyimide interface. Here ITO film thickness is 80 nm.

Also as evident in Figure 4.2f and further predicted in the simulations, the ITO fragments partially delaminate from the polyimide substrate. Consequently, the conductance of the ITO thin film is nearly cutoff. As to be further explained later, the

interfacial delamination mitigates the tensile stress transferred from the substrate to the ITO film, therefore prevents further initiation of channel cracks, resulting in the saturation of the crack density.

4.1.5. Thickness dependence of crack density in ITO thin films

Figure 4.4 plots the crack density in the ITO thin films as a function of applied tensile strain for film thickness of 200 nm and 80 nm, respectively. For each thickness, two samples were tested. It was found that the crack initiation in a thicker ITO film occurs at relatively smaller applied tensile strain than that for a thinner ITO film. However, the saturated crack density of the thicker ITO film is lower than that of the thinner ITO film. Assuming a brittle nature of ITO film fracture, the critical tensile strain to initiate cracking in an ITO thin film scales inversely with the square root of the length of the largest pre-existing defects in the film. For a thicker ITO film, it is more likely to have larger initial defects (e.g., voids, missing grains, or embrittled grain boundary during deposition), and therefore, entails a relatively lower onset strain of crack initiation. The thickness dependence of the crack density will be explained in detail later in through a fracture mechanics analysis.

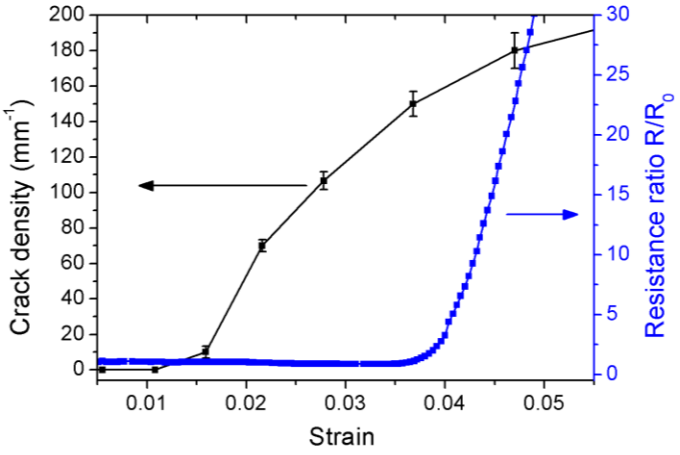

Figure 4.3 The crack density and the variation of electrical resistance of an 80 nm thick ITO film deposited on polyimide as a function of the applied strain. R_0 denotes the electrical resistance of the unloaded ITO thin film.

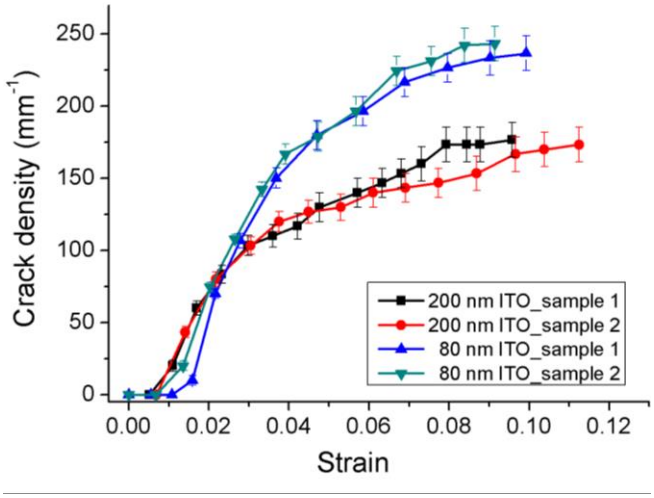

Figure 4.4 Crack density as a function of applied strain for ITO thin films with thickness of 80nm and 200nm, respectively. Two samples were tested for each film thickness.

4.1.6. Mechanics modeling

We next establish a mechanics model to use the *in situ* experimental data of ITO crack density evolution to compute the critical but hard-to-measure properties of the ITO/polymer laminates, such as the cohesive toughness and fracture strength of the ITO films and the adhesive toughness of the ITO/polyimide interface. We also offer a mechanistic understanding of the thickness dependence of the saturated ITO crack density.

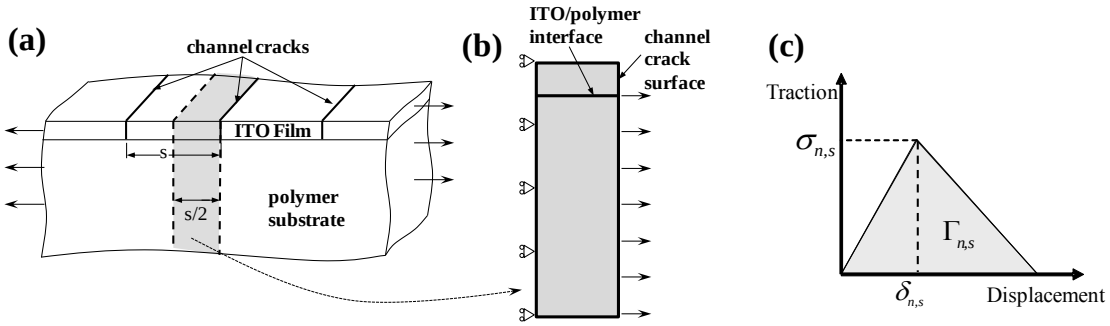

Figure 4.5 (a) Schematics of the simulation model. (b) Unit cell used in finite element simulation. (c) The traction-displacement laws used to model the ITO/polymer interface.

Figure 4.5 depicts the finite element simulation model. Under tension, a thin blanket ITO film on a polymer substrate is subject to channel cracking (Figure 4.5a). For simplification, we assume the channel cracks in ITO are uniformly spaced (i.e., the crack density is given by $1/s$, where s is the width of ITO fragments). The ITO/polymer laminate is taken to deform under the plain strain conditions. Taking advantage of symmetry we model only a unit cell of the laminate, consisting of a half

of the ITO stripe between two neighboring channel cracks and the substrate underneath (Figure 4.5b). In the simulation model, the film is a layer with thickness *h*, and the substrate is a block with thickness 1000*h* and length *s/2*. Symmetric boundary condition is set for the left edge of the unit cell and a horizontal displacement *u* is set along substrate portion of the right edge of the unit cell. The quantity $2u/s$ defines the applied strain.

Both the ITO film and the polymer substrate are modeled as linear elastic materials with Young's modulus of 140 GPa and 2GPa, respectively, and Poisson's ratio of 0.3 and 0.4, respectively. The linear elastic assumption is reasonable for the ITO film but has some limitations for the polymer substrate whose impact on modeling results will be discussed in detail later in the paper.

The channel cracks lead to stress concentration in the substrate near the channel roots, which could be severe enough to cause delamination along the ITO/polymer interface, as also evident in the *in situ* experiments. To simulate the cracking-induced interfacial delamination, the ITO/polymer interface is modeled as an array of nonlinear springs, which is characterized by a tensile and a shear traction-displacement law, with six parameters: interfacial tensile strength σ_n and shear strength σ_s, critical opening displacement δ_n and sliding displacement δ_s, and the areas under the traction-displacement curves Γ_n and Γ_s (i.e., the normal and shear adhesion energy of the ITO/polymer interface, respectively), as illustrated in Figure 4.5c. We assume that $\sigma_n = \sigma_s$, $\delta_n = \delta_s$ and $\Gamma_n = \Gamma_s$. In all simulations, $\sigma_n =$

500MPa and δ_n =0.5nm. The interfacial toughness Γ_n is varied to fit the crack density vs. applied strain curve from in situ experiments. The ITO/polymer interface is meshed with four-node cohesive elements sharing nodes with the neighboring elements in the film and the substrate. The viscous regularization option in finite element codes ABAQUS is used for the cohesive elements to enhance the computation convergence.

4.1.7. Modeling strategy and results

When a freestanding ITO thin film is subject to tension, it fractures by a *single* channel crack running through its width. Supported by a polymer substrate, the tensile fracture of the ITO thin film involves the initiation and propagation of *multiple* channel cracks, and the subsequent increase and saturation of the crack density as the applied tension increases, as observed in experiments. The increase of crack density is due to the transfer of tensile load from the polymer substrate to the ITO film through the interface. The brittle nature of the channel cracks in ITO thin film leads to severe stress concentration in the substrate near the channel roots that can cause delamination along the ITO/polymer interface. As the delamination initiates and propagates along the interface, the tensile load transferred from the polymer substrate to the ITO film decreases. If the delamination length is sufficiently large, the maximum tensile stress in the ITO film drops below the ITO fracture strength. As a result, no further channel cracks can be initiated in the ITO film. In other words, the crack density in the ITO film saturates.

Based on such an understanding, we apply the following modeling strategy in the simulations. For a given crack density vs. applied strain curve from *in situ* experiments (e.g., Figure 4.4), the crack density corresponding to the channel crack onset strain (e.g., 10/mm at 1.59% for 80 nm thick ITO film) defines a FEM simulation model with width of 50 μm (e.g., Fig. 4.5b). An ITO/polymer interfacial toughness (i.e., Γ_n) is assigned for the traction-displacement law of the interface. This unit cell model is stretched to the channel crack onset strain. The maximum tensile stress in the ITO, which occurs at the ITO portion of the left edge of the unit cell, is obtained. Given the brittle nature of the fracture of the ITO thin film, such a tensile stress indicates the ITO fracture strength, above which channel cracking occurs. A series of FEM unit cell models are then built with widths corresponding to the crack density values in the same experimental curve. Each simulation model is then stretched to a certain applied strain at which the maximum tensile stress in the ITO thin film reaches the ITO fracture strength determined from the first simulation model. The corresponding crack density vs. applied strain curve based on the above simulations is then plotted together with that from the *in situ* experiment for comparison. The value of Γ_n in the traction-displacement law of the ITO/polyimide interface is then varied, and the above simulation procedure is repeated until the best fit between the simulation and experiment curves is reached. The corresponding value of Γ_n and maximum tensile stress in the ITO thin film are defined as the ITO/polyimide interfacial toughness and the ITO fracture strength, respectively.

Figure 4.6 plots the crack density vs. applied strain curves from the best-fit simulations and experiments, for ITO film thickness of 80 nm and 200nm, respectively. The ITO/polyimide interfacial toughness and the ITO fracture strength obtained from the best fit simulations are 9.5J/m^2 and 2.4GPa for 80 nm thick ITO film, and 10.8J/m^2 and 1.7GPa for 200 nm thick ITO film, respectively. As shown in Figure 4.6, the simulation curves can fit the experiment curves quite well until a certain applied strain. When the applied strain further increases, the maximum tensile stress in the ITO film cannot reach the ITO fracture strength, therefore no further channel crack can be initiated. In this sense, the simulation model underestimates the saturated crack density. Such a discrepancy in saturated crack density between the modeling and the experiment results can be attributed to the assumption of elastic behavior of the polymer substrate. In reality, the polymer substrate yields and deforms plastically if the applied tensile strain exceeds a critical value. The linear elastic assumption for the polymer leads to an overestimated tensile stress in the substrate. As a result, under a given applied tension, the length of the delamination along the ITO/polymer interface is also overestimated due to the increased stress concentration at the delaminating front. Consequently, the tensile stress transferred to the ITO thin film is underestimated, leading to a prediction of saturated crack density lower than that measured in the *in situ* experiments. Nonetheless, those predicted values from the simulations offer estimates of the lower bounds of the ITO/polyimide interfacial toughness and ITO fracture strength, which agree with the results from other recent experiments.

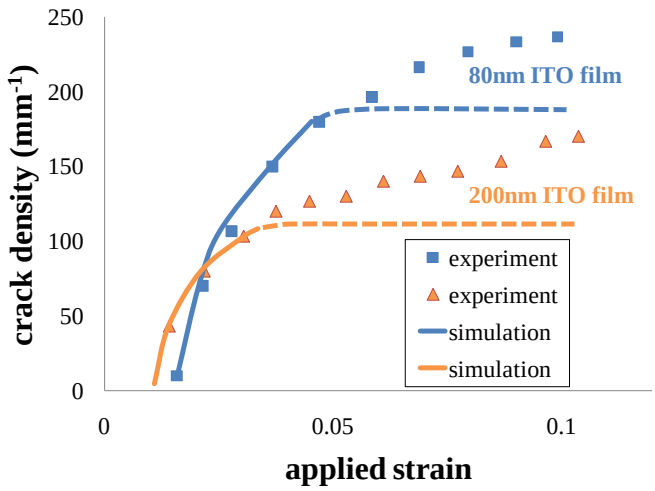

Figure 4.6 The crack density vs. applied strain curves from the best-fit simulations and experiments, for ITO film thickness of 80 nm and 200nm, respectively.

Figure 4.7a plots the variation of the tensile stress in the 80 nm thick ITO thin film as a function of the relative location in a unit cell model, at various applied strains. When the applied strain is small, the distribution of the tensile stress is rather uniform in majority part of the ITO thin film except the portion near the channel crack. As the applied strain increases, interfacial delamination initiates and propagates. As a result, the tensile stress transferred to the ITO thin film is reduced, leading to a rather non-uniform distribution of the tensile stress in the ITO thin film, with the highest level at the center of the ITO fragment and gradually diminishing to zero in the delaminated portion. Figure 4.7b further plots the delamination length normalized by the ITO fragment width as a function of applied strain, for both 80 nm and 200 nm thick ITO films, respectively, which clearly shows the advance of

interfacial delamination, and therefore the underlying mechanism for the saturation of crack density in polymer-supported ITO thin films under tension.

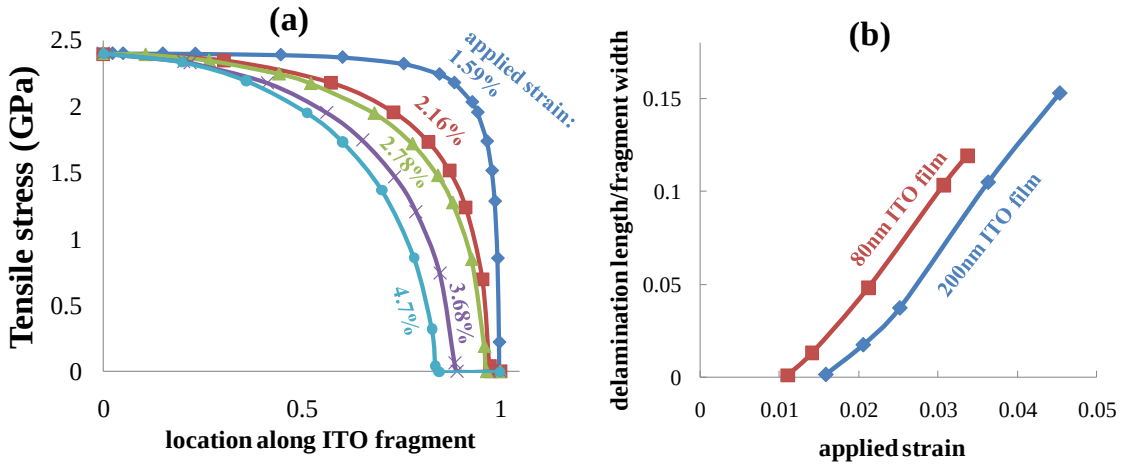

Figure 4.7 (a) The variation of the tensile stress in the 80 nm thick ITO thin film as a function of the relative location in a unit cell model, at various applied strains. For the horizontal axis, 0 denotes the center of the ITO fragment and 1 denotes the right edge of the ITO fragment (i.e., the channel crack surface). (b) The delamination length normalized by the ITO fragment width as a function of applied strain, for both 80 nm and 200 nm thick ITO thin films, respectively.

Given the brittle nature of the ITO thin film fracture, the cohesive toughness of the ITO thin film is defined as the energy required for propagating channel crack to generate new crack surface of unit area. The detailed shape and deformation state near the channel crack front can be rather complicated, and hard to predict. By contrast, far ahead and far behind the channel crack front, the structure can be taken to deform under the plane strain conditions. Since both ITO and polymer are assumed to be linearly elastic at the channel crack onset strain, the driving force for the channel cracking can be calculated by the elastic energy stored in a slice of

ITO/polymer laminate of unit thickness far ahead of the channel crack front minus the elastic energy stored in a slice of ITO/polymer laminate of unit thickness far behind the channel crack front. In the simulation, the widths of these two slices of ITO/polymer laminate are set to be the reciprocal of the crack density corresponding to the crack onset strain in the *in situ* experiment. The slice far ahead of the channel crack front has a continuous ITO thin film, while the slice far behind has a channel crack in the middle of the ITO thin film. Each slice is subject to an applied strain equal to the crack onset strain, and the resulting strain energy is calculated in ABAQUS. Applying the above simulation strategy to the experiment results, we obtain a cohesive toughness of 42.0J/m^2 for ITO films with thickness of 80nm and 40.4J/m^2 for ITO films with thickness of 200nm. These values roughly agree with the results from other recent studies.[120]

The thickness dependence of the saturated crack density in polymer supported brittle films has been observed in previous studies.[127] A few mechanics models have been considered to explain such thickness dependence.[128] A consideration of the force balance of an ITO fragment at the saturation limit gives $\tau = 2h_{ITO}\sigma / s_{cr}$, where τ is the interfacial shear stress, h_{ITO} is the ITO film thickness, σ is the tensile stress in ITO film and s_{cr} is a length close to the ITO fragment width at the saturation limit (i.e., $1/s_{cr}$ approximately denotes the saturated crack density). A fracture mechanics based dimensional consideration leads to $\sigma \propto \sqrt{\Gamma_{ITO}/h_{ITO}}$, where Γ_{ITO} is the cohesive toughness of the ITO film. Given that the same fabrication conditions in depositing ITO films of different thickness on the same polymer substrate, it is

reasonable to assume similar interfacial properties in different samples (e.g., as evident by the similar interfacial toughness values predicted above). In other words, the interfacial shear stress τ remains to be constant. The above analysis yields that the thickness dependence of the saturated crack density takes the form of $\sqrt{\Gamma_{ITO} h_{ITO}} / s_{cr} \approx$ constant. Using the ITO cohesive toughness obtained before and the saturated crack density data from *in situ* experiments, the value of $\sqrt{\Gamma_{ITO} h_{ITO}} / s_{cr}$ for h_{ITO} =80 nm agrees with that for 200nm within about 10%. This good agreement confirms the above mechanics understanding of the thickness dependence of the saturated crack density in polyimide supported ITO thin films.

4.1.8. Bending fatigue experiment and results

Other than the monotonic loading, flexible electronic devices will be under the cyclic deformation in most of the time. They will be bent, twisted and stretched repeatedly. While organic substrates can recover from large strains, the inorganic ITO layer might fracture at small strains, often less than about one percent. Recent experiment [122] showed the gradual damage of thin ITO films on polymer substrate under cyclic tensile loading. This observation is both intriguing and puzzling, because a brittle material like ITO is not particularly susceptible to fatigue under cyclic loads.

There is no a standard way to quantify the electro-mechanical properties under cyclic loading, and people have developed different testing machines based on the sample dimensions and materials properties [13, 16, 122, 129]. Bending test is one of the prevalent methods and adopted by many researchers. In our work, we used

the cyclic fatigue tester machine mentioned in Chapter 2 to run the bending fatigue test for ITO-based electrodes, and the schematics and image are showed in Figure 4.8. The dog-bone shape sample (7 mm in length and 3 mm in width) will be fixed in one end, and the compression load will be applied from the other end. By controlling the compression distance ∆D showed in the Figure 4.8, the level of bending can be controlled. Generally speaking, larger value of ∆D results in high strain of bending.

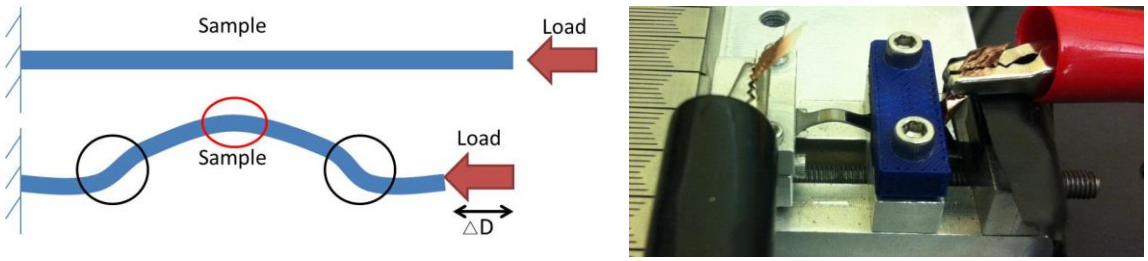

Figure 4.8 Schematics and image of bending fatigue testing method. By controlling the compression distance ∆D, the level of bending can be controlled.

The results of bending fatigue are showed in Figure 4.9 a. The resistance would increase dramatically after the first few cycles then saturate at certain range. The saturated value depends on the bending level (or higher travelling distance ∆D). The higher travelling distance always results in larger saturated value. The parallel channel cracks were found near the contact portions for clamping samples (black circles in Figure 4.8), not in the middle of the sample (red circle in Figure 4.8). The most severe damage happen in the two ends of sample, other than in the center.

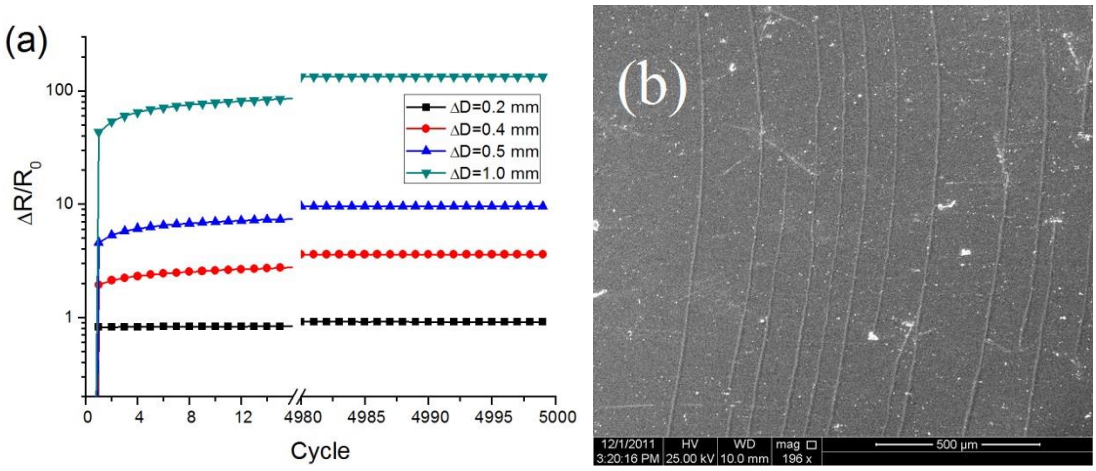

Figure 4.9 (a) The resistance as the function of bending cycles. (b) The SEM image shows that cracks happened in the bending portion (black circles in Figure 4.8) of the sample.

4.2. Enhanced electro-mechanical properties on multi-layer ITO electrodes

4.2.1. Introduction of multi-layer barrier and electrode

The multilayer structural design of ITO-based electrodes in the present study is inspired by the recent progress in designing high performance permeation barriers for flexible electronics. While flexible electronics is being developed toward an array of promising applications (e.g., paper like displays and sensitive electronic skins, etc),[7, 130-134] the service life of flexible devices is limited due to the vulnerability of functional organic layers in flexible devices to the attack of environmental water vapor and oxygen. High performance permeation barriers are desired to achieve long-lasting flexible electronics devices. However, designing such permeation barriers to allow a reasonable service life of flexible devices is rather challenging,

given the design criteria over three orders of magnitude more stringent than that of traditional barriers in terms of water vapor permeation rate and the large deformation of the flexible devices.[135, 136] Recently, organic-inorganic multilayer permeation barriers (e.g., alternating layers of polyacrylate and Al_2O_3) are emerging as a promising solution to the stringent barrier requirement of flexible electronics.[135, 137, 138] In such multilayer permeation barriers, the inorganic layer serves as the barrier for water vapor and oxygen and the organic layers decouple the defects (e.g., pinholes) in the as-made inorganic layers and thus yield a remarkably elongated diffusion path for water and oxygen molecules. Modeling study of the failure mechanics of multilayer permeation barriers shows that the organic layers can also increase the critical fracture strain of the inorganic layers.[126, 139] A recent study further reveals that a compliant protective coating on the top inorganic layer in a multilayer permeation barrier can further enhance the mechanical durability of the permeation barriers.[126]

Motivated by the progress in the abovementioned multilayer permeation barriers, we design and fabricate ITO-based multilayer electrodes with enhanced electro-mechanical durability. The failure mechanics of the ITO-based multilayer electrodes will be investigated through both in situ electro-mechanical experiments of the electrodes and coherently devised mechanics modeling. So far, existing studies on inorganic/organic multilayer permeation barriers for flexible electronics are mainly based on modeling and no systematic experimental study of their failure mechanics has been reported. In this sense, results from the present paper could also

potentially lead to a better understanding of the failure mechanisms of multilayer permeation barriers.

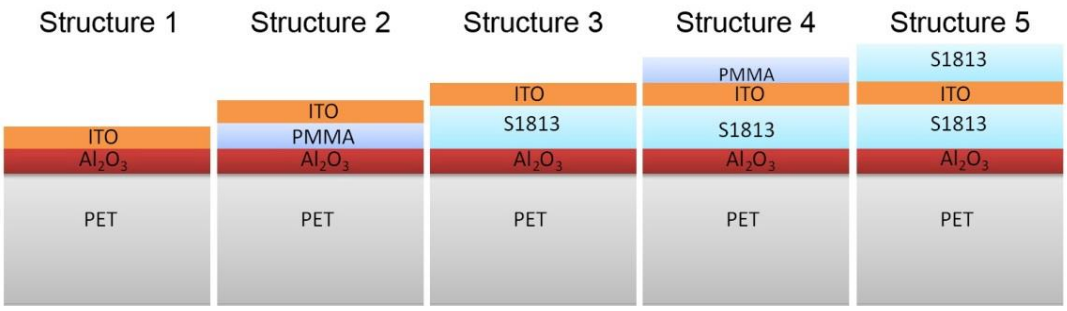

Figure 4.10 Schematics of five structural designs of ITO-based multilayer electrodes. The thicknesses of PET, Al_2O_3, ITO, PMMA, and S1813 are 127 µm, 60 nm, 80 nm, 100 nm and 1 µm, respectively. A 5 nm Cr layer is coated between adjacent layers to increase interlayer adhesion (not shown for visual clarity).

4.2.2. Design and fabrication of five different structures of ITO-based multilayer electrodes

Five different structures of ITO-based multilayer electrodes are designed and fabricated, and schematics of the cross-section view of these five structures are showed in Figure 4.10. The polyethylene terephthalate (PET, 127 µm thick) in well-cut dog-bone shape (gauge length and width are 7 mm and 3 mm, respectively) is employed as the substrate. The PET substrate is first coated by an Al_2O_3 (60 nm thick) layer using e-beam evaporation method (Sharon E-Beam Evaporator). In Structure 1, an ITO layer (80 nm thick) is further coated directly on top of the Al_2O_3 layer, using e-beam evaporation method. In Structure 2, an intermediate polymeric layer of polymethyl methacrylate (PMMA, 495A2 from MicroChem Corp.) is first

coated onto the surface of the Al_2O_3 layer by spin coating method with the speed of 1000 rms for 30 seconds, and the resulting thickness of PMMA is about 100 nm. An ITO layer (80 nm thick) is then coated on top of the PMMA layer. In Structure 3, S1813 (Shipley Microposit S1813 photoresist) is used as intermediate polymeric layer between the Al_2O_3 and ITO layers and is spin coated with the speed of 3000 rms for 30 seconds with a resulting thickness about 1 μm. In Structures 4 and 5, a layer of PMMA (100 nm thick) and S1813 (1 μm thick) is spin coated on top of the ITO layer of Structure 3, respectively, serving as a top protective coating. The thicknesses of various layers in these five structure designs are determined by an atomic force microscope (Digital Instrument Nanoscope IIIA), using the contact mode. To ensure the well bonding in between layers in all five designs, a 5 nm thick Cr layer (not shown in Figure 1 for visual clarity) is coated between adjacent layers by e-beam evaporation method.

4.2.3. *In situ* SEM observation of channel cracks in ITO film under uni-axial tension

To characterize the channel cracks initiation and propagation of the ITO layers in different multilayer electrode structures, *in situ* uni-axial tensile tests are performed inside a SEM chamber. The in situ tensile tests are of particular importance to correlate crack initiation and propagation process with the applied tensile strain, and to avoid the unloading-induced partial or full closure of cracks in the ITO layer in ex situ tests. The detail description of the experimental method can be found in our earlier paper.[54]

The channel crack initiation and propagation process in the ITO layer in Structures 1, 2 and 3 are quite similar: ITO layers are very smooth, without any appreciable cracks before loading; as the tensile strain increases to a threshold value, small channel cracks start to initiate at the edges of sample and then grow along the sample width direction, perpendicular to the tensile loading direction. Figure 4.11 shows a series of snapshots of these multilayer electrodes during tensile loading. Some interesting phenomena are found as following. First, the channel crack distribution in the ITO film is quite uniform along the sample length direction (also the loading direction), which suggests that the rather uniform elongation of the PET substrate. Second, as the strain level increases, the number of channel cracks in the same structure would increase, e.g., the number is only 4 in Figure 4.11b but 8 in Figure 4.6e. Finally, at the same strain level, the number of cracks is affected by the existence and thickness of the intermediate polymer layer: the number of cracks can be reduced after inserting a thin polymer layer in Structure 2, compared to Structure 1(Figure 4.11a and b, and Figure 4.11d and e), even the thickness of the polymer is on the same order of Al_2O_3 barrier and ITO function layer (100 nm PMMA, 60 nm Al_2O_3 and 80 nm ITO); and the number of cracks can be further reduced if the polymer thickness is increased in Structure 3 (1 μm S1813), compared to Structure 2 (Figure 4.11b and c, and Figure 4.11e and f). It is worth noting that, when Structure 1 is subject to severe tension, some ITO strips (demarcated by two neighboring channel cracks) delaminate and buckle away from the substrate (e.g., Figure 4.11d), driven by the compressive stress in the ITO film due to the Poisson's effect. Severe bending due to buckling results in high tensile

stress near the top surface of the buckled crest of the ITO strip, which eventually leads to the ITO cracking at the crest along the direction roughly parallel to the applied tension.[140]

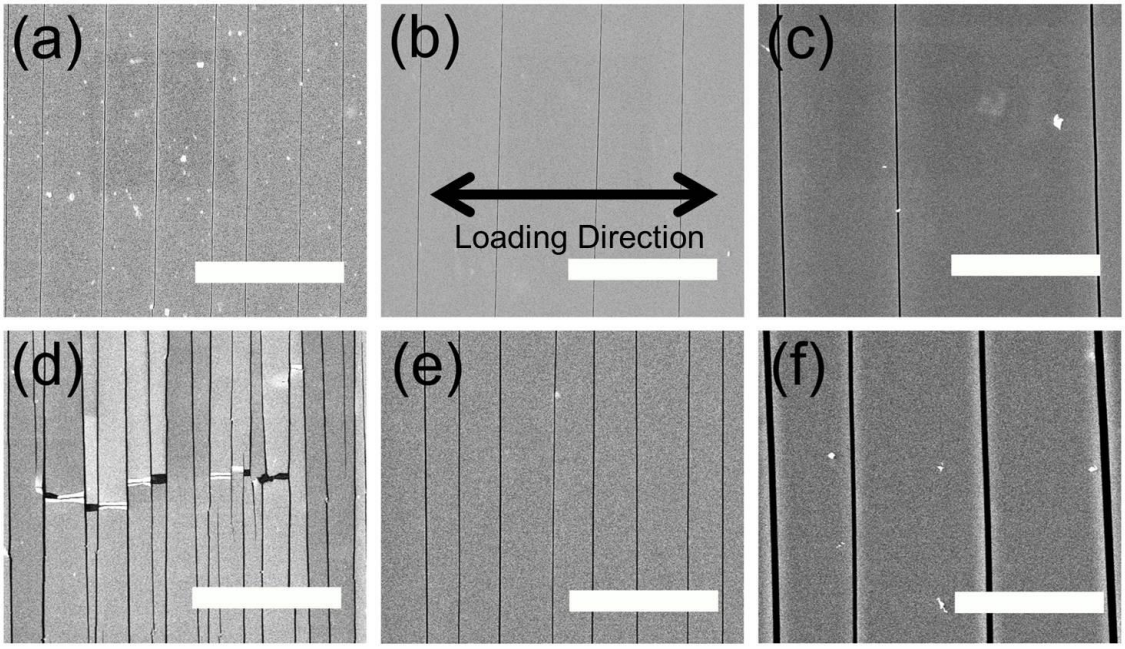

Figure 4.11 *In situ* observation of multilayer structures in different strain levels: (a) Structure 1, (b) Structure 2, and (c) Structure 3 are at the strain of ~4%; and (d) Structure 1, (e) Structure 2 and (f) Structure 3 are at the strain of ~13%. The white scale bar in each figure is 30 μm in length.

To quantitatively describe the channel cracking under applied tensile strain, we define crack density as the number of channel cracks per unit length in the tensile loading direction. The crack density as a function of the applied tensile strain in Structures 1 to 3 is shown in Figure 4.12a. For each structure, the crack density first increases significantly as the applied strain increases, and then gradually saturates at certain value. The sample without any intermediate polymeric layer (Structure 1)

has the highest value of saturating crack density, while the sample with the thicker S1813 intermediate polymeric layer has the lowest value of saturating crack density (Structure 3). Both qualitative observation and quantitative results of the evolution of crack density at various applied strains indicate that the intermediate PMMA layer in Structure 2 can effectively reduce the crack density when compared with that in Structure 1, and the crack density can be further reduced when a thicker and stiffer intermediate polymeric layer is used (Structure 3).

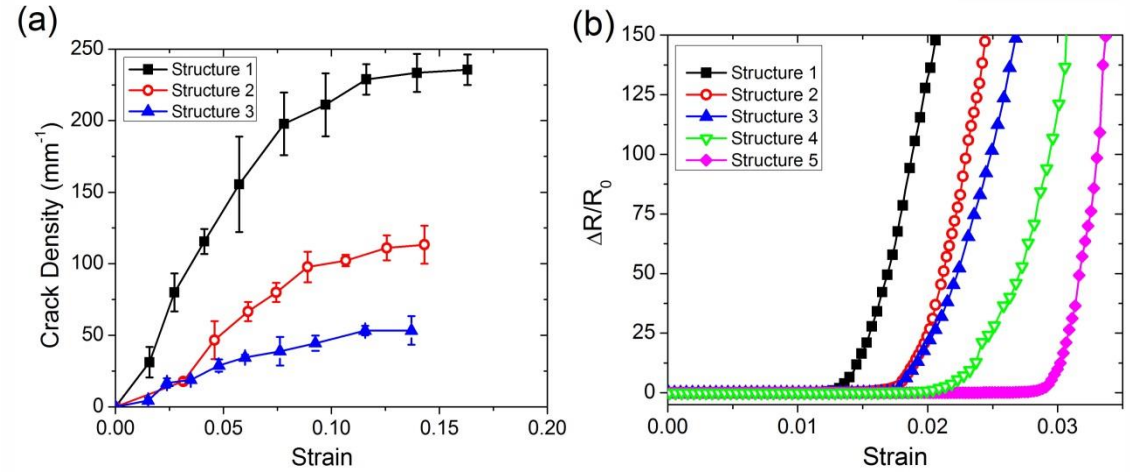

Figure 4.12 (a) Cracks density and (b) normalized change in electrical resistance as the function of strain in different ITO-based multilayer electrodes.

4.2.4. Electro-mechanical behavior of ITO-based multilayer electrodes

In real applications of flexible electronics, the strain level should be less than that for the initiation of channel cracks in functional layers, and that strain level is always less than 3% in ITO-based electrodes.[140] Other than mechanical failure, conductive failure, defined as the dramatic increase in electrical resistance during

deformation, is also employed to evaluate the electro-mechanical quality of electrodes in a more direct and effective way. Figure 4.12b plots the normalized change in electrical resistance as a function of the applied tensile strain. For each multilayer electrode, the electrical resistance of the ITO thin film remains nearly unchanged when the applied tensile strain is relatively small. In other words, the ITO thin film remains electrically conductive when subject to a modest elongation. As the applied tensile strain further increases, the electrical resistance first rises gradually, and then shoots up dramatically, leading to the conductive failure. The critical strain of an ITO-based multilayer electrode is defined as the strain when the normalized change in electrical resistance starts to shoot up dramatically, and the value ranges of critical strain for all the electrodes are listed in Table 4.1. It is found that the value of critical strain in Structure 1 is the smallest. More importantly, the critical strain is affected by the existence of the intermediate layer: the value of critical strain is increased after inserting the intermediate polymeric layer (PMMA or S1813) in Structure 2 or 3. However, not like the crack density, the thickness of the intermediate polymeric layer seems to play little role in the critical strain: there is nearly no difference of critical strains between Structure 2 and 3.

The above results clearly show that the intermediate polymeric layer can reduce the density of channel cracks in high strain level (>4%) and increase the electrical stability in low strain level (<3%). It has been previously shown that the mechanical durability of the top oxide layer in a multilayer structure can be enhanced by applying a thin protective coating onto the surface of the top oxide.[126] In this work, we coat a polymeric layer (thin PMMA or thick S1813) on top of the ITO thin

film (Structures 4 and 5), aiming to increase the electro-mechanical properties during the tensile loading. The results in Figure 4.12b clearly show that the critical strain has been increased after the protective coating, and this is a clear evidence for the improvement of electro-mechanical quality in multilayer structures. In particular, the critical strain of Structure 5 is even higher than that of Structure 4, indicating that a thicker polymeric layer offers more mechanical constraint, which leads to a reduced driving force for the channel cracking of ITO layer.

Table 4. 1 **Critical strains of ITO-based multilayer electrodes. The value range of critical strain in each structure was determined from at least three electro-mechanical tests.**

Structure number	**1**	**2**	**3**	**4**	**5**
Critical strain (%)	1.0-1.3	1.7-1.9	1.7-1.9	2.1-2.3	2.5-2.8

4.2.5. Discussion: Dominating failure modes of ITO-based multilayer electrodes

To understand the dependence of the critical strains of ITO electrodes (as in Table 4.1 and Figure 4.12b) on the multilayer structural design, we next establish a mechanics model to compute the driving force for steady state channel/tunnel cracking of the ITO electrodes in Structures 1 to 5. Results from our mechanics modeling offer a mechanistic understanding of the role of intermediate and top protective polymeric layers on the improvement of electro-mechanical durability of ITO electrodes.

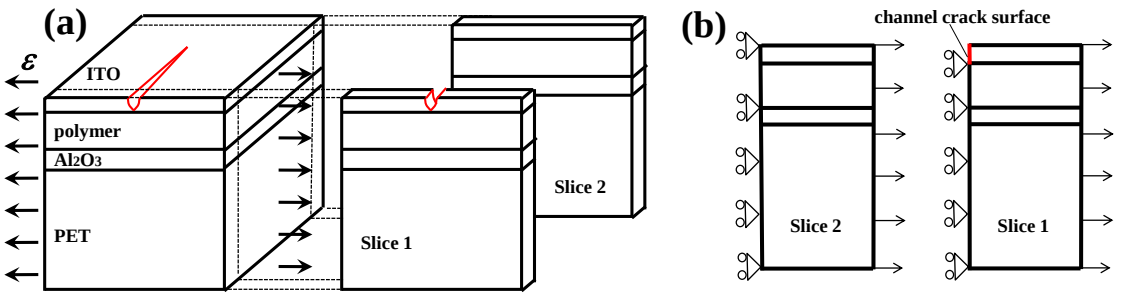

Figure 4.13 (a) The elastic energy reduction associated with the steady state channel cracking propagation in the multilayer can be computed by subtracting the elastic energy stored in a slice of the multilayer structure of unit thickness far behind the crack front (Slice 1) from that far ahead of the crack front (Slice 2). (b) Schematics of models of Slice 1 and Slice 2 used in finite element simulations.

It has been shown that,[139] for a multilayer structure such as Structures 2 to 5 under tension, if the intermediate polymeric layer is thicker than the ITO layer, channel cracking of the top ITO layer in Structures 2 and 3 (or tunnel cracking of the ITO layer in Structures 4 and 5) requires the least driving force when compared with other tensile-cracking failure modes, such as tunnel cracking of the intermediate polymeric layer or channel cracking of ITO/polymer/Al_2O_3 as a whole. In our multilayer design of Structures 2 to 5, both PMMA and S1813 layers are thicker than the ITO layer. Therefore, channel/tunnel cracking of the ITO layers is expected to be the dominating failure mode in Structures 2 to 5, which agrees with our experimental observation.

For Structure 1, however, the ITO layer directly lies on the Al_2O_3 layer without any intermediate polymeric layer in between. Under tension, there may exist two possible failure modes of Structure 1. In failure mode (a), channel cracks occur only in the top ITO layer while the Al_2O_3 layer remains intact, while in failure mode (b), channel cracks cut through the whole thickness of both ITO and Al_2O_3 layers. To determine dominating failure mode of Structure 1, we next compute the critical fracture strains corresponding to the above two failure modes, the lower of which determines the dominating failure mode.

Taking all materials in the multilayer structure to be linearly elastic, the steady state channel cracking propagation is driven by the associated reduction of elastic energy in the multilayer due to crack opening. This elastic energy reduction can be computed by subtracting the elastic energy stored in a slice of the multilayer structure of unit thickness far behind the crack front (Slice 1) from that far ahead of the crack front (Slice 2), as illustrated in Figure 4.13a. When the thickness of the intermediate polymeric layer in Figure 4.13a vanishes, it corresponds to Structure 1. Assuming a uniform spacing *s* between neighboring channel cracks (i.e., $1/s$ is the crack density), dimensional analysis leads to the following form of the elastic energy reduction in Structure 1

$$U = E'_{ITO}\varepsilon^2 h_{ITO}^2 f\left(\frac{h_{ITO}}{h_{Al_2O_3}}, \frac{E_{ITO}}{E_{Al_2O_3}}, \frac{h_{ITO}}{s}\right) \qquad \textbf{Equation 4.}\ 1$$

where $E'_{ITO} = E_{ITO}/\left(1-\nu^2_{ITO}\right)$ is the plane strain Young's Modulus of ITO, ε is the applied tensile strain. h_{ITO} ($h_{Al_2O_3}$) and E_{ITO} ($E_{Al_2O_3}$) are the thickness and Young's Modulus of ITO (Al_2O_3), respectively, and ν_{ITO} is the Poisson's ratio of ITO. The dimensionless function f denotes the normalized energy released rate of ITO film cracking and can be calculated numerically using finite element method. For clarity, the dimensionless functions f for failure modes (a) and (b) are designated as f_a and f_b, respectively. For failure mode (a), channel cracks will propagate in the ITO layer if the associated reduction of elastic energy U_a exceeds the fracture toughness of ITO, Γ_{ITO}, times the thickness of the ITO layer. Therefore the critical condition can be given as

$$U_a = \Gamma_{ITO} h_{ITO} \qquad \textbf{Equation 4. 2}$$

A combination of Eqs. 4.1 and 4.2 give the normalized critical applied strain ε_a for crack propagation in the ITO layer

$$\frac{\varepsilon_a}{\sqrt{\Gamma_{ITO}/E'_{ITO}h_{ITO}}} = \sqrt{\frac{1}{f_a}} \qquad \textbf{Equation 4. 3}$$

For failure mode (b), cracks channel through the whole thickness of ITO and Al_2O_3 layers, therefore, the associated reduction of elastic energy is

$$U_b = \Gamma_{ITO} h_{ITO} + \Gamma_{Al_2O_3} h_{Al_2O_3} \qquad \textbf{Equation 4. 4}$$

where $\Gamma_{Al_2O_3}$ is the fracture toughness of Al_2O_3. A combination of Eqs. 4.1 and 4.4 gives the critical strain ε_b for channel cracking propagation in both ITO and Al_2O_3

$$\frac{\varepsilon_b}{\sqrt{\left(\Gamma_{ITO} h_{ITO} + \Gamma_{Al_2O_3} h_{Al_2O_3}\right) / E'_{ITO} h_{ITO}^2}} = \sqrt{\frac{1}{f_a}} \qquad \textbf{Equation 4. 5}$$

In our specimens, $h_{Al_2O_3} = 0.75 h_{ITO}$. For simplicity, the fracture toughnesses of ITO and Al_2O_3 are taken to be identical, i.e., $\Gamma_{ITO} = \Gamma_{Al_2O_3}$. Equation 4.5 can then be reorganized as

$$\frac{\varepsilon_b}{\sqrt{\Gamma_{ITO} / E'_{ITO} h_{ITO}}} = \sqrt{\frac{1.75}{f_b}} \qquad \textbf{Equation 4. 6}$$

Dimensionless functions f_a and f_b are calculated by normalizing the elastic energy reduction U associated with channel crack propagation. As aforementioned, this elastic energy reduction can be computed by subtracting the elastic energy stored in a slice of the multilayer structure of unit thickness far behind the crack front (Slice 1) from that far ahead of the crack front (Slice 2), as illustrated in Figure 4.13a. The elastic energy stored in Slice 1 and Slice 2 can be directly calculated using finite element code ABAQUS. Schematics of models used in finite element calculation for Slices 1 and 2 are given in Figure 4.13b. The width s of the model is defined by the inverse of crack density. Taking advantage of symmetry, only half of the slice is modeled and symmetric boundary condition is set for the left edge of the model (in

Slice 1, the ITO portion of the left edge is set free to simulate the free channel crack surface); a horizontal displacement $u/2$ is set along the right edge of the model. Therefore, the quantity u/s defines the applied strain. In the finite element calculations, the Young's moduli of ITO, Al_2O_3 and PET are set to be 200 GPa, 300 GPa and 2 GPa, respectively, and their Poisson's ratios are 0.3, 0.3 and 0.4, respectively. The thickness of the PET substrate is set to be $625h_{ITO}$. The whole model is meshed with the second-order eight-node quadrilateral elements, with densified mesh in the region near the crack tip. The elastic energy stored in Slice 1 and Slice 2 can be readily calculated.

Table 4.2 lists the calculated normalized critical strains for failure modes (a) and (b) for three different crack densities. For all crack densities considered, the critical strains for failure mode (b) is always lower than those for failure mode (a). In other words, for Structure 1, the dominating failure mode is the channel cracking through the whole thickness of ITO and Al_2O_3 layers. This can be understood as follows. For failure mode (a), the opening of the channel cracks in the top ITO layer is constrained by the underlying Al_2O_3 layer. For failure mode (b), the opening of the channel cracks cutting through both ITO and Al_2O_3 layers is subject to the constraint of the underlying PET substrate. Given the huge difference in the Young's moduli of Al_2O_3 and PET, the mechanical constraint of the Al_2O_3 layer in failure mode (a) is much stronger than that of the PET substrate in failure mode (b). Consequently, under tension, Structure 1 is vulnerable to channel cracking through the whole thickness of ITO and Al_2O_3 layers.

Table 4. 2 Normalized critical strains for failure modes (a): channel cracking in the top ITO layer and failure mode (b): channel cracking in both ITO and Al2O3 layers for various crack densities.

	Crack density =10 mm^{-1}	30 mm^{-1}	100 mm^{-1}
$\frac{\varepsilon_a}{\sqrt{\Gamma_{ITO}/E'_{ITO}h_{ITO}}}$	0.518	0.528	0.532
$\frac{\varepsilon_b}{\sqrt{\Gamma_{ITO}/E'_{ITO}h_{ITO}}}$	0.197	0.208	0.226

4.2.6. Discussion: Comparing driving forces for crack propagation in Structures 1 to 5

We next compute the driving forces for the steady state channel/tunnel cracking in Structures 1 to 5. The comparison of such driving forces provides mechanistic understanding of the dependence of the measured critical strains of ITO electrodes on the multilayer structural design. The driving forces of cracking for Structures 1 to 5 are defined as

$$G_i = \frac{U_i}{h_i} = \frac{E'_{ITO}\varepsilon_{appl}^2 h_{ITO}^2 f_i}{h_i} \quad i = 1,\ldots,5 \qquad \textbf{Equation 4. 7}$$

where U_i is the associated reduction of elastic energy due to crack propagation in Structure i as defined in Eq. 4.1, h_i is the total thickness of the cracked layers ($h_i = 1.75h_{ITO}$ for Structure 1 and $h_i = h_{ITO}$ for Structures 2 to 5). The values of the dimensionless function f_i are computed using finite element method, with similar strategy delineated before. Here, PMMA and S1813 are modeled as linear elastic materials with Young's modulus of 2 GPa and 7 GPa, respectively, and Poisson's ratio of 0.4 for both.

Figure 4.14 plots normalized driving force for cracking propagation $G_i / E'_{ITO}\varepsilon_{appl}^2 h_{ITO}$ in Structures 1 to 5 as a function of crack density. In the range of crack density we study (i.e., 10 mm^{-1}~100 mm^{-1}), $G_1 > G_2 > G_3 > G_4 > G_5$. In other words, for a given fracture toughness of the ITO layer, Structure 1 has the lowest critical strain to lose electronic conductance of the ITO electrode while Structure 5 has the highest critical strain. Such a prediction of the dependence of critical strain on the structural design agrees with the experimental measurements as shown in Table 4.1 and Figure 4.12b. Such dependence can be further understood as follows. In Structures 2 and 3, the deformable intermediate polymeric layer prevents the channel cracks in the ITO layer from penetrating into the Al_2O_3 layer. In turn, the intact stiff Al_2O_3 can offer relatively strong mechanical constraint to the ITO cracking. By contrast, the Al_2O_3 layer in Structure 1 fractures with the ITO layer. As a result, there is a more than two-fold decrease of crack driving force in Structures 2 and 3 from that in Structure 1, for a given crack density. Since the S1813 intermediate layer in Structure 3 is stiffer and thicker than the PMMA intermediate

layer in Structure 2, the overall mechanical constraint on the ITO cracking in Structure 3 is slightly stronger than that in Structure 2. Therefore, $G_2 > G_3$. For Structures 4 and 5, the top protective polymeric layer further constrains the cracking opening displacement of the ITO layer (turning channel cracking into tunnel cracking), which results in an about four-fold decrease of the crack driving force from Structures 2 and 3, for a given crack density. When compared with Structure 1, the overall reduction of the crack driving force in Structure 5 is more than ten-fold. In other words, a thin, compliant and well-bonded top protective layer and an intermediate polymeric layer can effectively enhance the electro-mechanical durability of the ITO-based multilayer electrodes. The above results agree with those in a recent study of the mechanical durability of inorganic/organic multilayer permeation barriers for flexible electronics. The slight decrease of the crack driving force as the increase of crack density as shown in Figure 4.14 can be explained by the partial mitigation of the stress level in the uncracked portions of the ITO layer due to channel/tunnel crack propagation. More crack propagation (i.e., higher crack density) leads to further reduction of the effective stress level in the ITO layer, and thus the slight decrease of the crack driving force. Experimental results in Table 1 show that the critical failure strains of Structure 5 are higher than those of Structure 4, while the modeling results in Figure 5 show that the driving force for cracking in Structures 5 is only slightly lower than that of Structure 4. For Structures 2 and 3, the experimental results on critical failure strains are nearly identical, but the modeling results in Figure 4.14 predict a 10~20% difference in their driving forces for cracking. These discrepancies between the experimental and modeling results

may be attributed to the assumption of well-bonded interfaces in the multilayer electrodes in our models. In reality, interfacial delamination may occur between the ITO layer and the polymeric layers, which leads to an increased driving force for cracking of the ITO layer.[126]

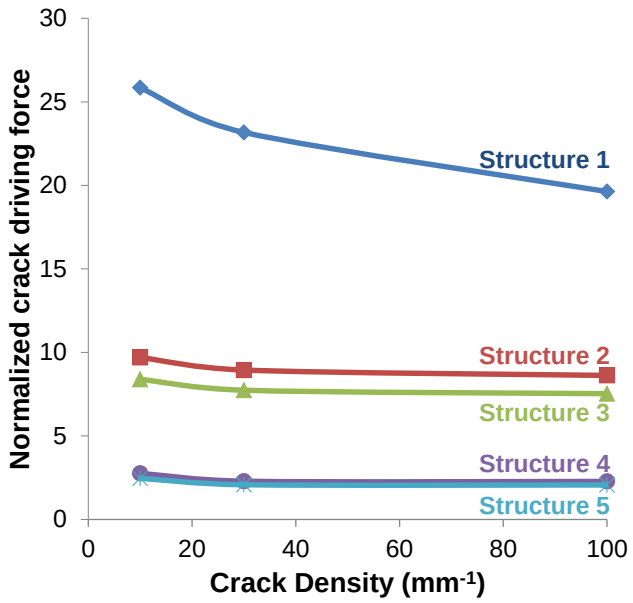

Figure 4.14 Normalized driving force for cracking propagation $G_i / E'_{ITO}\varepsilon^2_{appl}h_{ITO}$ in Structures 1 to 5 as a function of crack density.

4.3. *In situ* electro-mechanical characterization of fracture behavior in CNT film

In this session, we performed *in situ* electro-mechanical tests of single-wall carbon nanotube (SWCNT) and multi-wall carbon nanotube (MWCNT) thin films deposited

on polyethylene terephthalate (PET) substrates inside a scanning electron microscope (SEM). Both monotonic loading of large deformation and cyclic loading of small deformation were applied to the samples, and then the crack initiation and propagation, crack density evolution and the corresponding electrical resistance variation were systematically investigated.

4.3.1. Sample preparation and experimental procedures

We used commercially available SWCNT/PET films from TOP NANOSYS, and MWCNTs synthesized by chemical vapor deposition method from Hanwha nanotech. It was informed that SWCNT was synthesized by arc-discharge method. SWCNT/PET and MWCNTs were verified by field emission scanning electron microscopy (FE-SEM) before coating. Thermogravimetric analysis showed that there were limited impurities in MWCNTs. We dispersed MWCNTs in deionized water with 0.4 wt % sodium dodecyl sulfate (SDS) and sonicated for several hours. The concentration of MWCNT was 0.1 mg/mL. We then sprayed the MWCNT solution on a PET substrate to fabricate the flexible electrode. The SWCNT/PET film was fabricated in TOP NANOSYS using a similar process with MWCNT/PET film. The thicknesses of PET substrate and CNT film are 188 μm and 75±25 nm, respectively.

The resulting SWCNT/PET and MWCNT/PET films were cut into rectangle strip samples for in situ tests, with gauge length ~10 mm and width ~ 2 mm. For SWCNT/PET films, the R_0 and initial sheet resistance are ~6300 Ω and ~1200 Ω/□;

for MWCNT/PET films, the R_0 and initial sheet resistance are ~10000 Ω and ~1900 Ω/□. The in situ tensile tests were performed using a microtester (Deben UK, Ltd.) inside a SEM chamber (FEI Quanta 400 high resolution field emission scanning electron microscope, FEI company, Hillsboro, OR). The uni-axial tensile tests were conducted under displacement control, and the strain rate was controlled to be around 10^{-3}/s. The increase of applied tensile strain was paused at certain preset strain values to allow for high resolution SEM imaging at different locations along the sample length. The electrical resistance of the samples was measured by two point probe method using a Keithley 2000 multimeter during the tensile test.

4.3.2. *In situ* SEM observation of crack initiation and propagation in SWCNT/PET electrodes

The evolution of crack initiation and propagation in SWCNT/PET strip samples was shown in Figure 4.15 a-c. At the beginning stage, the surface was very flat, and there was no visible micro-scale crack at the strain level lower than 30%. After the strain reached a critical value (strain=42.8% in Figure 4.15a), short and narrow cracks appeared on the surface. The cracks' growth directions were always perpendicular to the loading direction. Their average length was around 1.5 μm, and the average width was around 200 nm. The density and width of cracks increased as the increasing applied strain. Compared to Figure 4.15a with a strain=42.8%, larger number of cracks, whose average width was around 300 nm, can be found in the Figure 4.15b with a strain=61.5%. However, the average length of cracks kept at around 1.5 μm and did not increase too much after their appearance. The depth of

the cracks also increased as the increasing of applied strain. At the strain level of 80.3% shown in Figure 4.15 c, white contrast most likely caused by the electron beam charging effect appeared inside the crack opening areas. This phenomenon suggested that the cracks went through the whole thickness of the SWCNT layer and the charging occurred because the non-conductive PET substrate was exposed to the electron beam inside the SEM.

Based on the observations mentioned above, three important statistical parameters of cracks, including average length, crack density and normal area, were defined and obtained from the real time SEM images during the loading process (Figure 4.15d). Average crack length is defined as the arithmetic mean of the crack lengths; crack density is defined as the number of cracks in the unit area; and crack normal area is defined as the area percentage of cracks in the unit area. Consistent with the earlier qualitative SEM observations, the average crack length and crack density almost stabilized at a constant level after the crack initiation stage, but the normal area of cracks kept on increasing after the crack initiation stage.

More importantly, the evolution of crack initiation and propagation has a very close relationship with the corresponding electrical properties of the SWCNT/PET electrode. At the strain level of less than 50%, the electrical resistance increased very slowly (<80%) as the increasing of applied strain. Even the cracks were found on the sample surface at this stage, the whole CNT film was still electrically connected because the crack did not go through the film thickness. Again, the average length of cracks was very stable and kept at a rather small value of around

1.5 μm. These special features in SWCNT/PET electrode seem to largely contribute to the good electrical property under large deformation. In this study, a simple model[13] based on sample geometrical changes alone seems to give a good approximation for the electrical resistance, before the cracks went through the sample thickness:

$$\frac{\Delta R}{R_0} = \left((1+\varepsilon) \cdot \frac{1}{(1-\upsilon \ln(1+\varepsilon))^2} \right) - 1 \qquad \textbf{Equation 4.}\ 8$$

where ΔR is the change in resistance, R_0 is the initial resistance, ν is Poisson's ratio and ε is the engineering strain. Poisson's ratio is taken to be 0.2 in this study, according to the typical values reported in the literature for individual CNT[141] and carbon fiber[142]. The dash line in Figure 13e illustrates the relationship between electrical resistance and applied strain in Equation 4.8. The good match between the prediction and experimental result indicates that the electrical resistance was mainly affected by the sample geometrical changes when the strain less than 50%, demonstrating a remarkable mechanical durability of the functional SWCNT/PET electrode.

For typical ITO films on PET substrates, once the cracks initiated, they would quickly go through the film width direction as well as the thickness direction, cutting off the electrical current path at relatively small strains (~3%)[54]. For SWCNT films on PET substrates, the dramatic increase of electrical resistance occurred only after the cracks went through the thickness. However, because of the

limited length of the cracks developed in such films (Figure 4.15b and c), it is very difficult to completely cut off the electrical current path. Additionally, the crack normal area as defined earlier is less than 20% before final mechanical failure of the substrate. In this case, the sample remained conductive even at very high strain level (~90%).

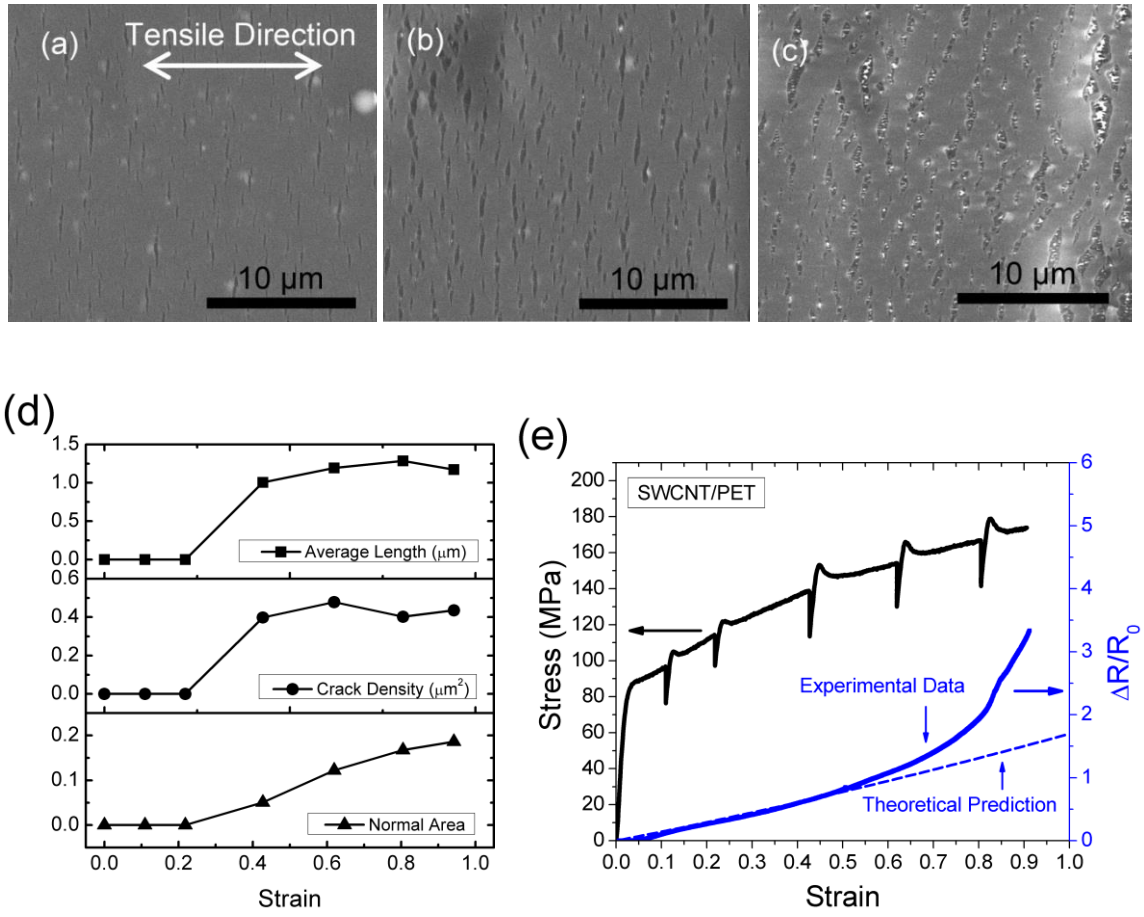

Figure 4.15 Crack initiation and propagation in SWCNT film during in situ tensile test: SEM image under the deformation of (a) strain=42.8%, (b) strain=61.5%, and (c) strain=80.3%; (d) evolution of three statistical parameter of cracks, including average length, crack density and normal area as the function of applied strain; (e) variation of stress and electrical resistance as a function of the applied strain, and R_0 denotes the electrical resistance of the initial CNT thin film .

4.3.3. *In situ* SEM observation of crack initiation and propagation in MWCNT/PET electrodes

Unlike the SWCNT/PET samples, the surface was very rough in MWCNT/PET samples even before deformation. After the applied strain reached a critical value (Figure 4.16a, strain=15.6%), short stripe-shaped cracks were found on the surface of MWCNT layer. As the increasing of the strain level (Figure 4.16b, strain=39.9%), the crack opening became wider and wider, with small bundles of MWCNTs could be observed very clearly in the crack opening areas bridging the two crack surfaces (Figure 4.16b, c and inserts). The bridging MWCNT bundles were in good contact with each other at first, which ensured that the conductivity of the MWCNT film could be maintained at this strain level. At the higher strain level shown in Figure 4.16c (strain=61.4%), some of the MWCNT bundles were pulled out from the MWCNT layer. Subsequently, the MWCNT bundles started to lose contact with each other as the applied strain raised to a higher level.

The corresponding electro-mechanical behavior in MWCNT/PET samples was very similar compared to the SWCNT/PET samples discussed earlier (Figure 4.16d). The theoretical prediction based on Equation 4.8 also seems to be applicable to MWCNT/PET samples before applied strain=45% (Figure 4.16d). At this low strain level, the MWCNT network was intact and they had relatively good contact with each other, which resulted in a fairly conductive film. This demonstrates that the remarkable mechanical durability found earlier in SWCNT/PET electrodes was also evident in MWCNT/PET electrodes. However, at the higher strain level

(strain>60%), the MWCNT bundles were pulled out and started to lose contact with each other. Therefore, once a large amount of MWCNT bundles started to be pulled out from the MWCNT film, a faster increase in electrical resistance was expected as a function of applied strain, clearly shown in Figure 4.16d.

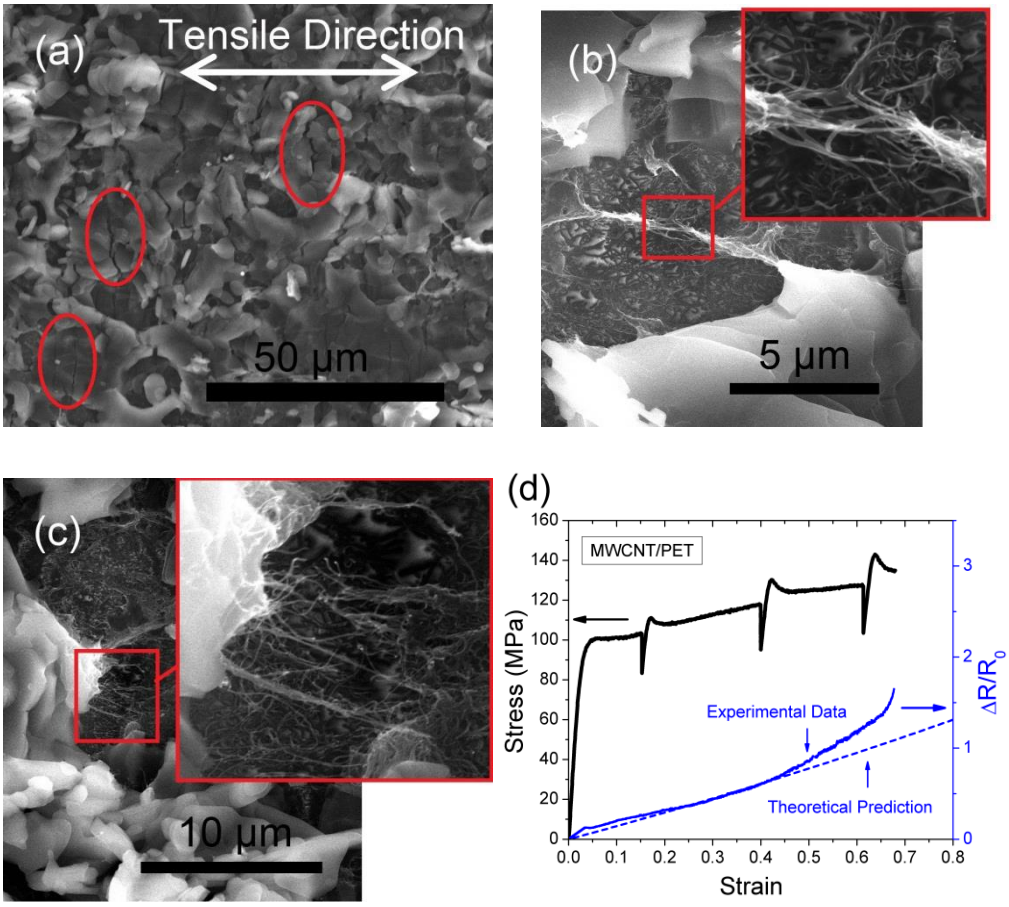

Figure 4.16 Crack initiation and propagation in MWCNT film during in situ tensile test: (a) strain=15.6%, (b) strain=39.9%, (c) strain=61.4%, and (d) variation of electrical resistance as a function of the applied strain. R_0 denotes the electrical resistance of the initial CNT thin film.

4.3.4. Electro-mechanical characterization of fatigue behavior in CNT film

In the lifetime of flexible electronics, deformation under repeated loading would be more common and is the main reason for the failure of electrodes. It is therefore very important to investigate and compare the responses of these CNT-based electrodes under the uni-axial cyclic tensile loading-unloading processes. As shown in Figure 4.17, repeated tensile loading and unloading at strain levels ranging from 0% to 2% and from 39% to 43% were applied to both SWCNT/PET and MWCNT/PET electrodes. For the fatigue behaviors for lower strain level (0%-2%), the electrical responses of the two electrodes were very similar and reached a plateau even after 250 cycles. Additionally, the higher strain level of 39%-43% had also been selected to study the electrical-mechanical response of the electrodes under cyclic loading-unloading process after the general initiation of cracks at the strain level of ~40%. Unlike the very stable electrical resistance observed in the MWCNT/PET electrode, the electrical resistance had been continuously increasing with the number of loading cycles in the SWCNT/PET electrode . After 250 cycles of loading-unloading cycles, the electrical resistance had been increased by nearly 40% for the SWCNT/PET electrode.

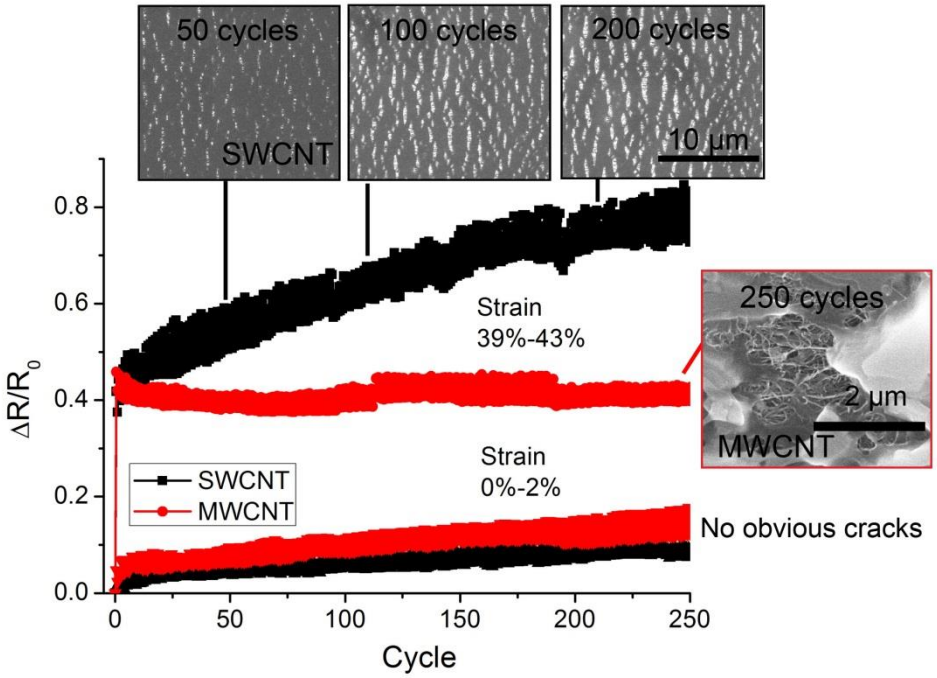

Figure 4.17 Electro-mechanical responses of CNT-based electrodes under cyclic loading-unloading testing. The applied tensile strain of bottom (upper) two curves oscillates between 0% and 2% (between 39% and 43%).

In order to understand the possible reasons of these contrasting responses in different samples, real time in situ observations accompanied to the quantitative electro-mechanical fatigue tests inside a high resolution SEM were carefully evaluated. For both SWCNT/PET and MWCNT/PET samples under the cyclic testing of low strain range, no obvious micro-cracks had been observed during and after the 250 cycles testing, and this indicates that the CNT films remain intact under such a small strain range. As a result, both the electrical resistance values of SWCNT/PET and MWCNT/PET electrodes were very stable. However, in the cyclic testing of high strain range, the difference of electrical response is due to the different microstructural evolution after crack initiation. For SWCNT/PET electrode, the

crack opening area would increase with the number of cycles. As discussed in the case of monotonic loading earlier, the electrical resistance of the SWCNT/PET sample increased with the increasing of crack opening area. This scenario seems also to be applicable in the cyclic loading case. In contrast, the intriguing network structure remained intact during the whole loading cycle for MWCNT/PET electrodes, and the MWCNT bundles had been well connected to each other after many cycles of loading-unloading, providing better electrical conductivity for MWCNT/PET electrodes.

4.4. Summary

In summary, we reported a coherent study integrating *in situ* electro-mechanical experiments and mechanics modeling to decipher the failure mechanics of ITO-based and CNT-based electrodes under tension. Our *in situ* tensile tests inside SEM reveal real time details of crack initiation and propagation, crack density evolution, and associated electrical resistance variations in these macro electrodes. The corresponding mechanics models offer better understanding of the governing failure mechanisms inside the flexible electrodes.

Firstly, we investigated the failure mechanism of single layer structure ITO thin film on polyimide substrate, and the modeling results offer quantitative determination of critical mechanical properties (ITO cohesive toughness, fracture stress, and interfacial toughness) from the experimental data and explains the experimentally observed thickness dependence of crack density. After that, we tried

to improve the electro-mechanical property in multi-layer ITO-base electrode by structure optimization. While the experimental results show that a top protective polymeric coating above and an intermediate polymeric layer below the ITO layer can effectively enhance the electro-mechanical durability of the ITO-based multilayer electrodes, the mechanics modeling suggests that this enhanced durability is due to the reduction of driving force for ITO cracking up to ten folds. The findings in this work can provide quantitative guidance for the material selection and structural optimization of organic-inorganic multilayer structures with high mechanical durability.

Compared to ITO-based electrodes, CNT-based electrodes are also considered as a good candidate for flexible electrode. *In situ* electro-mechanical testing of single-wall carbon nanotube (SWCNT) and multi-wall carbon nanotube (MWCNT) thin films deposited on PET substrates were performed inside a scanning electron microscope (SEM). The crack initiation and propagation, crack density evolution and the corresponding electrical resistance variation were systematically investigated. The results confirmed that the CNT-based electrodes had good electro-mechanical durability: in the monotonic loading tests, at least a 40% strain was required for the permanent damage of both CNT films. In the cyclic loading tests of low strain level (0%-2%), the electrical resistance kept steady, and no obvious cracking was found. However, in the cyclic loading tests of high strain level (39%-43%), the electro-mechanical response of MWCNT/PET electrode was very stable, while the electrical resistance of SWCNT/PET electrode continued to increase as the number of cycles increased. These different electrical responses were attributed to

different mechanisms associated with microstructural evolution during cyclic loading.

By this stage, there is not an "ideal" flexible electrode can meet all the requirements: high transparency, low sheet resistance, survive after large deformation, low price, good fatigue behavior. When we are selecting the suitable electrode for certain purpose, the following Table 4.3 and the Table 1.2 in Chapter 1 can be both used as a reference.

Table 4. 3 Comparison of ITO-base and CNT-based electrodes (All the data came from the samples testing in this work, and R is electrical resistance)

Sample	Transparancy	Sheet Resistance (Ω/□)	Thickness (nm)	Critical Strain	Price	Fatigue Behavior
ITO-based	80%	400	80	1%-3%	High	Dramatical increase in R
MWCNT-based	40%	1900	75	50%	Low	Very steady in R
SWCNT-based	70%	1200	75	50%	Low	Graduately increase in R

Chapter 5

5. Concluding Remarks

5.1. Summary

During the development of flexile electronics, it is critical and crucial to improve the quality of flexible electrodes. In this work, we have performed nanomechanical and electro-mechanical characterization of materials for flexible electrode applications, including metallic NWs, ITO-based and CNT-based electrodes.

Four different testing platforms were designed and developed for electro-mechanical characterization and electro-mechanical characterization purpose. For the nano/sub-micro size samples, the micro mechanical devices can be used for uni-axial and bi-axial loading tests. For the macro size samples, the micro tester can be

used for *in situ* monotonic tensile test, while the fatigue tester can be used for *in situ* cyclic tensile or bending testing purpose.

In the nano scale, we have investigated mechanical behaviors of metallic nanowires under uni-axial tensile loading inside a SEM chamber. Engineering stress-strain curves were obtained, and *in situ* observations of deformation and fracture process were realized in real time. More importantly, we have demonstrated both size and strain-rate dependence on yield stress of single-crystalline Ni NWs with varying diameters (from 100 to 300 nm). The experimental results show a very high strain rate sensitivity in the order of ~0.1 and a very small activation volumes in the order of $\sim 10b^3$ for these Ni NWs, and such findings are confirmed by atomistic simulations. Moreover, two different size dependent fracture modes, namely ductile and brittle-like fractures, were found in the same batch of Cu nanowire samples.

In macro scale, we studied the electro-mechanical behaviors of ITO-base and CNT-based flexible electrodes. Firstly, we investigated the failure mechanism of single layer structure ITO thin film on polyimide substrate, and the modeling results offer quantitative determination of critical mechanical properties (ITO cohesive toughness, fracture stress, and interfacial toughness) from the experimental data and explains the experimentally observed thickness dependence of crack density. After that, we successfully improved the electro-mechanical property in multi-layer ITO-base electrode by structure optimization method. Finally, *in situ* electro-mechanical testing of SWCNT and MWCNT thin films deposited on PET substrates

were performed inside a SEM. The crack initiation and propagation, crack density evolution and the corresponding electrical resistance variation were systematically investigated. The results confirmed that the CNT-based electrodes had good electromechanical durability.

This work is a combined experimental and simulation study in both macro and nano scale. The results quantified the materials properties of metallic nanowires, and also provided with methods to better understand and improve the electro-mechanical properties in flexible electrodes. So the findings are believed to provide some further insights into the important yet complicated deformation mechanisms for nanoscale metals and fracture mechanism for flexible electrodes.

5.2. Suggestions for future work

There is never an ending for research work. Further work of this thesis may include but not limit in the following:

1. Electro-mechanical and thermo-mechanical characterization for one-dimensional nanomaterials. In the past decade, people have already well developed abundant methods to test pure mechanical properties of 1-D nanomaterials. However, it is still difficult to test their response under coupling electro-mechanical or thermo-mechanical fields. It would be very interesting to see the electrical response under the

deformation and mechanical response in different temperatures, because these scenarios are more close to the real applications.

2. Electro-mechanical or pure mechanical characterization for 2-D nanomaterials. The 2-D can be relatively easy to be fabricated in the lab, but the mechanical measurement is still under explored. Even we have designed a simple micro mechanical device for this purpose in Chapter 2, it is still on the beginning stage and needs more improvements. The two of big challenges might be Sample clamping and data analysis.
3. Mechanical properties of NWs 20-100 nm in diameter. Right now, it is possible to test NWs <10nm in TEM and >100 nm in diameter in SEM. The data between 20-100 nm is still missing. According form the prediction, the transition is happened in 100 nm. If we can have the missing data, more information can be obtained for the improvement.
4. Structure optimization of ITO-based electrodes. Generally speaking, there are two ways to improve the product qualities: material improvement and structure optimization. For ITO-based electrodes, too much effort has been made in the past 20 years, so structure optimization can be another opportunity for us. In the theoretical work, Li proposed the out-of-plane idea which can minimize the local strain and improve the durability.[143] It might be worth trying to improve the ITO-based electrodes.

5. New material system occurrence because of the fabrication techniques improvement. As mentioned before, thin means flexible. For flexible electronics, how to reduce the thickness of electrode and still keep its conductance and durability is the final goal. How to reduce the contact resistance in CNT-based electrodes can be one research direction. And new material system like metallic grid cover with graphene is a good example[47]: metallic grid serves as the backbone of current path, and graphene serves as the bridge once the backbone is damaged somewhere. The electro-mechanical testing data might be interesting to see for this kind of new material systems.

Publications and Patent List

Publication List

1. C. Peng, Y. Zhong, Y. Lu, S. Narayanan, T. Zhu, and J. Lou, Strain rate dependent mechanical properties in single crystal nickel nanowires, Appl. Phys. Lett. 102, 083102 (2013).

2. C. Peng, Z. Jia, H. Neilson, T. Li, and J. Lou, In Situ Electro-mechanical Experiments and Mechanics Modeling of Fracture in Indium Tin Oxide-based Multilayer Electrodes, Advanced Engineering Materials, DOI: 10.1002/adem.201200169 (2012).

3. C. Peng, Y. Zhan, and J. Lou, Size dependent fracture modes transition in copper nanowires, Small, DOI: 10.1002/smll.201101911 (2012).

4. C. Peng, Y. Ganesan, Y. Lu, and J. Lou, Size dependent mechanical properties of single crystalline nickel nanowires, J. Appl. Phys., 111 (2012).

5. C. Peng, Z. Jia, D. Bianculli, T. Li, and J. Lou, In situ electro-mechanical experiments and mechanics modeling of tensile cracking in indium tin oxide thin films on polyimide substrates, J. Appl. Phys., 109 (2011).

6. Z. Jia, C. Peng, J. Lou, and T. Li, A map of competing buckling-driven failure modes of substrate-supported thin brittle films, Accepted by Thin Solid Films, (2012)

7. Y. Lu, C. Peng, Y. Ganesan, J. Huang and J. Lou, Quantitative in situ TEM tensile testing of an individual nickel nanowires, Nanotechnology, 22 (2011).

8. Y. Ganesan, C. Peng, Y. Lu, P. Loya, P. Moloney, E. Barrera, J. Tour, B. Yakobson, R. Ballarini and J. Lou, Interface toughness of MWNT reinforced epoxy nanocomposites, ACS Applied Materials and Interfaces, 3 (2011).

9. Y. Ganesan, C. Peng, Y. Lu, L. Ci, A. Srivastava, P.M. Ajayan and J. Lou, Effects of nitrogen doping on the mechanical properties of carbon nanotubes, ACS Nano, 4 (2010).

10. J. Zhang, P. Loya, C. Peng, V. Khabashesku, J. Lou, Quantitative in situ mechanical characterization of the effects of chemical functionalization on individual carbon nanofibers, Advanced Functional Materials, DOI: 10.1002/adfm.201200593 (2012).

11. Y. Zhan, Y. Lu, C. Peng and J. Lou, Solvothermal synthesis and mechanical characterization of single crystalline copper nanorings, J Crystal Growth, 325 (2011).

12. Y. Ganesan, Y. Lu, C. Peng, H. Lu, R. Ballarini and J. Lou, Development and application of a novel micro-fabricated device for in situ tensile testing of 1-D nanomaterials, J. Microelectromechanical Systems, 19 (2010).

13. Z. Liu, L. Hu, J. Liu, C. Qiu, H. Zhou, D. Hashim, G. Shi, C. Peng, S. Najmaei, L. Sun, J. Lou, and P. Ajayan, Correlation between droplet-induced strain actuation and voltage generation in single-wall carbon nanotube films, Nano Lett., 11 (2011).

Patent List

1. Micromechanical devices for materials characterization, J. Lou, Y. Ganesan, Y. Lu and C. Peng, US patent 8058613, 2011.

References

1. Crabb, R.L. and F.C. Treble, *Thin Silicon Solar Cells for Large Flexible Arrays.* Nature, 1967. **213**(5082): p. 1223-1224.
2. Ray, K.A., *Flexible Solar Cell Arrays for Increased Space Power.* Aerospace and Electronic Systems, IEEE Transactions on, 1967. **AES-3**(1): p. 107-115.
3. Lin, Y.Y., et al., *Stacked pentacene layer organic thin-film transistors with improved characteristics.* Electron Device Letters, IEEE, 1997. **18**(12): p. 606-608.
4. Schön, J.H., C. Kloc, and B. Batlogg, *On the intrinsic limits of pentacene field-effect transistors.* Organic Electronics, 2000. **1**(1): p. 57-64.
5. Bae, S., et al., *Roll-to-roll production of 30-inch graphene films for transparent electrodes.* Nature Nanotechnology, 2010. **5**(8): p. 574-578.
6. Hattori, R., et al., *10.3: Distinguished Paper: Ultra Thin and Flexible Paper-Like Display using QR-LPD® Technology.* SID Symposium Digest of Technical Papers, 2004. **35**(1): p. 136-139.
7. Rogers, J.A., T. Someya, and Y.G. Huang, *Materials and Mechanics for Stretchable Electronics.* Science, 2010. **327**(5973): p. 1603-1607.
8. Pagliaro, M., R. Ciriminna, and G. Palmisano, *Flexible Solar Cells.* Chemsuschem, 2008. **1**(11): p. 880-891.
9. Leterrier, Y., et al., *Mechanical integrity of transparent conductive oxide films for flexible polymer-based displays.* Thin Solid Films, 2004. **460**(1-2): p. 156-166.
10. Lipomi, D.J., et al., *Skin-like pressure and strain sensors based on transparent elastic films of carbon nanotubes.* Nature Nanotechnology, 2011. **6**(12): p. 788-792.
11. http://www.fujifilmholdings.com.
12. Sierros, K.A., et al., *Stress-corrosion cracking of indium tin oxide coated polyethylene terephthalate for flexible optoelectronic devices.* Thin Solid Films, 2009. **517**(8): p. 2590-2595.
13. Sierros, K.A., et al., *Durable transparent carbon nanotube films for flexible device components.* Thin Solid Films, 2010. **518**(23): p. 6977-6983.
14. Kaempgen, M., G.S. Duesberg, and S. Roth, *Transparent carbon nanotube coatings.* Applied Surface Science, 2005. **252**(2): p. 425-429.
15. Hu, L.B., et al., *Highly stretchable, conductive, and transparent nanotube thin films.* Applied Physics Letters, 2009. **94**(16).
16. Pei, S.F., et al., *The fabrication of a carbon nanotube transparent conductive film by electrophoretic deposition and hot-pressing transfer.* Nanotechnology, 2009. **20**(23).
17. Chen, C.L., et al., *Mechanical and electrical evaluation of parylene-C encapsulated carbon nanotube networks on a flexible substrate.* Applied Physics Letters, 2008. **93**(9).

18. Wu, Z.C., et al., *Transparent, conductive carbon nanotube films.* Science, 2004. **305**(5688): p. 1273-1276.
19. Hu, L.B., et al., *Scalable Coating and Properties of Transparent, Flexible, Silver Nanowire Electrodes.* Acs Nano, 2010. **4**(5): p. 2955-2963.
20. Daw, M.S. and M.I. Baskes, *Embedded-atom method: Derivation and application to impurities, surfaces, and other defects in metals.* Physical Review B, 1984. **29**(12): p. 6443-6453.
21. Kohn, W., A.D. Becke, and R.G. Parr, *Density Functional Theory of Electronic Structure.* The Journal of Physical Chemistry, 1996. **100**(31): p. 12974-12980.
22. Atkinson, M., *Further Analysis of the Size Effect in Indentation Hardness Tests of Some Metals.* Journal of Materials Research, 1995. **10**(11): p. 2908-2915.
23. Zhu, Y. and H.D. Espinosa, *An electromechanical material testing system for in situ electron microscopy and applications.* Proceedings of the National Academy of Sciences of the United States of America, 2005. **102**(41): p. 14503-14508.
24. Wu, B., A. Heidelberg, and J.J. Boland, *Mechanical properties of ultrahigh-strength gold nanowires.* Nature Materials, 2005. **4**(7): p. 525-529.
25. Uchic, M.D., et al., *Exploring specimen size effects in plastic deformation of Ni3(Al, Ta).* Mat. Res. Soc. Symp. Proc., 2003. **753**: p. BB1.4.1.
26. Greer, J.R. and W.D. Nix, *Size dependence of mechanical properties of gold at the sub-micron scale.* Applied Physics A, 2005. **80**(8): p. 1625-1629.
27. Jennings, A.T. and J.R. Greer, *Tensile deformation of electroplated copper nanopillars.* Philosophical Magazine, 2011. **91**(7-9): p. 1108-1120.
28. Lu, Y., et al., *Cold welding of ultrathin gold nanowires.* Nature Nanotechnology, 2010. **5**(3): p. 218-224.
29. Uchic, M.D., et al., *Sample dimensions influence strength and crystal plasticity.* Science, 2004. **305**(5686): p. 986-989.
30. Lu, Y., et al., *Fracture of Sub-20nm Ultrathin Gold Nanowires.* Advanced Functional Materials, 2011. **doi: 10.1002/adfm.201101224**.
31. Volkert, C.A. and E.T. Lilleodden, *Size effects in the deformation of sub-micron Au columns.* Philosophical Magazine, 2006. **86**(33-35): p. 5567-5579.
32. Richter, G., et al., *Ultrahigh Strength Single Crystalline Nanowhiskers Grown by Physical Vapor Deposition.* Nano Letters, 2009. **9**(8): p. 3048-3052.
33. Zhang, D.F., et al., *In situ tensile testing of individual Co nanowires inside a scanning electron microscope.* Nanotechnology, 2009. **20**: p. 365706.
34. Wu, B., et al., *Microstructure-hardened silver nanowires.* Nano Letters, 2006. **6**(3): p. 468-472.
35. Minor, A.M., et al., *A new view of the onset of plasticity during the nanoindentation of aluminium.* Nature Materials, 2006. **5**(9): p. 697-702.
36. Mason, J.K., A.C. Lund, and C.A. Schuh, *Determining the activation energy and volume for the onset of plasticity during nanoindentation.* Physical Review B, 2006. **73**(5): p. 054102.

37. Tvingstedt, K. and O. Inganäs, *Electrode Grids for ITO Free Organic Photovoltaic Devices.* Advanced Materials, 2007. **19**(19): p. 2893-2897.
38. Kang, M.-G., et al., *Organic Solar Cells Using Nanoimprinted Transparent Metal Electrodes.* Advanced Materials, 2008. **20**(23): p. 4408-4413.
39. Rathmell, A.R. and B.J. Wiley, *The Synthesis and Coating of Long, Thin Copper Nanowires to Make Flexible, Transparent Conducting Films on Plastic Substrates.* Advanced Materials, 2011. **23**(41): p. 4798-+.
40. Wu, H., et al., *Electrospun Metal Nanofiber Webs as High-Performance Transparent Electrode.* Nano Letters, 2010. **10**(10): p. 4242-4248.
41. Bentley, A.K., et al., *Template synthesis and magnetic manipulation of nickel nanowires.* Journal of Chemical Education, 2005. **82**(5): p. 765-768.
42. Zhan, Y.J., et al., *Solvothermal synthesis and mechanical characterization of single crystalline copper nanorings.* Journal of Crystal Growth, 2011. **325**(1): p. 76-80.
43. Kim, F., J.H. Song, and P.D. Yang, *Photochemical synthesis of gold nanorods.* Journal of the American Chemical Society, 2002. **124**(48): p. 14316-14317.
44. Murphy, C.J. and N.R. Jana, *Controlling the aspect ratio of inorganic nanorods and nanowires.* Advanced Materials, 2002. **14**(1): p. 80-82.
45. Wang, X., L.J. Zhi, and K. Mullen, *Transparent, conductive graphene electrodes for dye-sensitized solar cells.* Nano Letters, 2008. **8**(1): p. 323-327.
46. Tung, V.C., et al., *High-throughput solution processing of large-scale graphene.* Nat Nano, 2009. **4**(1): p. 25-29.
47. Zhu, Y., et al., *Rational Design of Hybrid Graphene Films for High-Performance Transparent Electrodes (vol 5, pg 6472, 2011).* Acs Nano, 2011. **5**(9): p. 7686-7686.
48. Ganesan, Y., et al., *Development and Application of a Novel Microfabricated Device for the In Situ Tensile Testing of 1-D Nanomaterials.* Journal of Microelectromechanical Systems, 2010. **19**(3): p. 675-682.
49. Eberl, C., D.S. Gianola, and K.J. Hemker, *Mechanical Characterization of Coatings Using Microbeam Bending and Digital Image Correlation Techniques.* Experimental Mechanics, 2010. **50**(1): p. 85-97.
50. Scuor, N., et al., *Design of a novel MEMS platform for the biaxial stimulation of living cells.* Biomedical Microdevices, 2006. **8**(3): p. 239-246.
51. Loh, O., A. Vaziri, and H.D.S.M. Espinosa, *The Potential of MEMS for Advancing Experiments and Modeling in Cell Mechanics.* Experimental Mechanics, 2009. **49**(1): p. 105-124.
52. Lee, C., et al., *Measurement of the elastic properties and intrinsic strength of monolayer graphene.* Science, 2008. **321**(5887): p. 385-388.
53. Song, L., et al., *Large Scale Growth and Characterization of Atomic Hexagonal Boron Nitride Layers.* Nano Letters, 2010. **10**(8): p. 3209-3215.
54. Peng, C., et al., *In situ electro-mechanical experiments and mechanics modeling of tensile cracking in indium tin oxide thin films on polyimide substrates.* Journal of Applied Physics, 2011. **109**(10): p. 103530.

55. Pascual, J.I., et al., *Properties of Metallic Nanowires - from Conductance Quantization to Localization.* Science, 1995. **267**(5205): p. 1793-1795.
56. Cui, Y., et al., *Nanowire nanosensors for highly sensitive and selective detection of biological and chemical species.* Science, 2001. **293**(5533): p. 1289-1292.
57. Wu, Y., et al., *Single-crystal metallic nanowires and metal/semiconductor nanowire heterostructures.* Nature, 2004. **430**(6995): p. 61-65.
58. Cao, H.Q., et al., *Synthesis and I-V properties of aligned copper nanowires.* Nanotechnology, 2006. **17**(6): p. 1736-1739.
59. Zhu, T., et al., *Temperature and strain-rate dependence of surface dislocation nucleation.* Physical Review Letters, 2008. **100**(025502).
60. Zhu, T., et al., *Mechanics of Ultra-Strength Materials.* Mrs Bulletin, 2009. **34**(3): p. 167-172.
61. Gall, K., J.K. Diao, and M.L. Dunn, *The strength of gold nanowires.* Nano Letters, 2004. **4**(12): p. 2431-2436.
62. Ma, F. and K.W. Xu, *Size-dependent theoretical tensile strength and other mechanical properties of [001] oriented Au, Ag, and Cu nanowires.* Journal of Materials Research, 2006. **21**(11): p. 2810-2816.
63. Wu, H.A., *Molecular dynamics study of the mechanics of metal nanowires at finite temperature.* European Journal of Mechanics a-Solids, 2006. **25**(2): p. 370-377.
64. Leach, A.M., M. McDowell, and K. Gall, *Deformation of top-down and bottom-up silver nanowires.* Advanced Functional Materials, 2007. **17**(1): p. 43-53.
65. Park, H.S. and P.A. Klein, *Surface Cauchy-Born analysis of surface stress effects on metallic nanowires.* Physical Review B, 2007. **75**: p. 085408.
66. Chen, C.Q., et al., *Size dependence of Young's modulus in ZnO nanowires.* Physical Review Letters, 2006. **96**: p. 075505.
67. Agrawal, R., B. Peng, and H.D. Espinosa, *Experimental-Computational Investigation of ZnO nanowires Strength and Fracture.* Nano Letters, 2009. **9**(12): p. 4177-4183.
68. Zhu, Y., et al., *Mechanical Properties of Vapor-Liquid-Solid Synthesized Silicon Nanowires.* Nano Letters, 2009. **9**(11): p. 3934-3939.
69. Brenner, S.S., *Tensile Strength of Whiskers.* Journal of Applied Physics, 1956. **27**(12): p. 1484-1491.
70. Brenner, S.S., *Plastic Deformation of Copper and Silver Whiskers.* Journal of Applied Physics, 1957. **28**(9): p. 1023-1026.
71. Brenner, S.S., *Growth and Properties of Whiskers.* Science, 1958. **128**(3324): p. 569-575.
72. Fleck, N.A., et al., *Strain Gradient Plasticity: Theory and Experiment.* Acta Metallurgica Et Materialia, 1994. **42**(2): p. 475-487.
73. Stolken, J.S. and A.G. Evans, *A microbend test method for measuring the plasticity length scale.* Acta Materialia, 1998. **46**(14): p. 5109-5115.
74. Lou, J., P. Shrotriya, and W.O. Soboyejo, *A cyclic microbend study on LIGA Ni microelectromechanical systems thin films.* Journal of Engineering Materials and Technology, 2005. **127**(1): p. 16-22.

75. Guzman, M.S.D., et al., *Role of indentation depth on the measured hardness of materials, in Thin Films: Stresses and Mechanical Properties IV.* Mater. Res. Soc. Symp. Proc., 1993. **308**: p. 613-618.
76. Stelmashenko, N.A., et al., *Microindentations on W and Mo Oriented Single-Crystals - an STM Study.* Acta Metallurgica Et Materialia, 1993. **41**(10): p. 2855-2865.
77. Ma, Q. and D.R. Clarke, *Size-Dependent Hardness of Silver Single-Crystals.* Journal of Materials Research, 1995. **10**(4): p. 853-863.
78. Poole, W.J., M.F. Ashby, and N.A. Fleck, *Micro-hardness of annealed and work-hardened copper polycrystals.* Scripta Materialia, 1996. **34**(4): p. 559-564.
79. McElhaney, K.W., J.J. Vlassak, and W.D. Nix, *Determination of indenter tip geometry and indentation contact area for depth-sensing indentation experiments.* Journal of Materials Research, 1998. **13**(5): p. 1300-1306.
80. Lou, J., et al., *Nanoindentation study of plasticity length scale effects in LIGA Ni microelectromechanical systems structures.* Journal of Materials Research, 2003. **18**(3): p. 719-728.
81. Dimiduk, D.M., M.D. Uchic, and T.A. Parthasarathy, *Size-affected single-slip behavior of pure nickel microcrystals.* Acta Materialia, 2005. **53**(15): p. 4065-4077.
82. Frick, C.P., et al., *Size effect on strength and strain hardening of small-scale [111] nickel compression pillars.* Materials Science and Engineering A, 2008. **489**(1-2): p. 319-329.
83. Lu, Y. and J. Lou, *Quantitative In-situ Nanomechanical Characterization of Metallic Nanowires.* JOM, 2011. **63**(9): p. 35-42.
84. Abraham, F.F. and H.J. Gao, *Anomalous ductile-brittle fracture behaviour in fcc crystals.* Philosophical Magazine Letters, 1998. **78**(4): p. 307-312.
85. Kang, K. and W. Cai, *Brittle and ductile fracture of semiconductor nanowires - molecular dynamics simulations.* Philosophical Magazine, 2007. **87**(14-15): p. 2169-2189.
86. Kang, K.W. and W. Cai, *Size and temperature effects on the fracture mechanisms of silicon nanowires: Molecular dynamics simulations.* International Journal of Plasticity, 2010. **26**(9): p. 1387-1401.
87. Lee, G., et al., *Fabrication, structure and mechanical properties of indium nanopillars.* Acta Materialia, 2010. **58**(4): p. 1361-1368.
88. McDowell, M.T., A.M. Leach, and K. Gall, *On The Elastic Modulus of Metallic Nanowires.* Nano Letters, 2008. **8**(11): p. 3613-3618.
89. Peng, C., et al., *Size dependent mechanical properties of single crystalline nickel nanowires.* J. Appl. Phys. , 2012(111): p. 063524.
90. Jennings, A.T., J. Li, and J.R. Greer, *Emergence of strain-rate sensitivity in Cu nanopillars: Transition from dislocation multiplication to dislocation nucleation.* Acta Materialia, 2011. **59**(14): p. 5627-5637.
91. Zhu, T. and J. Li, *Ultra-strength materials.* Progress in Materials Science, 2010. **55**(7): p. 710-757.

92. Lu, L., et al., *Size dependence of rate-controlling deformation mechanisms in nanotwinned copper.* Scripta Materialia, 2009. **60**(12): p. 1062-1066.
93. Wang, Y.M., A.V. Hamza, and E. Ma, *Temperature-dependent strain rate sensitivity and activation volume of nanocrystalline Ni.* Acta Materialia, 2006. **54**(10): p. 2715-2726.
94. Whitney, T.M., et al., *Fabrication and Magnetic-Properties of Arrays of Metallic Nanowires.* Science, 1993. **261**(5126): p. 1316-1319.
95. Yin, A.J., et al., *Fabrication of highly ordered metallic nanowire arrays by electrodeposition.* Applied Physics Letters, 2001. **79**(7): p. 1039-1041.
96. Zhang, L., et al., *Controlled Swimming of Ni Nanowires Using Rotating Magnetic Field.* IEEE-NANO Conf. Proc., 2009. **9**: p. 487-490.
97. Ganesan, Y., et al., *Effect of Nitrogen Doping on the Mechanical Properties of Carbon Nanotubes.* Acs Nano, 2010. **4**(12): p. 7637-7643.
98. Howatson, A.M., P.G. Lund, and J.D. Todd, Engineering Tables and Data Amsterdam, The Netherlands: Kluwer, 1991: p. 41.
99. Lu, Y., et al., *Quantitative in situ TEM tensile testing of an individual nickel nanowire.* Nanotechnology, 2011. **22**(35): p. 355702.
100. Kiener, D., et al., *A further step towards an understanding of size-dependent crystal plasticity: In situ tension experiments of miniaturized single-crystal copper samples.* Acta Materialia, 2008. **56**(3): p. 580-592.
101. Oh, S.H., et al., *In situ observation of dislocation nucleation and escape in a submicrometre aluminium single crystal.* Nature Materials, 2009. **8**(2): p. 95-100.
102. Schneider, A.S., et al., *Effect of orientation and loading rate on compression behavior of small-scale Mo pillars (vol 508, pg 241, 2009).* Materials Science and Engineering a-Structural Materials Properties Microstructure and Processing, 2010. **527**(4-5): p. 1280-1280.
103. Mishin, Y., M.J. Mehl, and D.A. Papaconstantopoulos, *Embedded-atom potential for B2-NiAl* Physical Review B, 2003. **65**: p. 224114.
104. Warner, D.H. and W.A. Curtin, *Origins and implications of temperature-dependent activation energy barriers for dislocation nucleation in face-centered cubic metals.* Acta Materialia, 2009. **57**(14): p. 4267-4277.
105. Ryu, S., K. Kang, and W. Cai, *Entropic effect on the rate of dislocation nucleation.* Proceedings of the National Academy of Sciences of the United States of America, 2011. **108**(13): p. 5174-5178.
106. Beuth, J.L., *Cracking of Thin Bonded Films in Residual Tension.* International Journal of Solids and Structures, 1992. **29**(13): p. 1657-1675.
107. Hutchinson, J.W. and Z. Suo, *Mixed-Mode Cracking in Layered Materials.* Advances in Applied Mechanics, 1992. **29**: p. 63-191.
108. Ma, Q., *A four-point bending technique for studying subcritical crack growth in thin films and at interfaces.* Journal of Materials Research, 1997. **12**(3): p. 840-845.

109. Tsui, T.Y., A.J. McKerrow, and J.J. Vlassak, *Constraint effects on thin film channel cracking behavior.* Journal of Materials Research, 2005. **20**(9): p. 2266-2273.
110. Liu, X.H., et al., *Delamination in patterned films.* International Journal of Solids and Structures, 2007. **44**(6): p. 1706-1718.
111. Chiu, S.L., J. Leu, and P.S. Ho, *Fracture of Metal-Polymer Line Structures .1. Semiflexible Polyimide.* Journal of Applied Physics, 1994. **76**(9): p. 5136-5142.
112. Alaca, B.E., M.T.A. Saif, and H. Sehitoglu, *On the interface debond at the edge of a thin film on a thick substrate.* Acta Materialia, 2002. **50**(5): p. 1197-1209.
113. Li, T., et al., *Stretchability of thin metal films on elastomer substrates.* Applied Physics Letters, 2004. **85**(16): p. 3435-3437.
114. Li, T., et al., *Delocalizing strain in a thin metal film on a polymer substrate.* Mechanics of Materials, 2005. **37**(2-3): p. 261-273.
115. Lu, N.S., et al., *Metal films on polymer substrates stretched beyond 50%.* Applied Physics Letters, 2007. **91**(22).
116. Zhang, Z. and T. Li, *Effects of grain boundary adhesion and grain size on ductility of thin metal films on polymer substrates.* Scripta Materialia, 2008. **59**(8): p. 862-865.
117. Begley, M.R., et al., *Fracture of nanoscale copper films on elastomer substrates.* Applied Physics Letters, 2009. **95**(23).
118. Lu, N.S., et al., *Failure by simultaneous grain growth, strain localization, and interface debonding in metal films on polymer substrates.* Journal of Materials Research, 2009. **24**(2): p. 379-385.
119. Rochat, G., et al., *Mechanical analysis of ultrathin oxide coatings on polymer substrates in situ in a scanning electron microscope.* Thin Solid Films, 2003. **437**(1-2): p. 204-210.
120. Jansson, N.E., et al., *Calculation of adhesive and cohesive fracture toughness of a thin brittle coating on a polymer substrate.* Thin Solid Films, 2006. **515**(4): p. 2097-2105.
121. Cairns, D.R., et al., *Strain-dependent electrical resistance of tin-doped indium oxide on polymer substrates.* Applied Physics Letters, 2000. **76**(11): p. 1425-1427.
122. Cairns, D.R. and G.P. Crawford, *Electromechanical properties of transparent conducting substrates for flexible electronic displays.* Proceedings of the IEEE, 2005. **93**(8): p. 1451-1458.
123. Ambrico, J.M. and M.R. Begley, *The role of initial flaw size, elastic compliance and plasticity in channel cracking of thin films.* Thin Solid Films, 2002. **419**(1-2): p. 144-153.
124. Vlassak, J.J., *Channel cracking in thin films on substrates of finite thickness.* International Journal of Fracture, 2003. **119**(4-2): p. 299-323.
125. Mei, H.X., Y.Y. Pang, and R. Huang, *Influence of interfacial delamination on channel cracking of elastic thin films.* International Journal of Fracture, 2007. **148**(4): p. 331-342.

126. Jia, Z., M.B. Tucker, and T. Li, *Failure mechanics of organic-inorganic multilayer permeation barriers in flexible electronics.* Composites Science and Technology, 2011. **71**(3): p. 365-372.
127. Jansson, N.E., Y. Leterrier, and J.A.E. Manson, *Modeling of multiple cracking and decohesion of a thin film on a polymer substrate.* Engineering Fracture Mechanics, 2006. **73**(17): p. 2614-2626.
128. Leterrier, Y., *Durability of nanosized oxygen-barrier coatings on polymers.* Progress in Materials Science, 2003. **48**(1): p. 1-55.
129. Kim, K.S., et al., *Large-scale pattern growth of graphene films for stretchable transparent electrodes.* Nature, 2009. **457**(7230): p. 706-710.
130. Forrest, S.R., *The path to ubiquitous and low-cost organic electronic appliances on plastic.* Nature, 2004. **428**(6986): p. 911-918.
131. Crawford, G.P., *Flexible Flat Panel Displays*. 2005, Chichester, UK: John Wiley & Sons.
132. Lacour, S.P., et al., *Stretchable interconnects for elastic electronic surfaces.* Proceedings of the Ieee, 2005. **93**(8): p. 1459-1467.
133. Wong, W.S. and A. Salleo, *Flexible Electronics*. 2009, New York, NY: Springer.
134. Lipomi, D.J. and Z.A. Bao, *Stretchable, elastic materials and devices for solar energy conversion.* Energy & Environmental Science, 2011. **4**(9): p. 3314-3328.
135. Lewis, J.S. and M.S. Weaver, *Thin-film permeation-barrier technology for flexible organic light-emitting devices.* Ieee Journal of Selected Topics in Quantum Electronics, 2004. **10**(1): p. 45-57.
136. Erlat, A.G., M. Yan, and A.R. Duggal, *Substrates and Thin-Film Barrier Technology for Flexible Electronics*, in *Flexible Electronics*. 2009. p. 413-449.
137. Nisato, G., et al., *Thin Film Encapsulation for OLEDs: Evaluation of Multi-layer Barriers using the Ca Test.* SID Symposium Digest of Technical Papers, 2003. **34**(1): p. 550-553.
138. Moro, L., et al. *Integrated encapsulation of bottom and top emission OLED displays*. in *PIE-The International Society for Optical Engineering, Organic Light-Emitting Materials and Devices VIII, Denver, CO, USA*. 2004.
139. Cordero, N., J. Yoon, and Z.G. Suo, *Channel cracks in a hermetic coating consisting of organic and inorganic layers.* Applied Physics Letters, 2007. **90**(11): p. 111910.
140. Jia, Z., et al., *A map of competing buckling-driven failure modes of substrate-supported thin brittle films.* Thin Solid Films, 2012. **520**(21): p. 6576-6580.
141. Yakobson, B.I., C.J. Brabec, and J. Bernholc, *Nanomechanics of carbon tubes: Instabilities beyond linear response.* Physical Review Letters, 1996. **76**(14): p. 2511-2514.
142. Lee, H.G., H.Y. Hwang, and D.G. Lee, *Effect of wear debris on the tribological characteristics of carbon fiber epoxy composites.* Wear, 2006. **261**(3-4): p. 453-459.

143. Tucker, M.B. and T. Li, *Strain Deconcentration in Thin Films Patterned with Circular Holes.* International Journal of Applied Mechanics, 2009. **1**(4): p. 557-568.